ELECTRON MICROSCOPY IMAGING OF FLUX PINNING DEFECTS IN YBCO SUPERCONDUCTORS

BY

Anne-Hélène PUICHAUD

A thesis
submitted to the Victoria University of Wellington
in fulfilment of the requirements for the degree of
Doctor of Philosophy

Victoria University of Wellington
2016

Abstract

High-temperature superconductors are of great interest because they can transport electrical current without loss. For real-world applications, the amount of current, known as the critical current I_c, that can be carried by superconducting wires is the key figure of merit. Large I_c values are necessary to off-set the higher cost of these wires. The factors that improve I_c (microstructure/performance relationship) in the state-of-the-art coated conductor wires based on $YBa_2Cu_3O_7$ (YBCO) are not fully understood. However, microstructural defects that immobilise (or pin) tubes of magnetic flux (known as vortices) inside the coated conductors are known to play a role in improving I_c.

In this thesis, the vortex-defect interaction in YBCO superconductors was investigated with high-end transmission electron microscopy (TEM) techniques using two approaches.

First, the effect of dysprosium (Dy) addition and oxygenation temperature on the microstructure and critical current were investigated in detail. Changing only the oxygenation temperature leads to many microstructural changes in pure YBCO coated conductors. It was found that Dy addition reduces the sensitivity of the YBCO to the oxygenation temperature, in particular it lowers the microstructural disorder while maintaining the formation of nanoparticles, which both contribute to the enhancement of I_c.

In the second approach, two TEM based techniques (off-axis electron holography and Lorentz microscopy) were used to study the magnetic flux vortices. Vortex imaging was attempted with a TEM operated at 300 kV on both a YBCO crystal as well as a YBCO coated conductor. Many challenges were encountered including sample preparation, inhomogeneity, and geometry, in addition to the need to perform measurements at cryogenic temperatures. Although vortices were not able to be observed in the coated conductors, tentative observation of vortices in a YBCO crystal was made using Lorentz microscopy. Improvements for future electron holography experiments on YBCO at low voltage are suggested. This work represents a pioneering step towards directly imaging vortices in YBCO using more widely available microscopes with the aim of better understanding flux pinning to ultimately boost I_c in superconducting wires.

À mes parents

Acknowledgements

It is a pleasure for me to acknowledge many people that have contributed throughout the last three years and without whom all this work would not have been the same. First I would like to express my deep gratitude to my supervisors: Dr Ruth Knibbe, for her advice, support and for believing in me from the beginning. I am grateful for her time; despite her busy schedule, she found moments for personal and professional guidance. I want to thank my co-supervisor, Dr Stuart Wimbush, for his input in this project, the useful discussions and suggestions.

From the Robinson Research Institute, I am thankful to the many staff members who helped me and I am especially grateful to Dr Evgeny Talantsev for his assistance in coated conductors synthesis and X-ray diffraction. Thank you to Dr James Storey for his help on so many levels and to Sarah Spencer for her support. I want to thank David Flynn, at Victoria University of Wellington (VUW), for his help with electron microscopy, and Martin Ryan and Dr Bridget Ingham, at Callaghan Innovation.

This work was funded by the Royal Society of New Zealand with a Marsden Fund. I consider myself lucky for having had the opportunity to work with many amazing scientists around the world. I want to thank Dr Takeshi Kasama from the Center for Electron Nanoscopy at the Technical University of Denmark (DTU Cen), Dr Sadegh Yazdi (now at Rice University, United States) and Dr James Loudon, from the University of Cambridge, for their technical assistance, and valuable discussions during my time at DTU Cen. The holography work presented in Chapter 5 would not have been possible without them. Thank you to Zoltán Balogh for training and help on specimen preparation using FIB-SEM. Thank you to Andrew Borrow and to all the staff members of DTU Cen for making me feel welcomed in your research centre.

I am very grateful to Dr Laure Bourgeois and Dr Peter Miller for generously welcoming me at Monash Centre for Electron Microscopy, Australia. Thank you to Dr Jisheng Ma and Dr Amelia Liu for their assistance in specimen preparation.

A special thanks to all my family and friends from either side of the world for their unconditional support, to the PhD students I met along the way that became friends. A great thank you to Sophie, Clarisse and Pauline, for never doubting me, to Geoff, Kristina,

Julia, Chris, Tushara, Sarah, Maryam, Camille, Simon, Hélène, Françoise, Laure, Judy, and Dale. Finally, I want to express my deepest thank you to Matt for his endless love, support and reassurance.

Table of contents

List of figures

List of abbreviations and acronyms

ADF	Annular dark field
AMSC	American Superconductor Corporation
BF	Bright field
BSCCO	$Bi_2Sr_2CaCu_2O_{8+x}$
BZO	$BaZrO_3$
CCD	Charged-coupled device
CSD	Chemical solution deposition
CVD	Chemical vapor deposition
DF	Dark field
DyBCO	Dysprosium barium copper oxide
EDS	Energy dispersive X-ray spectroscopy
(F)FT	(Fast) Fourier transform
FEG	Field-emission gun
FIB	Focused ion beam
FWHM	Full width at half maximum
HAADF	High-angle annular dark field
HRSTEM	High resolution scanning transmission electron microscope/microscopy
HRTEM	High resolution transmission electron microscope/microscopy
HT	High oxygenation temperature
HTS	High temperature superconductor
I(F)FT	Inverse (fast) Fourier transform
IT	Intermediate oxygenation temperature
JEMS	Java electron microscopy software
LT	Low oxygenation temperature
LTS	Low temperature superconductor
PIPS	Precision ion polishing system

PLD	Pulsed laser deposition
PPMS	Physical property measurement system
RABiTS™	Rolling-assisted biaxially textured substrate
REBCO	Rare-earth barium copper oxide
SAD	Selected area diffraction
SEM	Scanning electron microscope/microscopy
STEM	Scanning transmission electron microscope/microscopy
TEM	Transmission electron microscope/microscopy
TFA-MOD	Trifluoroacetate metal organic deposition
VSM	Vibrating sample magnetometer
XRD	X-ray diffraction
Y123	$YBa_2Cu_3O_7$
Y124	$YBa_2Cu_4O_8$
YBCO	Yttrium barium copper oxide
YSZ	Yttrium stabilised zirconia

List of symbols

Δf	Defocus
A	Electron wave amplitude
B	Magnetic field
B_c	Critical magnetic field
B_{c1}	Lower critical magnetic field
B_{c2}	Upper critical magnetic field
C_E	Constant that depends on the microscope acceleration voltage
e	Electron charge
$\hbar$	Reduced Planck constant
k	Wave vector
I_c	Critical current

$\boldsymbol{r}$	2D vector
s	Vortex spacing
t	Sample thickness
T_c	Critical temperature
V_0	Mean inner potential of the material
κ	Ginzburg-Landau parameter
λ	Penetration depth
μ	Interference fringes contrast
μ_0	Vacuum permeability
ξ	Coherence length
Φ_0	Flux quantum
φ	Electron wave phase
ψ	Electron wave function

Introduction

The discovery of high temperature superconductors (HTS) in 1986 by Bednorz and Müller [1] has been of great interest for industrial applications for the last three decades. Superconductor materials have the potential to play a key role in high-power applications such as energy transportation and generators due to the absence of electrical resistance in the material. Their practical operation above the liquid nitrogen boiling point (77 K), was also a great benefit for HTS compared to the low temperature superconductors (LTS) that require expensive liquid helium to be operational. The current method to fabricating the latest generation of long wire lengths of HTS, also referred to as coated conductors, is coating the superconductor material on a thin metal substrate. These wires have a high current carrying capacity in magnetic field and permit the reduction of device sizes [2]. However the range of application is still limited by the ability of the material to carry high currents and tolerate high magnetic fields [3] as well as the high manufacturing cost.

The ability of a superconductor to withstand high magnetic fields comes from its property to allow part of the magnetic field to penetrate it in the form of tubes of flux called vortices. This advantage comes with the inconvenience that the vortices tend to move under the influence of a transport current which limits the current carrying capacity. A way to compromise between these effects is to introduce non-superconducting defects into the material to pin the vortices in place and thereby enable the wires to support higher magnetic fields and electrical currents. This approach is already in use but the interaction phenomenon between the detailed material microstructure and the vortex lattice is still not fully understood. Also the concentration, distribution and type of defects desirable for optimising wire performance are still of great interest [3, 4] and lead to different electrical performance depending on the temperature regime.

The correlation between the material's microstructure (characterised via microscopy and diffraction) and its critical current is the most common approach to indirectly study vortex pinning phenomena in practical coated conductors.

A more direct way to understand vortex-defect interactions is to directly image vortices and defects using high-end transmission electron microscopy (TEM) techniques, which relies on the ability to image magnetic fields using the properties of electrons. Cowley reported several ways to do so [5], and the two that are of particular interest for vortex

imaging in superconductors are off-axis holography and Lorentz microscopy. The first of these was invented by Gabor in 1948 [6] and the second was mainly developed by Tonomura and his co-workers [7-9] providing new possibilities to study magnetic materials.

The present work comprises research on $YBa_2Cu_3O_{7-\delta}$ (YBCO) based superconductors as it is the most commonly used material in coated conductor technology. This thesis presents two distinct works undertaken to understand vortex pinning in YBCO: first the microstructural and electrical characterisation of practical YBCO superconducting wires. Pure YBCO samples were compared to samples with a Dy addition, as rare-earth addition is known to enhance YBCO-based coated conductor's properties [10]. Previous studies have shown increased critical current in YBCO with Dy addition [11, 12] and is the addition of choice in commercial superconducting wire [13]. Second the use of electron holography techniques using TEM to image magnetic vortices. It will be explained that the success in imaging vortices using electron holography techniques greatly relies on the TEM samples' structure and preparation, and therefore the experiments were carried out both on YBCO coated conductors and on YBCO crystals.

The thesis is organised in six chapters as follows. The necessary background and literature review are presented in Chapter 1 which begins with an introduction to high temperature superconductors and YBCO coated conductors relevant to the work. The YBCO structure and the common defects present in coated conductors are then presented. Conventional TEM was the main tool used to characterise the samples' microstructure and the techniques used are described in this chapter. An in-depth description of magnetic vortices is presented before finishing the chapter with an explanation of the off-axis holography and Lorentz microscopy techniques used to directly image magnetic vortices.

The experimental methodology is presented in Chapter 2. The procedure for YBCO coated conductor synthesis is first described, followed by details of the instruments and methods used for material characterisation: SEM and TEM for imaging, X-ray diffraction for phase analysis and crystalline structure determination and vibrating sample magnetometry was employed to determine magnetic properties of YBCO. Special care is also taken to describe TEM specimen preparation. Finally the electrical performance of the samples was also characterised by superconducting transport current measurements.

The structural and electrical characterisation results of the pure YBCO thin films are presented in Chapter 3. The effect of the oxygenation temperature on the samples microstructure and on the critical current is addressed. Then a similar study is conducted for samples with 50 % Dy addition in Chapter 4. At the end of the chapter, the microstructure and electrical results of the samples are compared to those of the pure YBCO.

The electron holography results are presented in Chapter 5. The two techniques, off-axis electron holography and Lorentz microscopy, were applied to both YBCO coated conductors and on YBCO crystal. The experimental challenges, progress and insights are presented in this chapter.

The final chapter presents a summary and general conclusions on the work achieved in this thesis.

Chapter 1 Background

This chapter presents the necessary background information for understanding vortex pinning defects in $YBa_2Cu_3O_{7-\delta}$ (YBCO) and vortex imaging. It starts with a general introduction to superconductivity and type II superconductors in particular. Coated conductors based on the superconductor YBCO are then presented, followed by a description of the YBCO crystal structure and its typical defects. Conventional transmission electron microscopy (TEM) is then presented for the purpose of imaging YBCO coated conductors structure, including imaging and diffraction mode, as well as scanning transmission electron microscopy (STEM) and 3D electron tomography. Vortex characteristics relevant to YBCO are then addressed before finally introducing electron holography techniques in TEM for vortex imaging.

1.1 Superconductivity

Superconductors have two fundamental properties when cooled below a critical temperature, T_c. First, they present no electrical resistance to a direct current flow, and, second, they expel magnetic fields from their interior by producing supercurrents circulating at the surface of the sample which exactly oppose externally applied fields. This latter effect is known as the Meissner effect [14].

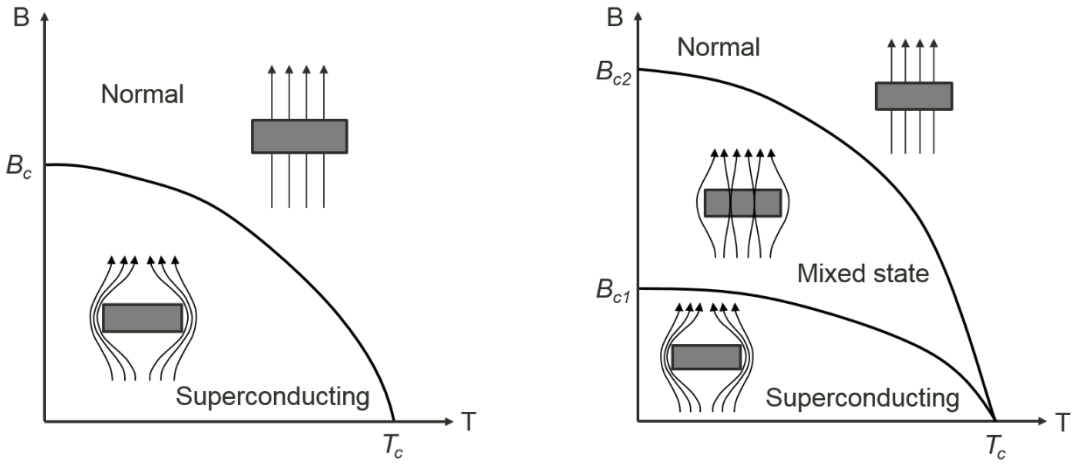

a) Type I superconductor b) Type II superconductor

Figure 1-1: Temperature dependence of the critical magnetic field describing the superconducting, normal and mixed states in a) type I and b) type II superconductors.

However, superconductors cannot expel an infinitely strong magnetic field, and are, as such, characterised by a critical magnetic field, B_c, above which the material loses its superconducting properties and reverts to the normal (non-superconducting) state (Figure 1-1). It is possible to distinguish two types of superconductors depending on how the superconductivity is lost. Type I superconductors (Figure 1-1a) present a sharp break down in their superconducting properties when subjected to a magnetic field higher than B_c. Type II superconductors (Figure 1-1b) allow the magnetic field to partially penetrate the superconductor in the form of vortices of magnetic flux, when subjected to a magnetic field above a lower critical magnetic field, B_{c1}. This is known as the mixed state. At a magnetic field higher than the upper critical magnetic field, B_{c2}, the superconductor completely loses its superconducting properties and reverts to the normal state. A representation of the structure of a flux vortex is shown in Figure 1-2.

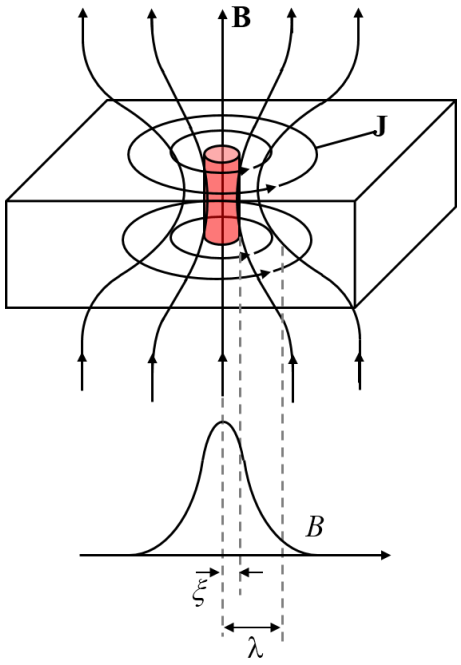

Figure 1-2: Structure of a magnetic flux vortex. The magnetic field B penetrates the superconductor, mostly within the vortex core of radius ξ (coherence length). Supercurrents J circulate around the vortex out to a distance λ (penetration depth) from the core, shielding the bulk of the sample from the magnetic field. Partially reproduced from [15] with permission from Elsevier.

Magnetic vortices are characterised by the radius of their non-superconducting core, equal to the coherence length, ξ, and by the penetration depth, λ, the distance over which the magnetic field, B, penetrates the superconductor. Supercurrents, J, flow around the vortices. Each vortex carries a single fluxon (also known as a flux quantum), given by:

$$\Phi_0 = \frac{h}{2e} = 2.07 \times 10^{-15}\ \text{Wb} \quad \textbf{(1.1)}$$

Applying a transport current to a type II superconductor generates a Lorentz force on the vortices $F_L = J \times B$ that creates vortex motion [16]. The motion of vortices in a superconductor is undesirable because it dissipates energy. However it is possible to pin the vortex in more energetically favourable locations. As mentioned above, the core of a vortex is non-superconducting, making non-superconducting defects in the material good pinning centres that hold the vortex in place, preventing its motion and therefore the corresponding dissipation of energy. A force, stronger than the Lorentz force, can hold the vortex in place and is called the pinning force, F_p. Even a region of slightly suppressed superconductivity can provide pinning.

The defects and precipitates described in section 1.3.2 contribute to vortex pinning. However the correlation between the defect landscape and the vortex pinning is still not fully understood.

1.2 YBCO coated conductors

High temperature superconductors (HTS) have been of great interest for practical applications since their discovery by Bednorz and Müller [1] with a T_c above 30 K. "Yttrium barium copper oxide" (YBCO) was the first HTS to exhibit superconductivity above the liquid nitrogen boiling point of 77 K and was discovered in 1987 by Wu [17]. It was soon followed by the discovery of superconductivity in similar materials. Its high critical temperature and its ability to withstand high magnetic fields make YBCO the superconductor of choice for future power applications such as energy transportation and generators, when fabricated in the form of wires. The wire's superconducting performance relies on the YBCO structure and composition. It was shown in the early stages of development that grain boundaries were greatly responsible for limiting the electrical performance of the material [18, 19]. This problem was overcome through use of the "coated conductor" technology, based on the epitaxial deposition of a superconducting film on a long metallic substrate.

1.2.1 Synthesis

To obtain a highly textured YBCO, several methodologies can be used such as pulsed laser deposition (PLD), chemical vapour deposition (CVD) [20] or chemical solution deposition (CSD) [21]. The latter is believed to be one of the cheapest [22], due to the absence of

high-vacuum and the possibility of deposition on long tapes, and is the method employed in this thesis. The YBCO is deposited on a rolling-assisted biaxially textured substrate (RABiTS) [23] supplied by American Superconductor (AMSC). A schematic of the coated conductor structure is presented in Figure 1-3. The substrate is a textured Ni-W alloy (with only 5 at% W [24], it will be referred to as the Ni substrate) with Y_2O_3, yttria stabilised zirconia (YSZ) and CeO_2 buffer layers. The first buffer layer, Y_2O_3, serves as an oxygen barrier between the Ni substrate and the YBCO, and is also used to enhance the epitaxy. The YSZ layer prevents reaction between the YBCO superconductor and the Ni. Finally, the CeO_2 cap layer is preferentially oriented to ensure epitaxial YBCO growth in the *c* direction [24].

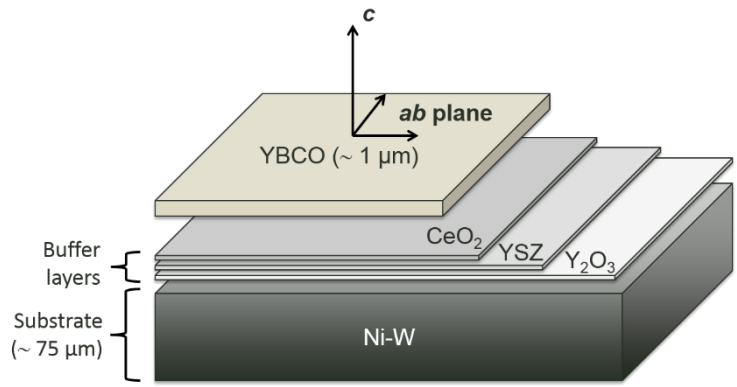

Figure 1-3: Schematic of the YBCO coated conductor structure.

The process of choice for the YBCO growth is the trifluoroacetate metal organic deposition (TFA-MOD) approach first developed by Gupta *et al.* [25] which gives thermodynamically stable and reproducible results [26]. The formation of YBCO thin films follows three main stages: decomposition, reaction and oxygenation. During the decomposition stage Y_2O_3, Ba-O-F and Cu-O form. During the reaction stage, $YBCO_{6.5}$ is formed from the reaction of Y_2O_3, Ba-O-F and Cu-O, and HF gas is released [27]. Finally, in the oxygenation stage, YBCO is oxidised forming $YBCO_{7-\delta}$ and stacking faults (SF). During the reaction stage, in addition to the $YBCO_{6.5}$ forming, Ba-Cu-O phases form through Cu-O and Ba-O-F reaction [4]. Y-Cu-O impurities may also be observed as its formation is concurrent to the one of Y_2O_3.

YBCO coated conductors have been characterised by a number of research groups and the effect of the synthesis procedure, such as the choice of precursors [25, 28, 29], the decomposition [29-35] and reaction [36-38] conditions have been widely studied.

However, little literature was found on the effect of the oxygenation temperature on the microstructure.

1.2.2 Electrical properties

The most important electrical characteristic of the YBCO wire is the critical current density, J_c. It is the maximum electrical current that the superconductor can support above which resistance appears [39], and that is attributed to the vortex motion mentioned in section 1.1. Usually the critical current drops quickly with increasing applied magnetic field and its largest value is for zero applied magnetic field. In this case, for low current passing through the superconductor, a small magnetic field is generated, lower than B_{c1}, and it is considered that no or little magnetic field penetrates through the superconductor. The critical current under no applied magnetic field is called the self-field critical current.

Another important property for practical applications is the irreversibility field. This is the magnetic field (lower than B_{c2} so the material is still superconducting) above which energy dissipation occurs due to the motion of the vortices and electrical resistance appears.

These characteristics are important as they define the material's practical limits, at specific temperatures and magnetic fields, beyond which dissipation occurs. In the worst case this dissipation can cause part of the superconductor to exceed T_c leading to runaway heating, known as a quench [40], and destroying the material.

1.3 Yttrium barium copper oxide

1.3.1 Structural characteristics

YBCO is a member of the cuprate material family and its basic form contains one yttrium (Y^{3+}), two barium (Ba^{3+}) and three copper ($Cu^{3+/2+}$) cations and the oxygen content may vary between 6 and 7 ($YBa_2Cu_3O_{7-\delta}$). When $\delta = 0.15$, the structure is orthorhombic and T_c is around a maximum of 93 K [17], but when $\delta > 0.6$, YBCO undergoes a structural transformation to tetragonal [41] and loses its superconducting property.

A schematic of the $YBa_2Cu_3O_7$ (Y123) crystal structure is presented in Figure 1-4. Its structure is generally described as a triple perovskite structure: a central $YCuO_3$ stacked between two $BaCuO_3$, with the oxygen vacancy mentioned above to give $YBa_2Cu_3O_{7-\delta}$. The central CuO_2-Y-CuO_2 section forms a "conduction block" and the outer CuO_2-BaO-CuO

sections form a "charge reservoir block". The presence of CuO chains and CuO_2 planes, specific to (Rare Earth)BCO (REBCO) materials, are proposed to be the source of their superconductivity [42].

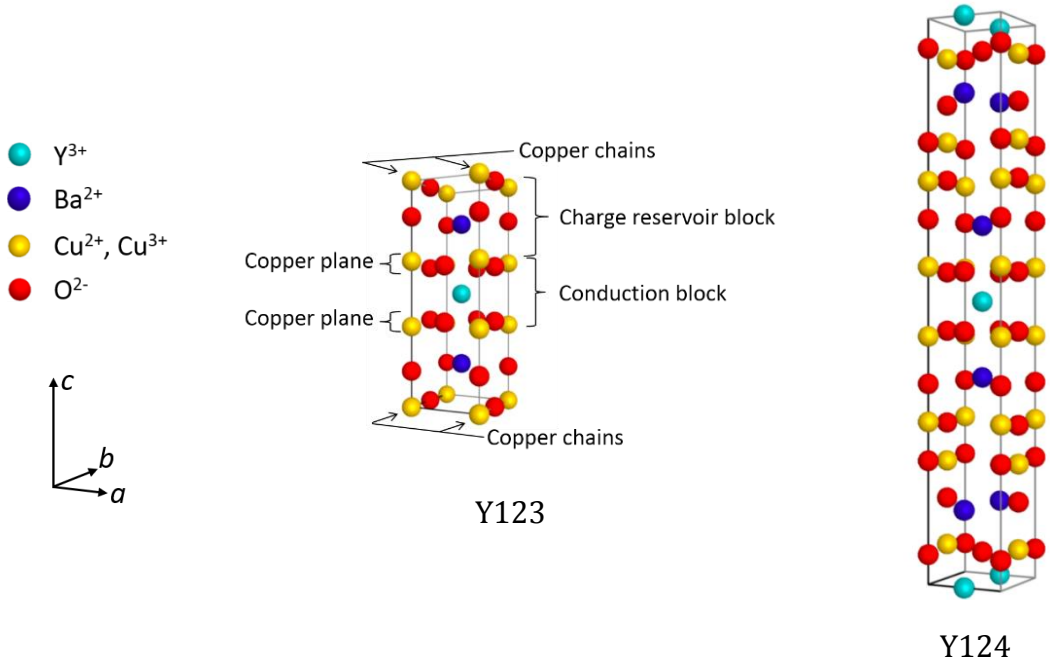

Figure 1-4: Crystal structure of $YBa_2Cu_3O_7$ (Y123) and $YBa_2Cu_4O_8$ (Y124). The structures were created using the JEMS software package [43] with the structural details from reference [16].

Alongside Y123, it is useful to introduce the structure of $YBa_2Cu_4O_8$ (Y124) and to compare its structural configuration to Y123. Y124 is described using two Y123 unit cells with two stacking differences. Every successive Y123 unit cell is shifted half a unit cell in the *b* direction, and between each cell are located two planes of Cu-O (instead of one) [44].

Previous research has shown that addition or substitution of Y by other rare-earths is effective in increasing the critical current [11, 45, 46]. The added rare-earth in this thesis is Dy, therefore $DyBa_2Cu_3O_7$ (DyBCO or Dy123) is presented for comparison. The structure is similar to YBCO, with the Dy substituting the Y. Its unit cell and critical temperature are very similar to the Y123 (Table 1-1). This small difference can be expected due to the small difference of ionic radius between Y^{3+} (1.019 Å) and Dy^{3+} (1.027 Å) [47]. Dy124 and Y124 are even more similar (See Table 1-1), although Dy124 presents a lower critical temperature (77 K), and all have an orthorhombic structure.

Maximum critical temperatures for YBCO and DyBCO crystals are reported to be around 93 K and 94 K respectively, however usual values reported for YBCO coated conductors are around 90 K.

Table 1-1: YBCO and DyBCO lattice parameters and critical temperature, with references.

	Y123 [41]	**Dy123 [48]**	**Y124 [16]**	**Dy124 [49]**
a	0.3823 nm	0.3818 nm	0.3841 nm	0.3846 nm
b	0.3887 nm	0.3884 nm	0.3871 nm	0.3873 nm
c	1.1680 nm	1.1649 nm	2.721 nm	2.7237 nm
T_c **(K)**	90-93 [17, 50, 51]	94 [48]	80 [49]	77 [49]

1.3.2 Defects and precipitates in YBCO coated conductors

A wire containing a perfectly ordered YBCO structure does not exhibit the highest critical current, because a certain amount of disorder and defects is beneficial for vortex pinning [4]. YBCO wires that are used in engineering devices, such as HTS magnets, will be subjected to a range of magnetic field strengths and magnetic field angles at any one time. Pinning centres that improve the critical current for specific applied magnetic field angles are described as anisotropic while those that increase the critical current at all field angles are called isotropic. As such, for practical application, it is critical that the isotropic pinning of the wire is optimised. Due to the YBCO structure previously presented and the epitaxial growth on the substrate, the YBCO films exhibit "intrinsic" pinning centres. The non-superconducting planes, as the Ba-O plane in the conduction block (Figure 1-4) for example, are source of pinning that is intrinsic to the structure. "Extrinsic" pinning defects can be added due to the synthesis process and provide additional pinning. The ideal synthesis technique therefore not only creates an epitaxial YBCO film, with low grain to grain misorientation, it also introduces nano-sized defects which pin the magnetic vortices and consequently improve the current carrying capacity of the wire. These nanoscale defects may be introduced either by a change in the global stoichiometry, a local change in stoichiometry or intentional nanoparticle additions.

When considering defects it is of interest to know the nature, size and distribution of the defects to correlate them with the coherence length of the vortex as mentioned in section 1.1.

1.3.2.1 Nanoparticle inclusions

A variety of nanoparticles inclusions have been added to YBCO films to enhance the critical current under applied magnetic fields [3]. They are described as three-dimensional pinning centres and they contribute to increasing the isotropic critical current. Common nanoparticles additions are: Y_2O_3, RE_2O_3 (such as Dy_2O_3, $BaMO_3$ perovskites (with M typically being Zr [12, 51-54], but also Sn [55] or Hf [56])). These nanoparticles may either be added as cation additions to the precursor solutions, by inclusion of nanoparticles in the YBCO matrix using pulsed laser deposition [57, 58], or as already formed nanoparticles which are then dispersed during YBCO thin film growth [59]. Yttria (Y_2O_3) nanoparticles also form because of deviation from the Y:Ba:Cu 1:2:3 stoichiometry [4].

Rare earth ion may also be added at the precursor stage to generate RE_2O_3 nanoparticles in the YBCO thin films [12, 60-62]. In the case of Dy additions to the precursor, the final nanoparticles are likely to contain a mixture of Y and Dy making $(Y,Dy)_2O_3$ as reported by several studies [60, 61]. However Ortalan e*t al.* [63] report that they observed $(Y,Dy)_2Cu_2O_5$ particles forming in films, using an MOD process, that tend to congregate at the twin boundaries.

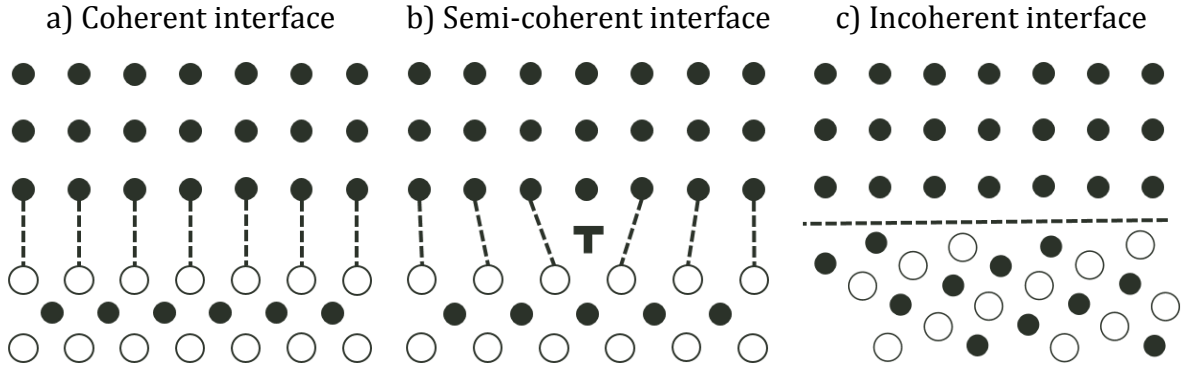

Figure 1-5: Schematic of a) coherent, b) semi-coherent and c) incoherent interface between two adjacent phases.

Although the composition, size and distribution of the nanoparticles is of interest, Llordés *et al.* [64] propose that a non-homogeneous strain created by an incoherent interface between the nanoparticles and the YBCO matrix is also a key parameter for isotropic vortex-pinning control. Coherency between two adjacent phases is illustrated in Figure 1-5. A perfect lattice matching between two phases would give a coherent interface, but it generally results in lattice strain for at least one of the two phases.

Dislocations may appear at the interface of one of the phase to relieve part of the strain, leading to a semi-coherent interface. For configuration with no lattice matching, the interface is defined as incoherent.

Llordés *et al.* [64] investigated $BaZrO_3$ (BZO) nanoparticle addition in a YBCO film grown using chemical solution deposition. They observed YBCO lattice straining in the region surrounding the particles as another contribution to vortex pinning. Strain has been observed in the YBCO matrix when the lattice mismatch between the nanoparticle inclusion and the YBCO matrix is large [3]. For example, YBCO lattice strain was observed around BZO inclusions where the lattice mismatch is about 9 % [65] while no YBCO lattice strain was observed around Y_2O_3 nanoparticles, where the lattice mismatch is about 2.5 % [66].

This raises the question of whether it is better to grow smaller nanoparticles that are greatly incoherent with the YBCO bulk and whether nanoparticles alone are not enough to increase the pinning in the material but also have to be incoherent with the YBCO matrix. Studies have shown that even nanoparticles that do not provide nanostrain in the adjacent YBCO, still do contribute to an improved critical current [56, 65, 66]. Despite this, although nanoparticles are beneficial for vortex pinning at 77 K, they do not have much effect at low temperature because of the reduction of the thermal fluctuations [12].

1.3.2.2 Stacking faults

The stacking fault is an anisotropic defect, which is defined in YBCO either as an extra CuO plane stacked between two Y123 layers [44, 67], or as an inclusion of Y124 phase stacked between Y123 layers [68, 69]. Nevertheless, a stacking fault is an extra non-superconducting Cu-O plane in the charge reservoir block that provides vortex pinning for a magnetic field applied along the *ab* plane.

If the stacking fault is defined as Y124 phase between Y123, this would provide a clear way to distinguish whether the phase is in a [010] or a [100] orientation [70]. Figure 1-6 shows projections of Y123 and Y124 in the [010] and [100] directions.

In high resolution transmission microscopy imaging (HRTEM), the oxygen atoms do not provide sufficient scattering to produce contrast and as such are not imaged, this makes viewing down the [010] and the [100] direction for Y123 visually indistinguishable. However, the presence of a stacking fault defined as Y124 can give direct information on the YBCO orientation because of the shift in the *b* direction of the Y124 structure. The

double CuO chain layer presents a square or a triangular alignment when orientated in the [010] or the [100] direction respectively [70, 71].

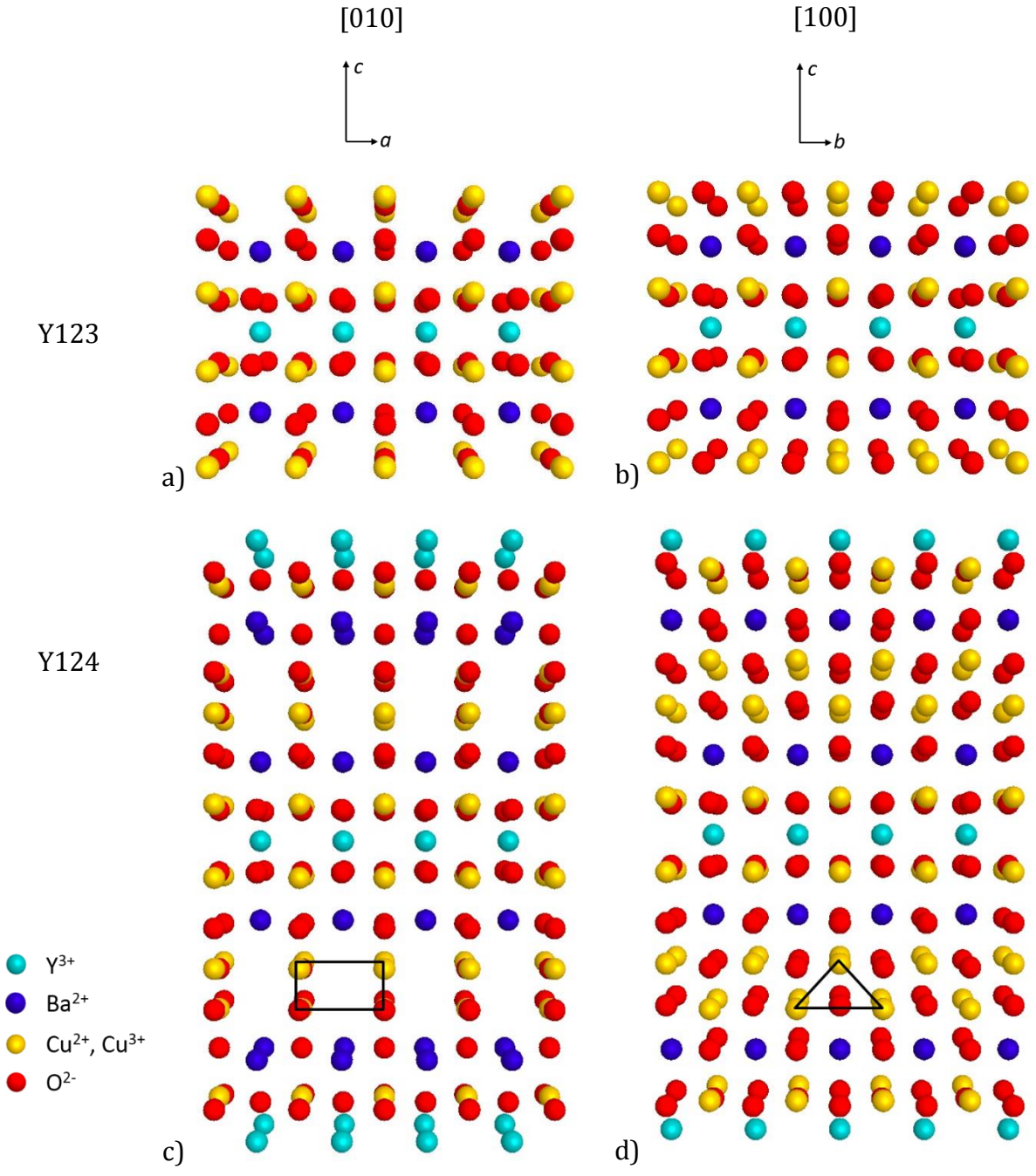

Figure 1-6: Y123 and Y124 crystal structures in the [010] and [100] projections.In the absence of contrast provided by the O atoms, the two directions are indistinguishable for Y123. In contrast, in the Y124 structure, the presence of the extra CuO plane, arranged in rectangular or triangular configuration, allows to discern [010] and [100] projection respectively. The structures were created using the JEMS software package [43].

1.3.2.3 Twin boundaries

Twin boundaries are very common defects in the YBCO structure both in coated conductors and YBCO crystals. It easily occurs because of the small difference between the *a*-axis and *b*-axis lattice parameters. Twin boundaries appear when the crystal orientation switches from *a* to *b* in a mirroring way. Twinning in YBCO is also related to oxygen deficiency in some regions [72] that leads to the change of orientation. It has been shown that twin boundaries contribute to vortex pinning as a two-dimensional pinning centre [27, 73].

1.3.2.4 Dislocations

Different types of dislocations can be described in YBCO thin films: threading dislocations occur where grains are misoriented and misfit dislocations can be observed at the interface between the YBCO and the substrate leading to extra or missing planes of atoms [3, 74]. Dislocations are considered one-dimensional pinning centres due to their long range in one direction [27].

1.3.2.5 Impurity phases

Ba-Cu-O phases are observed in YBCO coated conductors, and their formation is believed to originate from trapped liquid YBCO phases within "rigid" YBCO during the growth process [4]. The YBCO then react with Cu-O and form Ba-Cu-O phases. Ba-Ce-O phases have been found in thin films near the buffer layer when the CeO_2 reacts with the YBCO [75]. Those non-superconducting phases contribute to reducing the coated conductor critical current.

1.4 Conventional imaging using transmission electron microscopy

This section aims to introduce conventional imaging using TEM, before introducing TEM-based electron holography techniques in Section 1.6. A large number of textbooks explain TEM principle and alignment, such as the one of D. Williams and C. Carter [76]. The following section is a summary of TEM and STEM principle for imaging YBCO coated conductors.

1.4.1 TEM and STEM

A simplified schematic of the image formation in conventional TEM mode is shown in Figure 1-7. An electron beam is transmitted through a thin specimen under vacuum to form an image. The incident electrons are focused on the specimen with a series of condenser lenses and then the objective lens creates a first inverted image. Intermediate and projector lenses magnify and create the final image which is acquired by a charge-coupled device (CCD) camera.

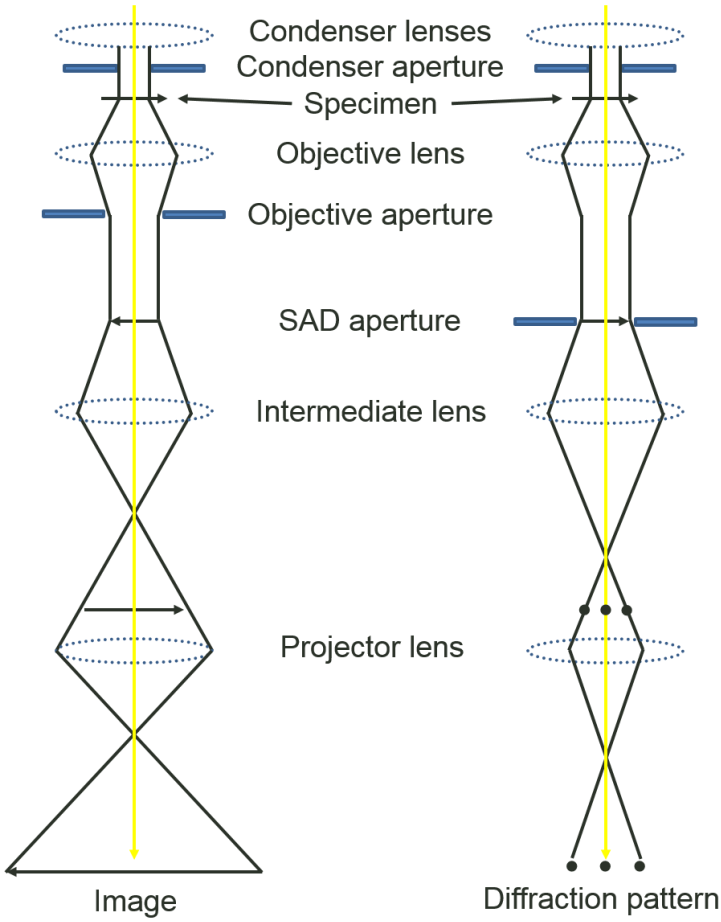

Figure 1-7: Simplified schematic of a transmission electron microscope in imaging mode (left) and diffraction mode (right).

In conventional TEM micrographs the image intensity reflects the electron wave amplitude. The electron beam amplitude is modified as it travels through the specimen because of the interaction of the electrons with the atoms of the specimen. The diffracted intensity variation caused by the specimen is due to absorption, dynamic scattering or microstructural features and give the amplitude contrast.

A TEM can also be used in diffraction mode to extract crystallographic information. In this configuration (Figure 1-7), the intermediate lens strength is adjusted to display the electron diffraction pattern. For selected area diffraction (SAD) work, a selected area aperture is introduced to both select a zone of interest in the specimen and to reduce the electron beam intensity to avoid damaging the CCD camera. The SAD provides crystal structure and orientation information. For perfectly aligned and defect free structures, the SAD spots are sharp and bright reflections. When structural distortion exists, such as stacking faults or a lattice parameter change, the reflections appear broader or more diffuse.

In STEM mode, as the name scanning suggests, the electron beam is scanned over the specimen's surface. This requires the electron beam to be focused to a fine probe on the specimen and beam deflectors are used to scan the beam. Images are then recorded using various detectors depending on the way the electrons scatter. The electrons directly transmitted (limited/no beam diffraction or scatter) can be collected in a bright field (BF) detector giving BF images. The scattered/diffracted electrons can be collected by an annular dark field (ADF) detector producing dark field (DF) images. Finally, electrons which scatter to high angles can be collected in by a high angle annular dark field (HAADF) detector. This final mode produces Z-contrast images and is used to emphasise atomic number variations in the specimen. In HAADF images, areas with high atomic number produce more scatter and consequently appear brighter than low atomic number regions.

High resolution (HR) imaging can be achieved in both TEM and STEM modes. One of the advantages of HRSTEM is that it gives access to the Z-contrast at high magnifications and resolutions, while HRTEM images are dependent on the focus and specimen thickness. However due to the electron beam being focused in a fine probe on the specimen, HRSTEM can be difficult for beam sensitive samples. The resolution given by microscopes is nevertheless limited by spherical and chromatic aberration of the electromagnetic lenses. High-end TEMs can now be equipped with monochromators and aberration correctors to reach resolutions below 1 Å.

1.4.2 3D electron tomography

Tomography is a technique that gives access to 3D information of a volume section by section using any kind of wave such as X-rays, gamma-rays or electron. Electron

tomography, used in TEM, is a four-step process. First a tilt series is recorded, by acquiring STEM images of the specimen at incremental angles around the area of interest. Then the stack of images in the tilt series is aligned along the tilt axis to correct the misalignment between each of the images due to the tilt. The third step is the "reconstruction" and consists in the creation of a 3D volume with frames in xy, xz and yz planes from the stack of the tilt STEM images. Finally the segmentation is the visualisation in 3D of the features of interest.

With 3D electron tomography, it is possible to see the three-dimensional distribution, size and shape of nanoparticles or inclusions and pores within a solid sample.

To date, little 3D TEM tomography work has been done on REBCO coated conductors [63, 77, 78]. Nishiyama *et al.* showed randomly and homogeneously dispersed nanoparticle inclusions of BZO, sized between 100-200 nm, in Gd-doped YBCO [77]. Ortalan *et al.* report the growth of $(Y,Dy)_2Cu_2O_5$ nanoparticles, sized 13-135 nm and located between twin boundaries, in Dy-doped YBCO thin films prepared using a slot die coating technique [63]. Both studies report an improvement of the isotropic vortex pinning of the coated conductors due to the nanoparticles inclusions.

1.5 Vortex characteristics in YBCO

The theoretical size, shape and distribution of the magnetic vortices in YBCO and the dependence of these factors on sample temperature and applied magnetic field is important to understand vortex-defect interaction in type II superconductors.

As described in section 1.3.1, YBCO is an anisotropic superconductor with a nearly tetragonal crystal structure with $a \approx b \neq c$. As such, the coherence length and the penetration depth also exhibit anisotropy with respect to the crystallographic structure of the YBCO, giving $\xi_a \approx \xi_b \neq \xi_c$ and similarly $\lambda_a \approx \lambda_b \neq \lambda_c$.

The observed vortex cross-section is therefore circular when the vortex lies along the *c*-axis, while vortices lying normal to the *c*-axis have an elliptical cross-section [16, 79]. In this work, the specimens were only prepared with the *ab* in-plane for vortex observation in Chapter 5 and the penetration depth, λ, in the text always refers to λ_{ab}.

1.5.1 Penetration depth

It is critical to understand λ as this determines the size of the observed vortex for observation using electron holography techniques. The penetration depth of a

superconductor varies with temperature [80, 81]. For example in YBCO, for temperatures varying from 5-40 K λ is found to range between 100-250 nm. It is therefore considered more useful to consider λ at the low temperature limit, $\lambda(0)$, (λ at 0 K) from which λ at other operating temperatures can be calculated using the following equation [82]:

$$\lambda(T) = \frac{\lambda(O)}{\sqrt{1 - \left(\frac{T}{T_c}\right)^{4/3}}} \qquad \textbf{(1.2)}$$

where T_c is the critical temperature of the superconductor.

Several $\lambda(0)$ values for YBCO found in the literature are summarised in Table 1-2. In practice, λ is measured at different temperatures down to about 4 K, then $\lambda(0)$ is extrapolated using Equation (1.2). The low temperature penetration depth for YBCO typically falls around 140 nm for most of the techniques, except for far infrared transmission and surface impedance techniques which gave a higher value of λ = 180 nm.

Table 1-2: Experimental values of the low-temperature penetration depth, $\lambda(0)$, of YBCO obtained using different techniques.

$\lambda(0)$ (nm)	**Technique**	**Year of publication – Reference**
140 ± 9	Muon spin spectroscopy	1993 – [83]
144	Infrared spectroscopy	1994 – [84]
155	Muon spin spectroscopy	1995 – [85]
140 ± 10	Polarised neutron reflectometry	1998 – [86]
139-146	Tunnel diode resonator	2000 – [87]
180 ± 20	Far infrared transmission and surface impedance	2002 – [88]

Figure 1-8 shows that at low temperature the vortex penetration depth varies little with temperature (~150 nm at 20 K). It is also important to remember that λ is dependent on temperature, but independent of applied magnetic field at low fields [89].

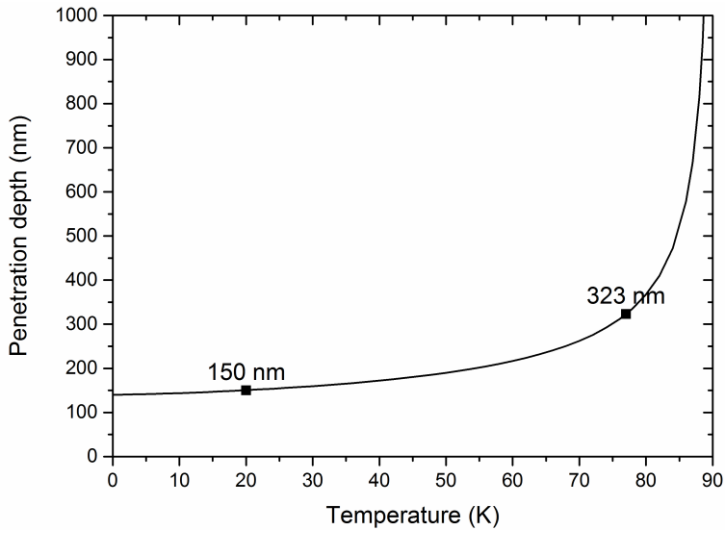

Figure 1-8: Penetration depth λ_{ab} of YBCO as a function of temperature using equation (1.2), with $\lambda(0)$ = 140 nm.

1.5.2 Coherence length

It is interesting to know the value of the coherence length in YBCO in the *c* direction and in the *ab* plane, as well as its dependence on temperature, as it will determine the optimal size of defects in the coated conductors.

The in-plane coherence length ξ_{ab} range, at different temperature, found in the literature for YBCO is summarised in Table 1-3.

Table 1-3: Experimental values of the in-plane coherence length ξ_{ab} for YBCO.

ξ_{ab} (nm)	Temperature	Year of publication - Reference
1-4	10-90 K	2004 – [80]
1-5	5-40 K	2007 – [81]
1.6	not specified	1994 – [90]
1.8	not specified	1988 – [16]

Along the *c*-axis, the coherence length is reported to be ξ_c = 0.3 nm [16].

The coherence lengths, in the *ab* plane and along the *c*-axis, as a function of temperature were calculated. On one hand, ξ_{ab} was determined using the Ginzburg-Landau parameter κ, and λ_{ab} from equation (1.2):

$$\kappa = \frac{\lambda_{ab}}{\xi_{ab}} \qquad \textbf{(1.3)}$$

In type II superconductors, the penetration depth is much larger than the coherence length and κ = 95 for pure YBCO [16].

On the other hand, the *c*-axis coherence length ξ_c was calculated using the following equation [16]:

$$\xi_c(T) = \frac{\xi_c(0)}{\sqrt{1 - \frac{T}{T_c}}} \qquad \textbf{(1.4)}$$

Figure 1-9 shows the coherence length as a function of the temperature along the *ab* plane and along the *c*-axis.

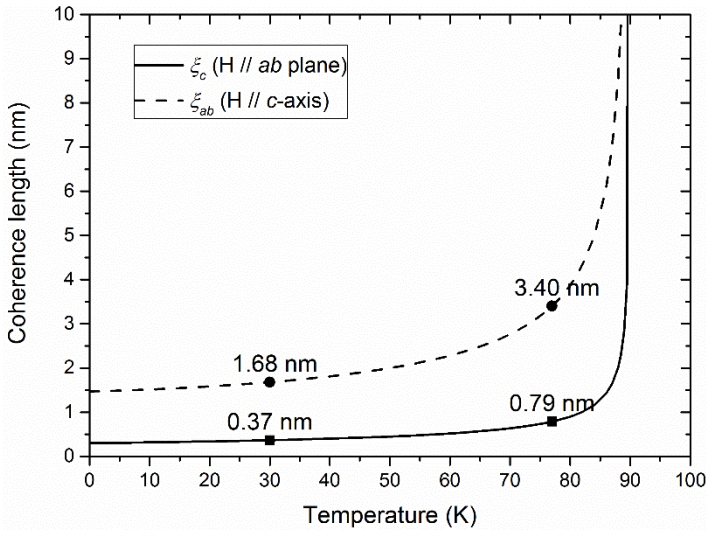

Figure 1-9: Coherence lengths, ξ_{ab} and ξ_c, in YBCO as a function of temperature calculated using equations (1.3) and (1.4) respectively. For both directions, ξ is two times larger at 77 K than at 30 K.

It is interesting to consider these coherence length sizes to correlate it to the size of defects in the material. Larger defects are required to pin a vortex for a magnetic field applied in the *c* direction than in the *ab* plane. In addition, at 77 K, a 7 nm sized defect is required to pin a vortex (for *H* // *c*-axis) while when the temperature is reduced, a smaller defect is necessary. Finally, the vortices are greatly elongated in the applied magnetic field direction compared to their small coherence length. Therefore depending on the magnetic field orientation, pinning defects will act as strong or weak pinning centres. Two-dimensional defects (such as dislocations or stacking faults mentioned in section 1.3.2) will act as strong pinning centres for magnetic field applied along the defect's long length direction. However small three-dimensional defects, of a size smaller than ξ, are only a source of weak pinning.

1.5.3 Vortex spacing

In the case when no pinning is occurring due to a lack of defects, as it would be the case in a perfect YBCO crystal, the vortices arrange themselves in a regular array in an hexagonal configuration. Unlike λ and ξ, the vortex spacing, s, is dependent on the applied magnetic field, but independent of temperature [15, 91] and can be calculated using:

$$s^2 = \frac{2\Phi_0}{\sqrt{3}B} \qquad \textbf{(1.5)}$$

where s is the vortex spacing (m) and B is the applied magnetic field (T).

Figure 1-10 is a plot of s as a function of applied magnetic field. In this work, for in-situ vortex imaging experiments using electron holography in the TEM, the experimental applied magnetic field range is from 5 to 1000 mT. Due to the inverse square root dependence of the vortex spacing on magnetic field, at low magnetic fields the vortex spacing is strongly dependent on magnetic field (at 5 mT the vortex spacing is about 690 nm), whereas at high magnetic fields the vortex spacing is only weakly dependent on magnetic field (at 800 mT the vortex spacing is 54 nm).

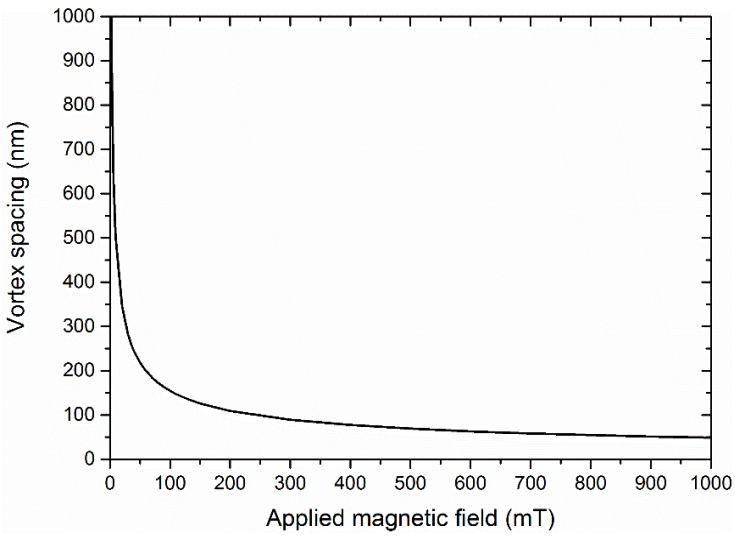

Figure 1-10: Vortex spacing as a function of the applied magnetic field for a hexagonal vortex configuration in the absence of pinning, calculated from equation (1.5).

1.6 Vortex imaging using TEM electron holography techniques

This section is an introduction to electron holography using TEM. The principle of the two techniques of electron holography that are used in this thesis, Lorentz microscopy and off-axis electron holography, are explained in the context of imaging vortices in superconducting materials. More details about the techniques and other applications of electron holography can be found in various references [9, 92, 93].

1.6.1 Principle of electron holography

Denis Gabor invented electron holography in 1948 [6] as a method to improve TEM resolution by correcting lens aberrations. In conventional TEM micrographs, the image intensity reflects the electron wave amplitude, but the phase information is lost. With electron holograms both the electron wave phase and intensity are recorded. Cowley reviewed twenty ways of utilising the wave properties of electrons by holography methods [5]. There are two main types of electron holography: high resolution electron holography and medium resolution electron holography. The former allows for aberration correction of high resolution images, while the latter allows magnetic and electric field information in a material to be obtained. To acquire electron holograms, the TEM must be equipped with a highly coherent electron beam such as a field-emission electron gun (FEG).

In this thesis, medium resolution electron holography is the technique of interest. There are two main types of medium resolution electron holography techniques for imaging vortices in superconductors: off-axis and in-line electron holography as shown in Figure 1-11.

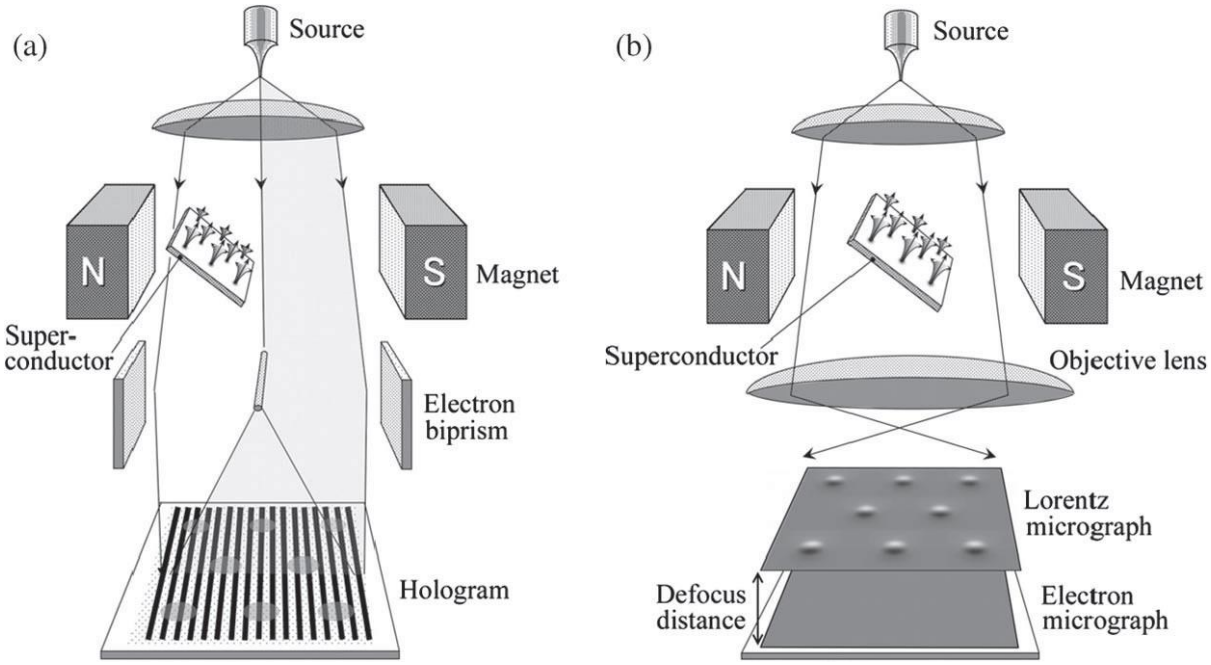

Figure 1-11: Optical systems for vortex observation a) off-axis electron holography where the electron beam passes through the superconductor and the vacuum, giving two electron waves that are then overlapped by the electron biprism to produce the hologram, and b) in-line electron holography (or Lorentz microscopy) where a defocus is applied to observe the vortices. Image reproduced from [7] © 2013 IEEE.

1.6.2 In-line electron holography (Lorentz microscopy)

In-line electron holography (Figure 1-11b), which will be referred to as Lorentz microscopy throughout this thesis, permits dynamic observation of vortices in superconductors. To conduct a Lorentz microscopy experiment, the TEM needs to be equipped with a Lorentz lens to defocus the image allowing the observation of the vortices. The objective lens can be used to introduce vortices by applying a magnetic field to the sample. Qualitative information is extracted from this technique and vortex migration can be observed. Quantitative information can be extracted by simulating the Lorentz micrographs [94, 95].

With this technique the vortices are not visible when the image is in focus and are observed only by applying a large defocus to create contrast. The vortices appear as bright and dark round features, also called globules by some authors [96]. A schematic of how an overfocused ($+\Delta f$) Lorentz micrograph is formed is shown in Figure 1-12. In an out-of-focus image, the component of the magnetic field, **B**, associated with the vortices, that is perpendicular to the electron beam, deflects the electrons [97] creating a region with an increased electron intensity (bright) and a region with a decreased electron

intensity (dark) below the vortex [15]. As such, the vortices appear as adjacent bright and dark features in the micrograph.

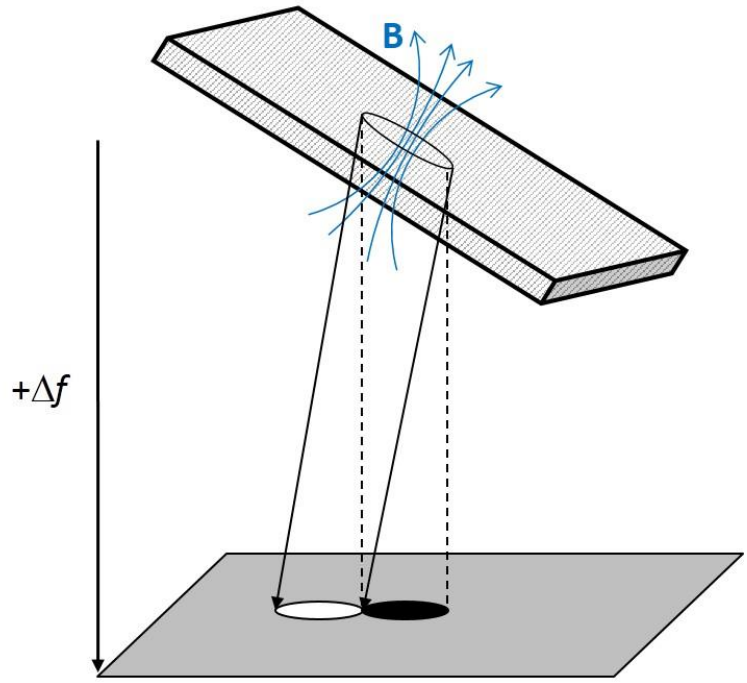

Figure 1-12: Schematic of out-of-focus images of vortices obtained by Lorentz microscopy. The applied magnetic field B passes through the superconductor at the core of the vortex. When a defocus Δ*f* is applied, the vortex appears in the micrograph as adjacent bright and dark features.

Belaggia *et al.* [94, 95] showed that the contrast of the vortex varies with the applied defocus. In this work, Lorentz microscopy was used to visualise the vortices in real time and to find the experimental conditions (temperature, applied field, specimen preparation) allowed for vortex observation.

1.6.3 Off-axis electron holography

In off-axis electron holography (Figure 1-11a), part of the electron beam passes through the sample, referred to as the object wave, and the remainder passes through the adjacent vacuum, referred to as the reference wave. The TEM is equipped with a biprism, which is positioned in the selected area aperture, and is used to overlap the two electron waves and form the hologram. The objective lens is used to apply a magnetic field as for Lorentz microscopy. Quantitative information about magnetic and electric fields can be obtained from this off-axis technique. Off-axis holography is an indirect magnetic field imaging technique and requires post-processing image analysis, termed hologram reconstruction, before information about magnetic or electric field variations can be extracted.

The following sections describe hologram formation, hologram reconstruction and magnetic field calculations [92, 98, 99].

1.6.3.1 Hologram formation

To understand the hologram reconstruction process, it is useful to know the intensity distribution in conventional bright field TEM images and compare it with electron holograms. As reviewed by Lichte, the electron wave interacts with materials following the principles of wave optics [98]. In the image plane, the electron wave function can be expressed as:

$$\psi_i(\boldsymbol{r}) = A_i e^{i\Phi_i(\boldsymbol{r})} \quad \textbf{(1.6)}$$

where A is the amplitude of the electron wave function, Φ its phase and $\boldsymbol{r}$ a two-dimensional vector in the sample plane.

As previously mentioned, in conventional TEM imaging, the phase information is lost and only the intensity remains which can be written as:

$$I(\boldsymbol{r}) = |A_i(\boldsymbol{r})|^2 \quad \textbf{(1.7)}$$

However in electron holography, the recorded hologram contains the phase information and the expression of the hologram intensity is:

$$I_{hol}(\boldsymbol{r}) = \psi_{hol}(\boldsymbol{r}).\psi^*_{hol}(\boldsymbol{r}) \quad \textbf{(1.8)}$$

where ψ_{hol} is the sum of the object and the reference wavefunctions as expressed in equation (1.9) and ψ^*_{hol} its complex conjugate.

$$\psi_{hol}(\boldsymbol{r}) = A_o e^{i(2\pi \boldsymbol{k}_o.\boldsymbol{r}+\Phi_o(\boldsymbol{r}))} + e^{i(2\pi \boldsymbol{k}_r.\boldsymbol{r}+\Phi_r(\boldsymbol{r}))} \quad \textbf{(1.9)}$$

where A_0 is the object wave amplitude, Φ_o and Φ_r are the object and the reference wave phase respectively and $\boldsymbol{k}_0$ and $\boldsymbol{k}_r$ are the wave vectors of the object and the reference wave respectively.

Substituting equation (1.9) into equation (1.8) the hologram intensity is expressed with the object wave amplitude, and the object and reference wave phases:

$$I_{hol}(\boldsymbol{r}) = 1 + A_o^2(\boldsymbol{r}) + 2\mu A_o(\boldsymbol{r}).cos[2\pi q_c.\boldsymbol{r} + \phi_o(\boldsymbol{r}) - \phi_r(\boldsymbol{r})] \quad \textbf{(1.10)}$$

where $q_c = \boldsymbol{k}_0 - \boldsymbol{k}_r$ is the carrier fringe frequency, and μ is the contrast of the interference fringes which can be written as:

$$\mu = \frac{I_{max} - I_{min}}{I_{max} + I_{min}} \quad \textbf{(1.11)}$$

where I_{max} and I_{min} are the maximum and the minimum intensities of the holographic fringes respectively.

An example of an interference micrograph recorded without a specimen is shown in Figure 1-13a. The phase information is contained in the hologram interference fringes, which, therefore, have to be well-formed for a better hologram reconstruction. The width of the area over which the reference wave and the specimen wave interfere is called the overlap width. This parameter determines the width of the studied area in the specimen and can be referred to as the field of view in the case of off-axis holography.

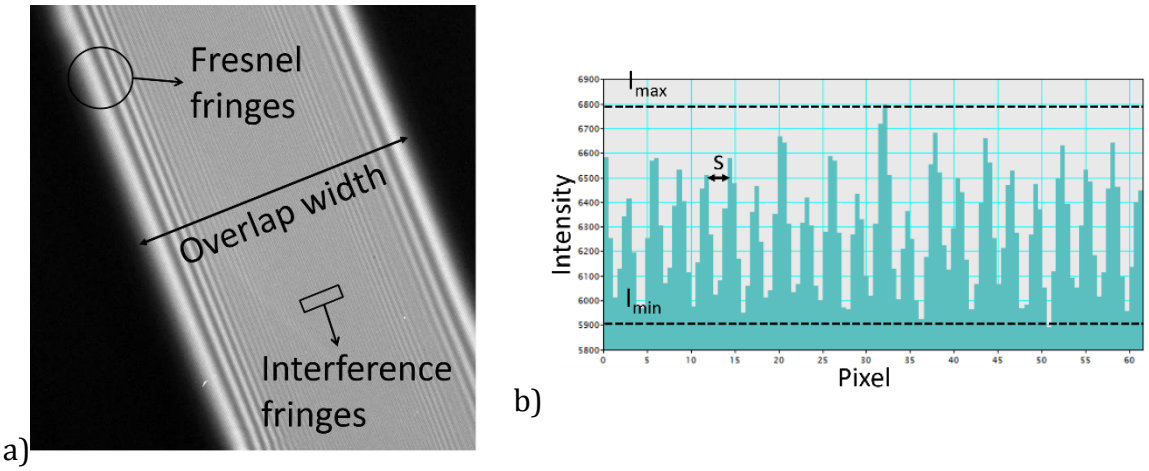

Figure 1-13: a) Off-axis electron hologram recorded in the vacuum as a reference where Fresnel fringes and interferences fringes can be seen. b) The intensity profile showing the spacing and the intensity maximum and minimum (I_{max} and I_{min}) of the interference fringes (rectangular area in a).

The overlap width increases with the biprism voltage. However, increasing the overlap width increases the number of fringes, consequently decreasing the fringe contrast and spacing $s = \frac{1}{q_c}$ (Figure 1-13b) [99].

1.6.3.2 Hologram reconstruction

To be able to extract phase information from an off-axis hologram, the hologram needs to be reconstructed. There are four main steps in hologram reconstruction (illustrated in Figure 1-14):

1. a Fourier transform (FT) of the hologram is taken;
2. one side band of the FT is selected using a mask;
3. an inverse Fourier transform (IFT) is applied to get the complex image;
4. the phase image and the amplitude image are extracted from the complex image.

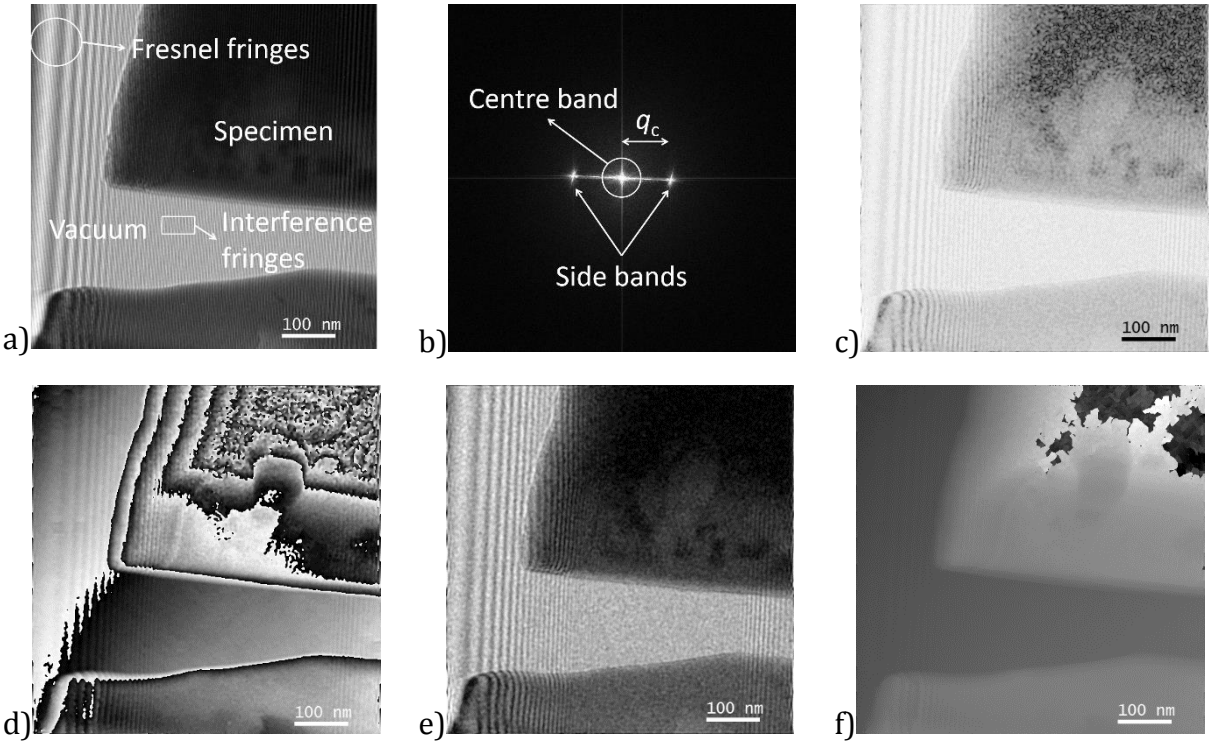

Figure 1-14: Hologram reconstruction basic steps a) electron hologram of a YBCO thin film with visible Fresnel and interference fringes, b) Fourier transform of the electron hologram showing side bands at a distance q_c from the centre band, c) the complex image, d) the phase image, e) the amplitude image and f) the unwrapped phase image.

An example hologram obtained on a YBCO thin film is shown in Figure 1-14. The dark areas of the hologram (Figure 1-14a), are the specimen and the bright area with visible Fresnel and interference fringes is the vacuum. The first step in reconstruction is to take a FT (Figure 1-14b) of the hologram to get a frequency spectrum which can be expressed from (1.10) as:

$$\begin{aligned} \boldsymbol{FT}[\boldsymbol{I_{hol}}(\boldsymbol{r})] = \boldsymbol{FT}\left[\boldsymbol{A_o^2}(\boldsymbol{r})\right] \\ + \boldsymbol{\delta}(\boldsymbol{q}+\boldsymbol{q_c})\otimes \boldsymbol{\mu FT}\left[\boldsymbol{A_o}\,(\boldsymbol{r}).\,\boldsymbol{e}^{\boldsymbol{i}[\boldsymbol{\Phi_o}(\boldsymbol{r})-\boldsymbol{\Phi_r}(\boldsymbol{r})]}\right] \\ - \boldsymbol{\delta}(\boldsymbol{q}-\boldsymbol{q_c})\otimes \boldsymbol{\mu FT}[\boldsymbol{A_o}\,(\boldsymbol{r}).\,\boldsymbol{e}^{-\boldsymbol{i}[\boldsymbol{\Phi_o}(\boldsymbol{r})-\boldsymbol{\Phi_r}(\boldsymbol{r})]}] \end{aligned} \qquad \textbf{(1.12)}$$

The obtained spectrum contains three bands. The phase and the amplitude information are contained in the two conjugate side bands (at $q = +q_c$ and $q = -q_c$), while no phase information is present in the centre band (at $q = 0$).

The second step is to apply a mask to one of the side bands and then take the IFT in order to obtain the complex image (Figure 1-14c).

The final step is to extract the phase image (Figure 1-14d) and the amplitude image (Figure 1-14e) from the complex image using the following equations.

$$\varphi(r) = tan^{-1}\frac{Im(r)}{Re\ (r)} \quad \textbf{(1.13)}$$

$$A(r) = \sqrt{Re^2(r) + Im^2(r)} \quad \textbf{(1.14)}$$

Where *Re* and *Im* are the real part and the imaginary part of the complex image respectively.

A reference hologram is also recorded under identical conditions, but with no specimen, so undesired phase distortions can be subtracted from the object hologram. Examples of causes of phase distortion are inhomogeneity in the charge distribution and thickness of the biprism, or spurious electric fields from the charging of microscope components [100].

Various software packages can be used to reconstruct holograms. Digital Micrograph™ is the one used in this thesis to reconstruct the phase and amplitude images from the hologram. The arctangent function (1.13), which is limited between –π and π, gives rise to contrast discontinuities in the phase image for phase changes larger than 2π. Interpretation of the phase image is generally more convenient after the phase image is unwrapped which resolves the phase discontinuities (Figure 1-14f).

1.6.3.3 Magnetic field calculations

The phase image should show the electric and magnetic fields. Therefore off-axis holography can give access to the magnetic field associated with magnetic vortices. The phase can be expressed as:

$$\phi(x) = C_E V_0(x)t(x) - \frac{e}{\hbar}\int B(x)t(x)dx \quad \textbf{(1.15)}$$

where $B(x)$ is the magnetic field in the sample perpendicular to x, V_0 is the mean inner potential of the material, $t(x)$ is the sample thickness, $\hbar$ is the reduced Planck constant, e is the electron charge and C_E a constant that depends on the microscope acceleration voltage.

If the sample is uniform in thickness and in composition, then t and V_0 are constant along x, and the derivative of ϕ in (1.15) becomes:

$$\frac{d\phi(x)}{dx} = -\frac{e}{\hbar}B(x)t \qquad \textbf{(1.16)}$$

As the values of e, t and $\hbar$ are known, and $\frac{d\phi(x)}{dx}$ corresponds to the phase ramp that can be extracted from the phase image, it is possible to calculate the magnetic field B within the specimen.

1.6.4 Vortex imaging using electron holography in the literature

Several other techniques can be used to observe vortices in superconductors such as the Bitter decoration method, scanning tunnelling microscopy and magneto-optical imaging [101-104]. Loudon and Midgley [15] draw a comparison of these techniques and a few of them are reproduced in Table 1-4.

The main advantage of Bitter decoration and magneto-optical imaging is that flux vortices can be observed over large areas. They both give access to vortex flux line patterns at different applied magnetic fields and temperatures. Scanning tunnelling microscopy has very good spatial resolution, but the field of view is limited to micron-sized regions. The main advantage of the electron microscopy techniques (Lorentz and off-axis holography) is that the vortices can be directly correlated with the sample microstructure. In addition, Lorentz microscopy can provide real-time vortex observation.

Table 1-4: Comparison of experimental techniques for vortex imaging (from [15], with permission from Elsevier).

Technique	Quantitative?	Spatial resolution	Maximum field of view	Time resolution	B-field sensitivity
Lorentz microscopy	Semi-quantitative	~200 nm	30 μm	Video rate ~1/30 s	0.04 mT
Electron holography	Yes	~10 nm	3 μm	~0.5 s	0.6 mT
Bitter decoration	No	~200 nm	No limit	Static	~0.01 mT
Scanning tunnelling microscopy	Yes	~0.1 nm	~10 μm	From few seconds to minutes	N/A
Magneto-optical imaging	Yes	~1 μm	~mm	0.1 s	0.005 mT

To check whether it would be possible to see the vortices in YBCO using Lorentz microscopy and electron holography, the magnetic field strength, B, of an individual vortex is determined by dividing the magnetic flux quantum by the vortex area:

$$B = \frac{\Phi_0}{\pi\lambda_{ab}^2} \qquad \textbf{(1.17)}$$

For a λ of 140 nm (Table 1-2) the calculated B is about 34 mT and as such is well within the range of field sensitivity of electron holography techniques (Table 1-4).

The first electron hologram of the magnetic lines of a single flux quantum in a superconductor was recorded in 1989 by Matsuda *et al.* [105] on a Pb film (Figure 1-15). Their observations were made using interference microscopy similar to the off-axis holography technique described in section 1.6.3 using a FEG-TEM operated at 150 kV. They observed magnetic field lines at the edge of the sample, in the vacuum, very localised at the surface of the specimen and spreading away from the material. They were able to show that each localised region of magnetic field lines had a value of $h/2e$ which corresponds to an individual flux quantum.

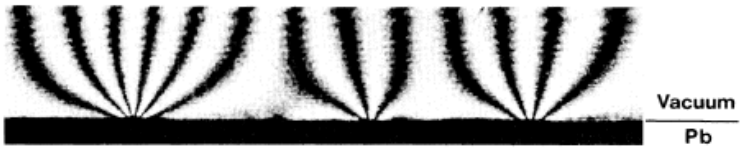

Figure 1-15: Interference micrograph of magnetic flux penetrating a superconducting Pb film (phase amplification, X2). Image and caption reproduced with permission from [105]. Copyright 1989 by American Physical Society.

Off-axis holography was used by Bonevich *et al.* [106] to observe magnetic flux lines from vortex lattices in Nb films (Figure 1-16) using a TEM operated at 300 kV. The thin black lines visible throughout the image are projected magnetic lines of forces. Bonevich *et al.* [106] circled areas where the lines are locally closer to each other. They identified those areas as vortices using the complementary techniques of Lorentz microscopy and off-axis holography.

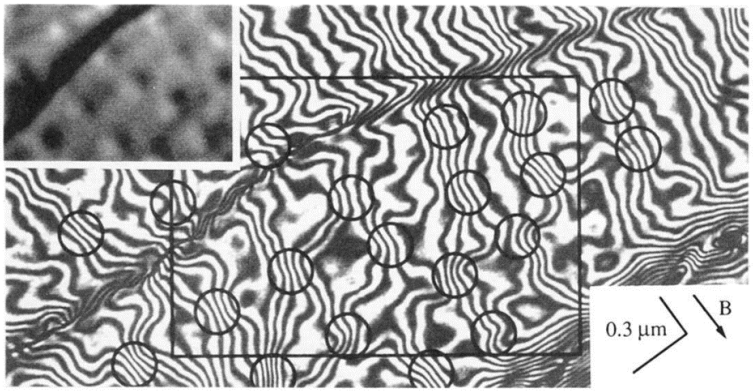

Figure 1-16: Interference micrograph of a vortex lattice (phase amplified 16X). Projected magnetic lines of force are directly observed as contour fringes. They are concentrated locally at the circled regions, becoming narrowly spaced. These regions spatially coincide with the spots observed in the Lorentz micrograph (inset), and are identified to be quantized vortices. Figure and caption reproduced with permission from [106]. Copyright 1993 by American Physical Society.

For over 20 years, Tonomura and his group studied vortex behaviour in superconductors and contributed to the development of off-axis holography and Lorentz microscopy [7]. They mainly carried out work on Pb and Nb superconductor films and on $Bi_2Sr_2CaCu_2O_{8+x}$ (BSCCO) and YBCO high temperature superconductors. They investigated the influence of the applied magnetic field magnitude and direction, the presence of columnar defects and the temperature.

To directly observe vortices in YBCO and BSCCO using Lorentz microscopy, Tonomura and his group used their 1 MV electron microscope [107, 108]. Figure 1-17 is a series of Lorentz micrographs highlighting the influence of the magnetic field tilt angle on the vortex arrangement in a YBCO single crystal. As explained in section 1.6.2, the vortices appear as circular bright and dark features when using an optimum Lorentz lens defocus. They found that increasing the magnetic field angle changed the vortex arrangement from triangular (Figure 1-17a) to linear (Figure 1-17c) on both defect free BSCCO [109] and YBCO [110], and that the vortices become elongated at higher angles (Figure 1-17d). They also discovered that vortices can be trapped by columnar defects which act as very strong pinning centres [109].

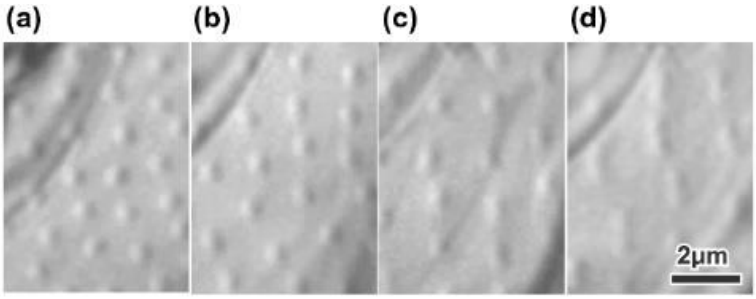

Figure 1-17: Lorentz micrograph of vortices in a YBCO crystal at tilted magnetic fields (T = 30 K; B = 0.3 mT). a) θ = 75°, b) θ = 82°, c) θ = 83°, d) θ = 84°. Figure and caption reproduced with permission from [111]. Copyright 2002 by the American Physical Society. The specimen was prepared in the *ab* plane.

More recently, direct observation of vortices using Lorentz microscopy has also been achieved on MgB_2 single crystals using a conventional FEG-TEM operated at a lower electron gun voltage, by Cottet *et al.* at 200 kV [112] and by Loudon *et al.* at 300 kV [15, 79, 113, 114]. They provide experimental details (temperature, applied magnetic field, specimen preparation) for which they successfully imaged magnetic vortices in MgB_2.

MgB_2, like YBCO, is a type II superconductor with a critical temperature of 39 K [115], considerably lower than that of YBCO (~90 K), which may make imaging vortices in the TEM simpler as a higher sample temperature can be used. MgB_2 has a hexagonal structure ($a = b \neq c$), which makes it an anisotropic uniaxial superconductor. However, MgB_2 has a considerably lower atomic weight (m_a = 46 u) compared to YBCO (m_a = 912 u). Therefore MgB_2 is electron transparent for specimen thicknesses of up to 350 nm [114], while a YBCO specimen needs to be thinner than 100 nm when under an electron beam at 300 kV.

As λ_{ab} of MgB_2 is similar to λ_{ab} of YBCO, it would be anticipated that the YBCO vortex shape and size would be similar to that of MgB_2. Therefore a number of cited documents referred to is on MgB_2 despite the fact that the material of interest in this thesis is YBCO.

1.6.5 Local applied field in holography experiments

Among the groups that have successfully observed magnetic vortices, only Loudon *et al.* describes detailed experimental conditions [15, 79, 114, 116]. They have observed vortices in MgB_2 at an applied magnetic field ranging from -5.11 mT to 7.69 mT [114] which is lower than the lower critical field, B_{c1}, of ~30 mT [117-119]. This is because the actual local magnetic field around the specimen is much larger than the one applied by the objective lenses as explained by Benkraouda and Clem [120]. They calculated that the minimum field, B_a, to apply for the first vortex to penetrate the specimen is:

$$B_a = B_{c1}\frac{L_z}{L_x + L_z} \quad \textbf{(1.18)}$$

where L_Z and L_X are the specimen thickness and length respectively.

Typical specimens prepared for electron holography are several micrometres long and no more than a few hundred nanometres thick (depending on the material). YBCO would be about 100 nm thick. This means that, depending on the specimen size, the local magnetic field around the specimen is at least 10 times greater than what the objective lenses provide.

1.7 Background summary and aims of the thesis

This chapter provided a background on superconductivity in YBCO superconductors, YBCO structure and defects in YBCO coated conductors. The vortex geometry was detailed in order to better understand vortex/defect interaction and the expectation in imaging vortices using electron holography techniques. Conventional TEM was introduced as well as the general principle of off-axis electron holography and Lorentz microscopy.

The overall aim of the thesis is to improve understanding of vortex-defect interaction in commercial YBCO coated conductors. In the first part of the thesis, the effect of the oxygenation temperature on microstructure and critical current was studied in both pure YBCO (Chapter 3) and YBCO with 50 % Dy addition (Chapter 4). The oxygenation temperature is of interest as it is a practically easy parameter to modify in industry. In the second part of the thesis, off-axis electron holography and Lorentz microscopy were performed on a YBCO coated conductor and on a YBCO crystal. The aim of those experiments is to directly image vortices in YBCO to ultimately observe a direct correlation of vortex-defect interaction, using a 300 kV TEM. The following chapter presents the experimental methodology specific to the work of this thesis.

Chapter 2 Experimental methods

The experimental work involved in this thesis included the synthesis of suitable superconducting coated conductors via the industrially-relevant method of metal-organic deposition. Both YBCO and Dy-doped YBCO samples were studied. The samples were characterised using X-ray diffraction (XRD), to determine the film's lattice parameters, the texturing and the stacking fault density, and scanning electron microscopy (SEM), to determine the surface porosity. The focus of the thesis is on the characterisation of the sample using transmission electron microscopy (TEM). TEM specimen preparation is introduced as both conventional cross-section preparation and focused-ion beam SEM (FIB-SEM) techniques were used. The TEM was used for conventional imaging to characterise the structure of the samples and for chemical analysis with energy dispersive spectroscopy (EDS). TEM images are usually analysed by interpreting the projection of the sample's structure in two dimensions. Here, the 3D distribution of the nanoparticles in the Dy-doped YBCO samples was also observed using a scanning transmission electron microscopy (STEM) based tomography technique. This thesis aims to contribute to the understanding of vortex-defects interaction in YBCO coated conductors. A way to do this would be to directly image the vortex and the defects using high-end electron holography techniques. The experimental conditions and challenges of the technique, applied to YBCO, are presented in this chapter. Vibrating sample magnetometry (VSM) was used to measure magnetic properties. Finally the critical current of the films was measured electrically.

2.1 Film synthesis

The YBCO thin films were synthesised by metal organic deposition using metal trifluoroacetates as precursors (TFA-MOD), and were epitaxially grown on RABiTs™ tapes supplied by American Superconductor (AMSC).

TFA-MOD method consists of five main steps: YBCO solution preparation; solution coating on the tape; decomposition of the metal-organic compounds by a low-temperature thermal treatment; reaction of the precursors to grow the YBCO by high-temperature thermal treatment and oxygenation of the material by annealing in oxygen.

2.1.1 Solution preparation and deposition on the substrate

The YBCO solution is prepared by dissolving all the precursors with the desired Y:Ba:Cu 1:2:3 ratio to obtain the final film composition. The chosen precursors of yttrium, barium and copper (supplied by AMSC) are dissolved in an aqueous free methanol solution. Some of the YBCO films were doped with 50 % dysprosium, which was added to the solution in the form of dysprosium acetate when appropriate. Copper was introduced in excess in the solution to ensure a good Y123 stoichiometry.

The YBCO solution was deposited on the substrate by spin coating to apply a thin and homogeneous layer. During the coating, most of the methanol is vaporised and the solution forms a gel on the substrate [22]. The deposition was done in a nitrogen atmosphere to avoid methanol vapours inhalation. The typical tape size was 1.5 cm × 1 cm. The tapes were pre-cut before solution deposition using a sharp metal guillotine to prevent from damaging the substrate surface.

2.1.2 Decomposition, reaction and oxygenation

The decomposition was done at about 400 °C in a humid oxygen atmosphere. Studies have shown that during this step the film is a mixture of polycrystalline and amorphous phases of YBCO, Y_2O_3, CuO and BaF_2 [121].

The crystalline structure of YBCO is obtained by a second heat treatment at about 750-800 °C in a controlled humid oxygen atmosphere (20 kP partial pressure). This treatment causes a reaction to form the YBCO and releases HF gas from BaF_2 [26, 31].

The crystallised film is finally post-annealed in flowing oxygen for further densification and to fully oxygenate the YBCO layer. This last oxygenation step is of particular interest in this work as it modifies the quantity and the type of defects in the film that influences the electrical properties.

2.1.3 Samples

The samples studied in this thesis are all TFA-MOD pure YBCO or 50 % Dy-doped YBCO. Both types of thin films were deposited, decomposed and reacted under the same conditions as described above. The structural defects in the samples appear during the oxygenation process. The various samples were oxygenated at either low, intermediate or high temperature in the range 300–800 °C. The precise temperatures may not be

mentioned due to commercial sensitivity. After reaching the set maximum temperature, the furnace was cooled using the slow inertia rate to ensure a maximised oxygen doping.

2.2 X-ray diffraction

X-ray diffraction was used for structural characterisation of the thin films. In this work, θ-2θ scans were used to check the phases present in the film, determine the YBCO lattice parameters and the stacking fault density. The relative misorientation of the grains was determined using the rocking curve and ϕ-scan methods [122].

2.2.1 Lattice parameters and grain misorientation

X-ray diffraction θ-2θ scans were carried out on a Philips PW1700 series diffractometer running a cobalt K_α radiation, equipped with a graphite diffracted beam monochromator, fixed incident and receiving slits and xenon filled gas proportional counters. The lattice parameters are obtained by doing a θ-2θ scan with a 2θ range typically from 5-70° with 0.02 step interval to observe the first seven (00l) YBCO reflections. The c-axis lattice parameter was calculated from the (006) peak, because of its high intensity and location at high angle, using (2-1).

$$d_{hkl} = \frac{1}{\sqrt{\left(\frac{h}{a}\right)^2 + \left(\frac{k}{b}\right)^2 + \left(\frac{l}{c}\right)^2}} \qquad (2\text{-}1)$$

The visualisation of XRD data is done by normalising the scans with the intense Ni peak. As all the YBCO thin films were synthesis on the same tape, the intense Ni peak is a good reference for scan comparison. In addition, because the Ni layer is thicker compared to the buffer layers and the YBCO thin film, the Ni peak intensity is considerably larger than the YBCO ones. It was then chosen to display XRD results using a log scale when appropriate.

The thin films texturing was studied using a Bruker D8 Advance diffractometer with cobalt K_α radiation. The study of epitaxial films requires a precise positioning of the sample to the X-ray beam. Figure 2-1 details the geometry of the sample position relative to the X-ray beam and the detector. The sample has to be placed in a way that the surface of the film is highly horizontal in order to be able to rotate it in ϕ without changing the X-ray angle ω.

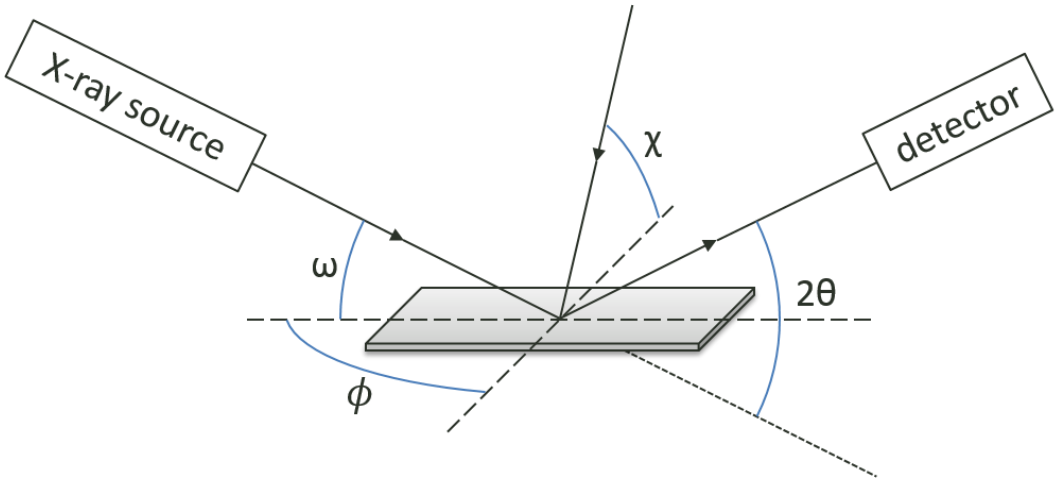

Figure 2-1: Goniometer geometry of the X-ray diffractometer around a textured sample. 2θ is the angle between the X-ray source and the detector, ω is the angle between the X-ray source and the surface of the sample, χ is the angle of the sample with respect to the horizontal and the ϕ angle correspond to the sample rotation in the horizontal plane.

The experimental parameters are chosen using the structure of the YBCO crystal lattice as follow.

The *a*-axis and *b*-axis lattice parameters were determined from the (200) and (020) peak position which, for an epitaxially oriented sample like the YBCO films, will be diffracting for a sample tilted at $\chi \approx 87\text{-}90°$. An example of θ-2θ scan of a YBCO film is shown in Figure 2-2. After precise positioning of the film, the (020) and (200) peaks are well defined and the *a*-axis and *b*-axis lattice parameters are calculated using equation (2-1).

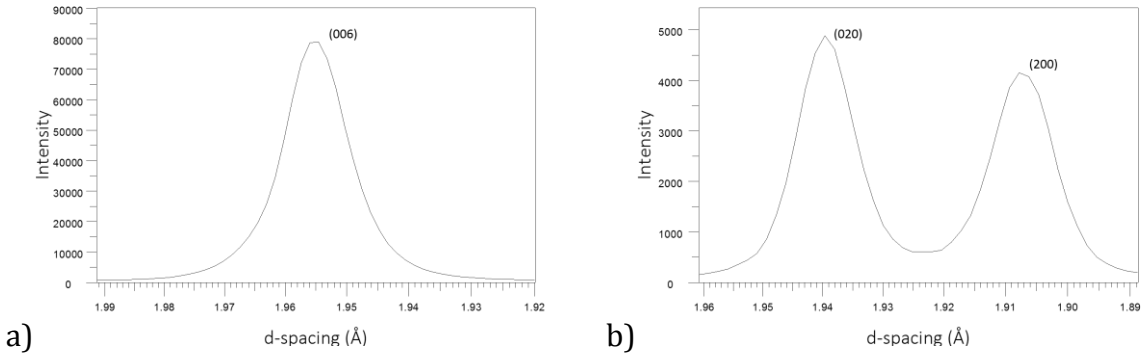

a) b)

Figure 2-2: X-ray diffraction θ-2θ scans of a YBCO film with *d*-spacing scales: a) (006) peak acquired for $\chi = 0°$, and b) the (020) and (200) peaks acquired at a tilted angle $\chi \approx 88°$.

The relative *c*-axis misorientation is measured using the rocking curve method [122]. In such scan the sample position is fixed, as well as the angle 2θ between the X-ray source and the detector, and only ω varies. Consequently, the X-ray source and the detector are

moving in a synchronised way during the scan. For a particular (*hkl*) planes family, when the X-ray incident angle ω is fixed to the value for which the planes (*hkl*) diffract, each of the (*hkl*) plane diffract. If the film is perfect with no grain misoriented, the signal would be a sharp peak. But when the angle of incidence is varied in regards to the film, with 2θ fixed, other grains slightly misoriented will diffract. The measure of the full width at half maximum (FWHM) of the rocking curve from the (006) peak was used to evaluate the misorientation in *c*-axis (an example of such scan is given in Figure 2-2).

The in-plane misorientation (or twist) in the *ab* plane was determined using a ϕ–scan on the (103) planes. In this configuration, the sample was tilted at $\chi \approx 45°$ and the X-ray source and the detector were fixed at $2\theta = 38°$.

2.2.2 Stacking fault density

The methodology used to determine the stacking fault density in the films is based on Hendricks-Teller methodology [123]. This technique has previously been used to determine stacking fault density in YBCO films [124, 125]. The intensity in a structure with stacking faults can be expressed by:

$$I = F_l^2 \Xi \frac{2p(1-p)\sin^2\left(\pi\frac{d_2-d_1}{d'}\right)}{1-2p(1-p)\sin^2\left(\pi\frac{d_2-d_1}{d'}\right)-p\cos\left(2\pi\frac{d_1}{d'}\right)-(1-p)\cos\left(2\pi\frac{d_2}{d'}\right)} \qquad (2\text{-}2)$$

where d_1 and d_2 are the *d*-spacing of Y123 and Y124 respectively, p is the fraction of Y123 layers. F_l is the structure factor and Ξ is the Lorentz polarisation factor. The details of the two latest are not given here.

Theoretical XRD plots were calculated with equation (2-2) for p between 1 and 0, that is to say for stacking faults fraction ranging from a pure Y123 phase to pure Y124 phase. The (00*l*) peaks were then fitted using a Lorentzian and the fractional change in peak position, expressed in (2-3), was extracted.

$$\frac{\left|(2\theta)_{pk}-(2\theta)_{Y123}\right|}{\left|(2\theta)_{Y124}-(2\theta)_{Y123}\right|} \qquad (2\text{-}3)$$

where $(2\theta)_{pk}$, $(2\theta)_{Y123}$ and $(2\theta)_{Y124}$ are the 2θ angles (peak position) of the calculated, the pure Y123 and the pure Y124 (00*l*) peaks respectively.

The quantity in (2-3) was then plotted as a function of p and can be expressed as a polynomial of the third order for each (00*l*) peak.

The (001), (002), (005) and (007) peaks of the experimental data were fitted using a Lorentzian function to extract the position of the peaks. The global stacking fault fraction (1−p) was then calculated as a weighted average of the fraction given by each peak.

2.3 Scanning electron microscopy

Scanning electron microscopy was used to image the films' surface porosity and to verify TEM specimen electron transparency prior to TEM imaging. An FEI Nova NanoSEM 450 field emission gun (FEG) was used at Robinson Research Institute. The surface of the sample was imaged using the backscatter detector and operating the FEG at 1 kV incident accelerating voltage with the stage beam deceleration turned on. The combination of the low accelerating voltage and the beam deceleration gives a predominantly topographic contrast as opposed to atomic number contrast.

ImageJ [126] was used to determine the porosity from SEM images of the thin film's surface. The images were recorded at a low enough magnification to visualise a significant area representative of the sample, and at high resolution to be able to separate the pores. A threshold was used to select the dark pixels corresponding to the pores and generate a binary image. The closing operation was used to fill the holes in the pores. Then the "particle analysis" plugins was used to calculate the porosity area which was finally divided by the total image surface to give the percentage of surface porosity.

TEM specimen electron transparency was ensured by imaging using SEM in scanning transmission electron microscopy (STEM) mode at 18 kV. As illustrated in Figure 2-3, the secondary electrons image of a cross section TEM specimen, do not show a contrast over the specimen surface depending on the thickness. In STEM high angle annular dark field (HAADF) and dark field (DF) modes the thinner areas of the specimen are visible and appear darker or brighter respectively. Those observations are therefore useful prior to TEM work in order to make sure the specimen is electron transparent.

a) 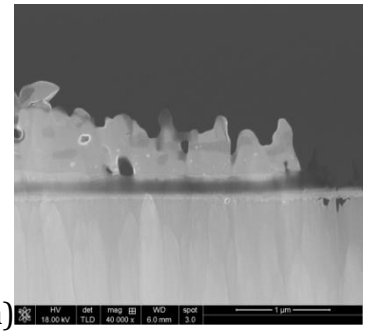 b) 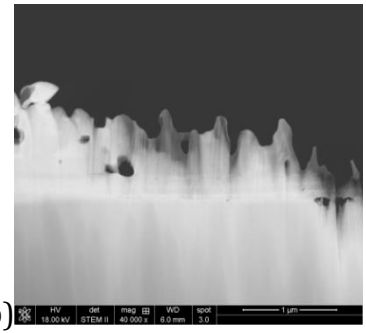 c) 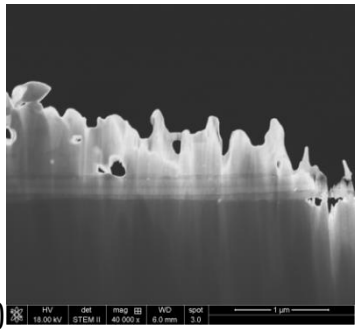

Figure 2-3: SEM micrographs of a cross-section YBCO thin film specimen: a) secondary electron, b) STEM-HAADF mode, c) STEM-DF mode. Scale bar 1 µm.

2.4 TEM specimen preparation

2.4.1 Conventional cross-section specimen preparation

Conventional TEM specimen preparation is a long process which requires several steps of manual polishing and ion milling to attain electron transparency as illustrated in Figure 2-4.

The YBCO film is cut in 5 mm x 10 mm slice and mounted between two silica slices as a sandwich to support the thin sample and protect the YBCO layer during mechanical polishing (Figure 2-4a). Epoxy (Allied 2-Part Adhesive EpoxyBond 110™) is used to bond the three slices together and is cured at 100 °C for 2 hours. The epoxy bond has to be as thin as possible but strong enough to bind the pieces. The sandwich is then cut normal to the interface (Figure 2-4b) in thin slices before being polished on both sides down to 30 µm thickness using a tripod polisher (Figure 2-4c and d). Five different sizes of diamond lapping film (30, 15, 9, 6 and 3 µm) are used to mechanically polish the sample on a flat glass surface. The specimen is then attached to a TEM grid using the same epoxy bond as previously (Figure 2-4e). Finally, the specimen is milled to electron transparency using a Gatan precision ion polishing system (PIPS), operated at 5 kV, with the guns angle at 7° for 2-5 hours until the YBCO is partially milled and then 3-4 kV with the guns at a 4° angle for a finer and softer final milling.

Considering the epitaxial growth of the YBCO on the substrate and the direction the specimen is cut, the cross-section TEM specimens observed present the *c*-axis in plane, as indicated on Figure 2-4.

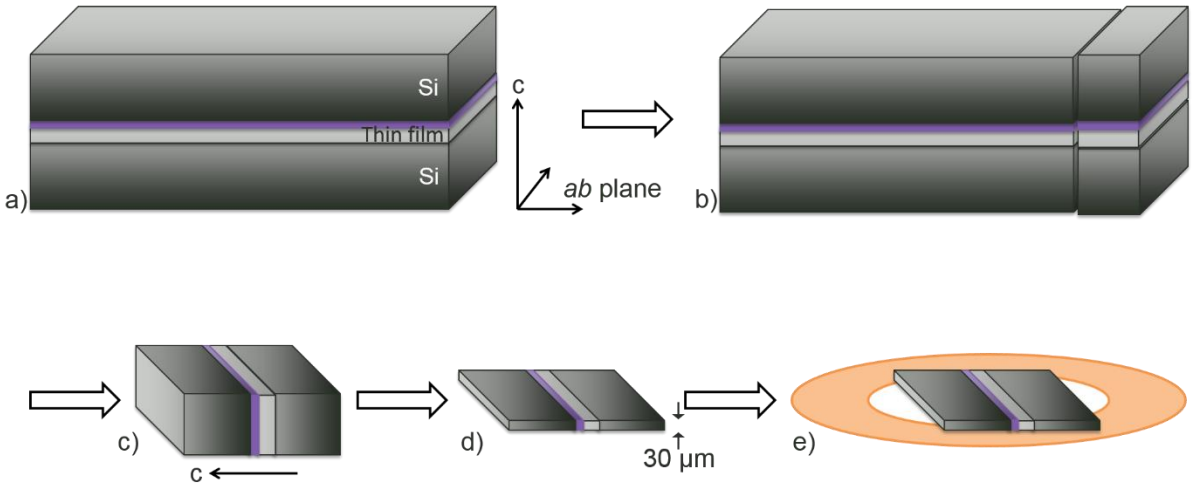

Figure 2-4: Detailed diagram of conventional cross-section specimen preparation. a) The film is glued between two silica layers using epoxy, b) the sandwich is cut in a thin layer (about 2 mm) then polished down to about 30 µm using diamond films and e) the thin specimen is attached to a TEM grid using epoxy.

2.4.2 Focused ion beam principle

A FIB-SEM is based on the same principle as a SEM, but is equipped (in addition to the electron gun) with an ion gun and is used to mill shapes or, in the case of this work, to thin a TEM specimen. The ion source is generally Ga because its low melting point (30 °C) and low volatility (at the melting point) make it a long-lasting source (~400 µA-hours/mg) and the low surface free energy gives a very sharp tip.

Solid metal Ga is heated by a large electric field and is ionised at the tip of a tungsten needle. The ions extracted from the source are then accelerated between 1-30 kV to form the ion beam. The beam is then focused onto the sample using a series of magnetic lenses, apertures and electrostatic deflectors. The created current can be up to 20 nA and is destructive.

It is possible to image with both the electron beam and the ion beam, although imaging with the ion beam should be kept to a minimum because the heavy Ga ion will damage the sample. To protect the TEM lamella from extensive Ga implantation, a protective layer of Pt is deposited using a precursor gas mix of Pt and C. The sample is scanned by the electron or ion beam while the Pt precursor gas is introduced near the sample and the metal from the gas is deposited at the sample surface by chemical vapour deposition.

The instruments used were a FEI Helios NanoLab DualBeam FIB-SEM at DTU Cen and a FEI Quanta 3D FEGSEM at MCEM Monash University. They are both equipped, in addition

to the electron and Ga ion sources, with a suite of imaging detectors, Pt gas injection tube and a micromanipulator.

2.4.3 Specimen preparation using FIB-SEM

The following description, illustrated by the SEM micrographs in Figure 2-5, details the main steps involved in TEM specimen preparation using a FIB-SEM for YBCO films. Here, the term "specimen" refers to the lamella extracted from the film for TEM observation and "sample" refers to the original thin film (i.e. prior to FIB preparation). The specimen preparation for the crystal is very similar so it will not be described.

The thin film is placed in the FIB-SEM chamber under vacuum. Two layers of Pt (about 3 μm in total) are deposited on the top edge of the film area to be milled (Figure 2-5a). This protects the sample from damage and milling during the procedure. The first Pt layer is deposited using a low acceleration voltage electron beam with a low Pt to C ratio, and provides protection from the ion beam. The second Pt layer is made using a low current ion beam with a high Pt to C ratio, and provides a better protective layer. Trenches are then cut into the sample on two sides of the Pt deposition to shape the specimen (Figure 2-5b-c, cuts 1-3). The biggest trench (cut 1), away from the specimen is made at high current (9 or 20 nA). The current is reduced as the milling gets closer to the specimen to reduce the risk of Ga implantation. A micromanipulator is attached with Pt to the specimen (Figure 2-5c) and the last edge of the sample is milled to completely detach the specimen from the sample (cut 4). The specimen is then attached to a TEM grid at 45° for electron holography experiments as suggested in previous work [9, 15, 96, 105, 106, 114, 116] (Figure 2-5d and e), or 0° for conventional TEM imaging.

For electron holography experiments, the heat transfer between the specimen and the TEM grid must be optimised. A notch is shaped on the side of the grid to fit the specimen. The gaps between the specimen and the grid are filled with Pt to ensure good electrical contact. A final layer of Pt is deposited over all the contacts between the grid and the specimen. Once the specimen is well attached to the grid, the micromanipulator is cut from the specimen. The specimen is then thinned on both surfaces to attain electron transparency (Figure 2-5e and f). A final cleaning of the specimen surfaces is done at very low voltage (2 kV) and current (11 pA) to remove possible amorphous or electrically "dead" layers created by the milling and imaging with the electron beam.

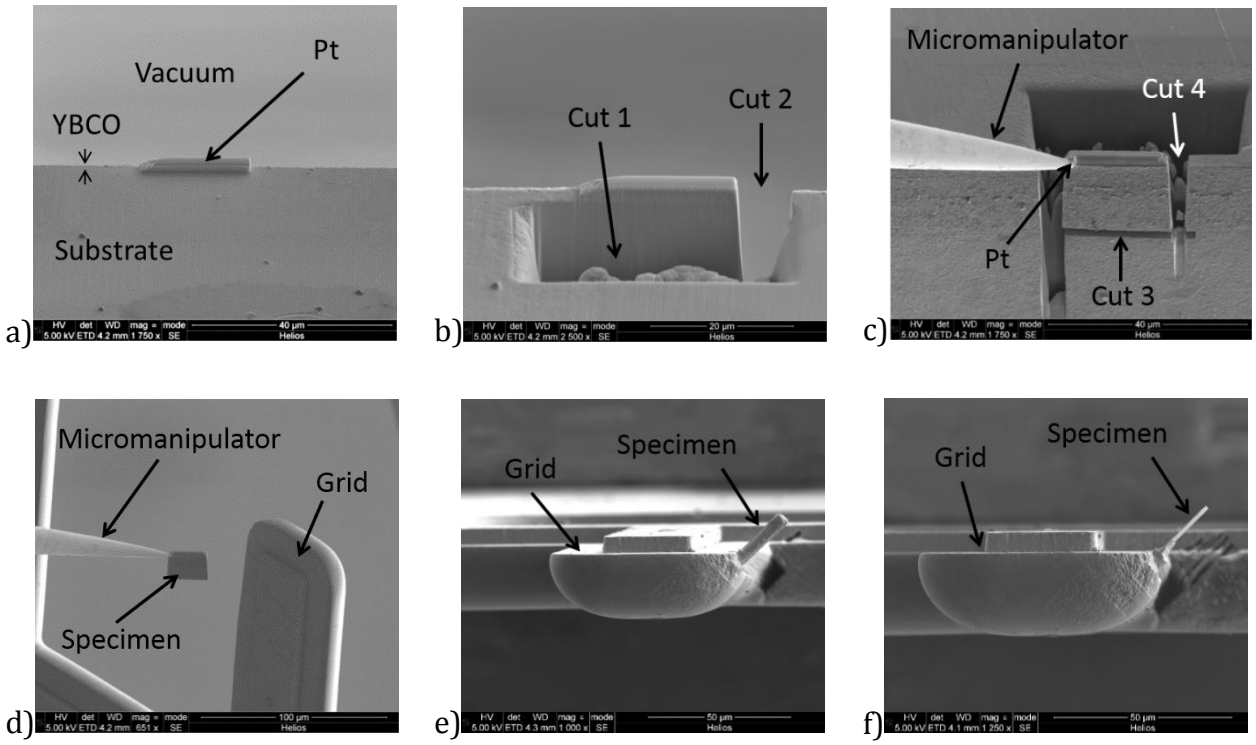

Figure 2-5: Steps involved in TEM specimen preparation using FIB-SEM: a) Pt deposition, b) milling on each side of the protective Pt, c) final milling and lift out, d) approach of the specimen to the TEM grid, e) specimen mounted on the grid before thinning and f) specimen thinned to electron transparency.

During the FIB specimen preparation process, imaging on the region of interest using the ion beam is avoided as much as possible, especially at high currents. Furthermore, the milling current is reduced as the thickness of the specimen gets closer to electron transparency.

Electron holography requires a specimen with a surface as flat as possible with no surface roughness, and a uniform thickness. The ion beam current has a Gaussian distribution [127], as such, the specimen needs to be slightly tilted by 1 to 2° with respect to the ion beam in order to obtain flat and parallel surfaces. All the holography specimens were prepared in the *ab* plane with *c*-axis out-of-plane.

For high resolution imaging, using conventional specimen preparation method is preferable as the Ar milling is gentler for the specimen than the Ga ion and also provides a thinner specimen. However the FIB-SEM was used to remove the entire Ni substrate for HRSTEM imaging. The Ni was milled away after the lift out, before the milling to electron transparency. This was done because the alignment in STEM mode was compromised by the strong magnetism of the Ni layer of the tape. The presence of the Ni was causing a lot

of astigmatism making the observation and the image acquisition challenging. In addition, FIB-SEM was indispensable to prepare specimen for electron holography experiment to control the area the specimen was selected from and to place the specimen at the specific orientation of 45°.

2.5 Transmission electron microscopy

Most of the high resolution images presented in this thesis were recorded using JEOL instruments located at Victoria University of Wellington (VUW). A JEOL 2010 TEM equipped with a LaB_6 filament operated at 200 kV and a Gatan charge-coupled device (CCD) camera was used for imaging and diffraction. A JEOL JEM-2100F TEM equipped with a FEG operated at 200 kV and equipped with a JEOL SDD EDS detector, a dark field and bright field detectors for STEM imaging and a high dynamic range CCD camera for diffraction acquisition was used. A JEOL JEM-2100F FEGTEM, located at the Monash Centre for Electron Microscopy (MCEM) was also used, operated at 200 kV and equipped with a Gatan Ultrascan CCD camera.

The high resolution scanning transmission electron microscope (HRSTEM) images were recorded using a FEI Titan ATEM equipped with a FEG, a monochromator and spherical aberration corrector (Cs corrector) at the Centre for Electron Nanoscopy at the Technical University of Denmark (DTU Cen). The instrument is equipped with an Oxford Instrument EDS detector. The microscope was operated at 300 kV. The probe correction allows imaging with high spatial resolution giving possibility of high resolution imaging and chemical mapping with TEM and STEM. The TEM also features a biprism wire for electron holography and a Lorentz lens for Lorentz microscopy.

2.5.1 HRSTEM using a spherical aberration corrected TEM

For HRSTEM imaging, the microscope was aligned using a specimen of gold nanoparticles on a carbon grid as a reference sample. A HRSTEM micrograph of the reference sample is presented in Figure 2-6. The resolution can be checked on the Fourier transform of an area were lattice fringes can be seen (Inset Figure 2-6) with the distance between the transmitted been and the furthest reflection. For HRSTEM imaging, the resolution was around 1.2 Å.

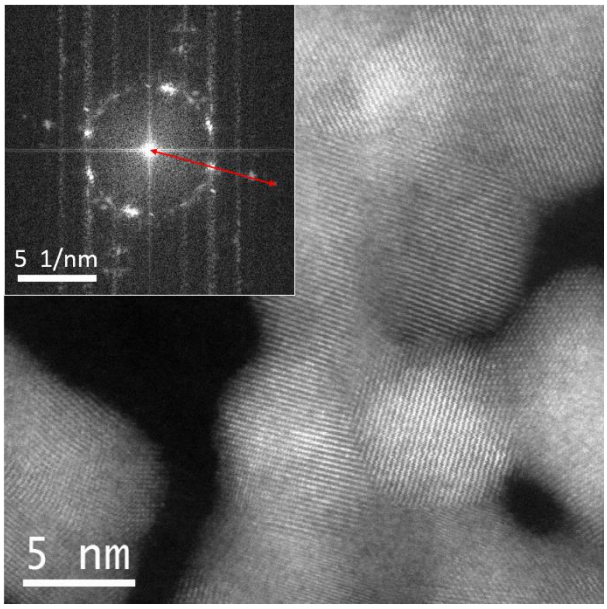

Figure 2-6: HRSTEM micrograph of gold nanoparticles dispersed on a carbon grid. Inset is a Fourier transform of the region exhibiting lattice fringes.

The microscope calibration was checked using the lattice fringes visible from the CeO_2 buffer layer (Figure 2-7). CeO_2 has a cubic structure with lattice parameter a = 0.541 nm [128, 129]. The Fourier transform inset Figure 2-7 shows that the CeO_2 is down [011] zone axis where the (111) and (200) reflections are visible giving the d-spacing d_{111} = 0.322 ± 0.008 nm and d_{200} = 0.277 ± 0.008 nm. One pixel corresponds to 0.2123 nm^{-1} giving an error of about 3 %.

The JCPDS data from EVA (No 34-0394) gives d_{111} = 0.3123 nm and d_{200} = 0.2705 nm. This shows that the spacing visible on CeO_2 is 3.1 % higher from the theoretical values of CeO_2 structure.

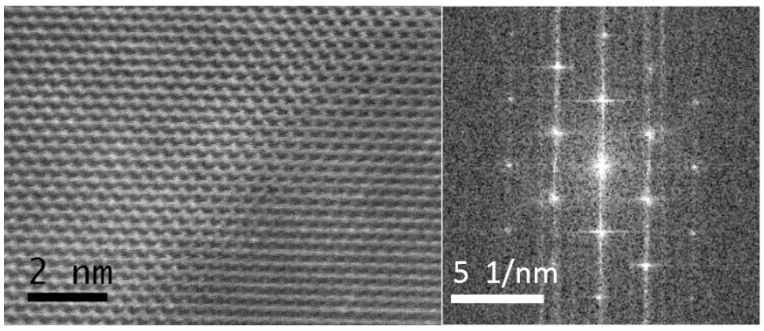

Figure 2-7: HRSTEM micrograph of the CeO_2 layer of the films (left) and its corresponding Fourier transform.

The Java electron microscopy simulation (JEMS) is a Java based simulation package created by Dr. Stadelmann [43]. The package offers multiple options of simulation mainly

related to electron interaction with atoms. The main tool used in this thesis was HRSTEM simulation. The studied structures were pure Y123 and pure Dy123 to compare with the Dy-doped YBCO films. The unit cell of the structure being relatively close, the a, b and c lattice parameters were not dramatically modified and the output parameter of interest from the simulation was the relative intensity of each atomic column.

The Y123 unit cell structure was provided in the JEMS package database [43]. From this base, the lattice parameters could be adjusted for Dy123 from reference [130].

2.5.2 Chemical analysis

Chemical analysis of the thin films was done using EDS on several TEM. The FEI Titan ATEM permitted a high magnification and higher resolution mapping because of the aberration corrected probe. The conditions with this microscope for STEM-EDS were: condenser apertures C1 2000 µm, C2 70 µm and C3 2000 µm, spot size 7 and camera length 16 cm. Other EDS analysis was performed using the JEM-2100F TEM at VUW. The typical conditions for STEM-EDS on the 2100F were using the 100 µm condenser aperture, spot 1.5 and camera length 12 cm. The microscopes were aligned using a gold nanoparticle sample on a carbon grid before inserting the YBCO samples to facilitate the alignment in the appropriate conditions.

2.5.3 Tomography

The tomography experiment was performed with a FEI Titan ATEM operated at 300 kV in STEM mode on a Dy-doped YBCO film to observe particle distribution. The specimen was prepared using a FIB-SEM in a cross-section view.

As explained in Chapter 1, the tomography experiment is a four-step process: acquisition of a tilt series, alignment of the tilt series along the tilt axis, reconstruction of the 2D images in a 3D volume and finally the segmentation to emphasis the features in a 3D model.

The specimen was loaded on a single tilt Fischione tomography holder that allows for large tilt angle $\pm$ 76°. The detector parameters were chosen carefully for the acquisition of the tilt series. YBCO has a large atomic number and therefore dominates the contrast in dark field images, making other particles only visible by applying a large contrast. The tilt series was consequently acquired with the bright field detector, using a short camera length of 77 cm, giving a good compromise to visualise the particles without over-

enhancing the diffraction contrast from other structural defects such as stacking faults or grain boundaries. STEM images were acquired with 2° step interval.

The tilt series images alignment and the reconstruction (the creation of a 3D volume in frames within xy, xz and yz) from the stack of tilt STEM images was performed using the FEI software Inspect 3D™.

The segmentation (visualisation in 3D of the feature of interest, here the nanoparticles) was made using FEI software Avizo™ and can be done using a threshold when the features of interest have a uniform and distinct contrast compared to the rest of the sample. However, the presence of a high density of defects (twin boundaries, dislocations, stacking faults, nanoparticles) in the YBCO thin film, minimised by adjusting the microscope alignment and the detector parameters, created a diffraction contrast that makes the segmentation challenging using an automated threshold. The segmentation was therefore done by identifying the particles frame by frame.

The reconstruction and the segmentation were done over a 500 nm wide area from the buffer layers, and about 700 nm long towards the surface of the film.

With tomography, it is possible to see the distribution of the particles within the film volume.

2.6 Electron holography in a transmission electron microscope

The aim of the electron holography experiments is to understand the vortex pinning behaviour on structural defects in YBCO coated conductors. The work was performed using a FEI Titan 80-300 ATEM operated at 300 kV at the Center for electron nanoscopy at the Technical University of Denmark (DTU Cen). The main challenges to overcome with electron holography experiments are the following:

- Use of a TEM operated at 300 kV to observe vortices in YBCO, which has not been achieved to date.
- The presence in practical superconducting wires of a large density of defects in the matrix, nanoparticles and chemical phases. This highly nanostructured material, as opposed to perfect crystal structure, creates diffraction contrast that obscures vortex contrast. Therefore the observed contrast might not be directly associated with magnetic field.

Electron holography was therefore attempted on both YBCO crystals and YBCO coated conductors. To overcome the microstructural challenge and be able to find the appropriate setting for the microscope, a YBCO crystal was used. To ensure that the microscope conditions were appropriately set to observe vortices, Lorentz microscopy was first performed then off-axis holography was attempted.

The YBCO samples were first characterised using XRD and VSM techniques to determine the samples purity, the critical temperature and the lower critical field.

2.6.1 YBCO crystal oxygenation

The provided YBCO crystals were annealed in an oxygen atmosphere at 450 °C for 72 hours following the annealing cycle shown in Figure 2-8.

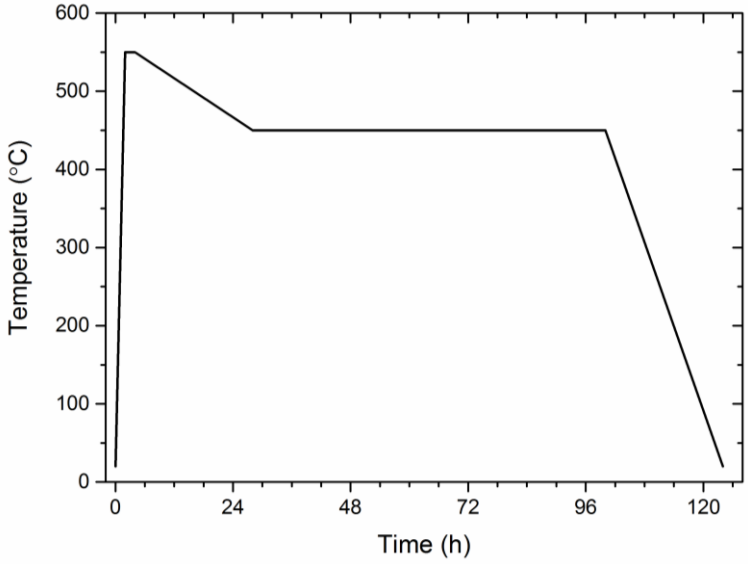

Figure 2-8: Nominal oxygenation cycle of the YBCO crystal, the temperature was raised to 550 °C in 2 h, hold for 4 h, then cooled to 450 °C in 24 h and held for 72 h, and finally cooled to room temperature in 24 h allowing a slow cool-down.

The oxygen flow rate was set at 200 cc/min. This cycle was chosen to fully oxygenate the crystal to achieve a homogeneous doping state and to reach a similar critical temperature to that of the films.

2.6.2 Experimental set-up

The TEM was set at 300 kV 12 hours in advance to ensure electron beam stability. The microscope was aligned in conventional TEM mode prior to the experiment.

Sample cooling is essential to cool the superconductor below T_c and requires at least liquid nitrogen temperatures (77 K). Although Tonomura and his group do not describe

their cooling procedure in detail, the use of liquid nitrogen for holography experiments has not been seen in the literature. The use of liquid helium is preferred to cool the sample well below T_c and minimise vortex movement when there are no pinning sites.

The specimen was mounted in the helium holder (Figure 2-9b), and then inserted into the TEM (Figure 2-9a). Since the He holder is very heavy compared to a standard TEM holder (Figure 2-9c), an extra stage equipped with two springs is added outside the TEM column to support the additional weight. The springs are screwed on each side of the holder and adjusted to an alpha and beta tilt of 0° and stage position of z = 0. Extreme care is taken to correctly position the He holder. An incorrectly positioned holder could compromise the vacuum, which could lead to beam instabilities or instrument damage.

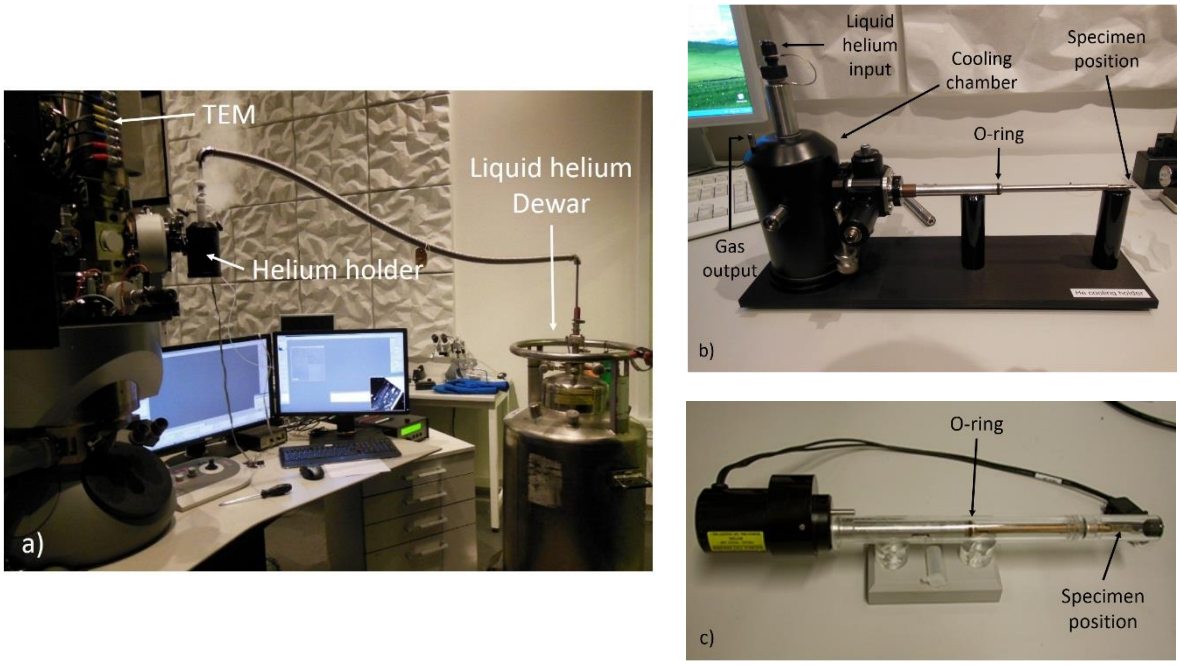

Figure 2-9: a) Experimental setup to cool the specimen to cryogenic temperature. The He holder is first inserted in the TEM, then the liquid helium is supplied to the He holder from the Dewar, b) Gatan He holder and c) standard FEI double tilt holder.

Once the He holder is correctly mounted into the TEM, liquid He was supplied to the He holder using a transfer tube. During the experiment, it is critical to maintain a stable temperature. Figure 2-10 shows the specimen temperature as a function of time during sample cooling. The first cooling (cooling 1) was performed with a relatively poor He holder chamber vacuum, which resulted in a slow temperature decrease and a waste of liquid He by evaporation. The second cooling (cooling 2) was done after improving the

He holder chamber vacuum. The liquid He was therefore supplied with less waste by evaporation and the cooling was significantly faster. When the liquid He cooling chamber is full, a plume appears at the tip of the gas output. The liquid He supply is then detached from the He holder to avoid vibrations during the hologram acquisition. An optimised He filling allows for about 1 h of cryogenic temperature.

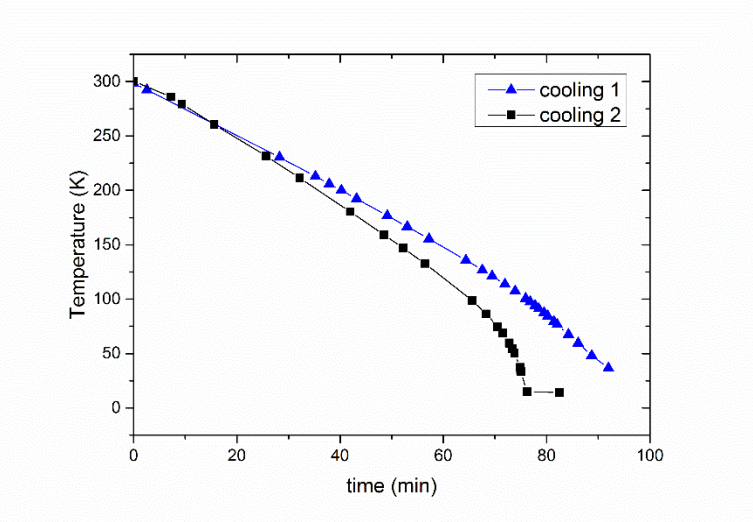

Figure 2-10: Temperature of the specimen as a function of time while supplying liquid He in the holder.

For both YBCO thin film and crystal, off-axis holography and Lorentz microscopy holograms were recorded at stable low temperatures (10 K and 20 K).

The off-axis holography experiment with observation in the vacuum was carried out while the temperature was ramping up, and a series of holograms were recorded at different temperatures, from 20 K to 95 K just above T_c, after which no vortices are expected to be seen since the specimen is no longer in the superconducting state.

2.6.3 Specimen and observation configuration for off-axis holography

2.6.3.1 Region of observation

Phase variations will only be observed where the interference fringes created by the biprism are located. By placing the specimen in the field of view, the magnetic field within the material can be studied (Figure 2-11a and c). It is also possible to observe the magnetic field next to the specimen by locating the specimen slightly off-centre from the electron beam and the hologram formation (Figure 2-11b and d). A TEM is always

operated with the chamber under vacuum for electron beam stability and coherency. In this chapter, when the sample is placed slightly off-centre from the electron beam the observation area is then referred to as being "in the vacuum" next to the specimen (Figure 2-11b). This second method was tested to observe the magnetic field leaking from the material.

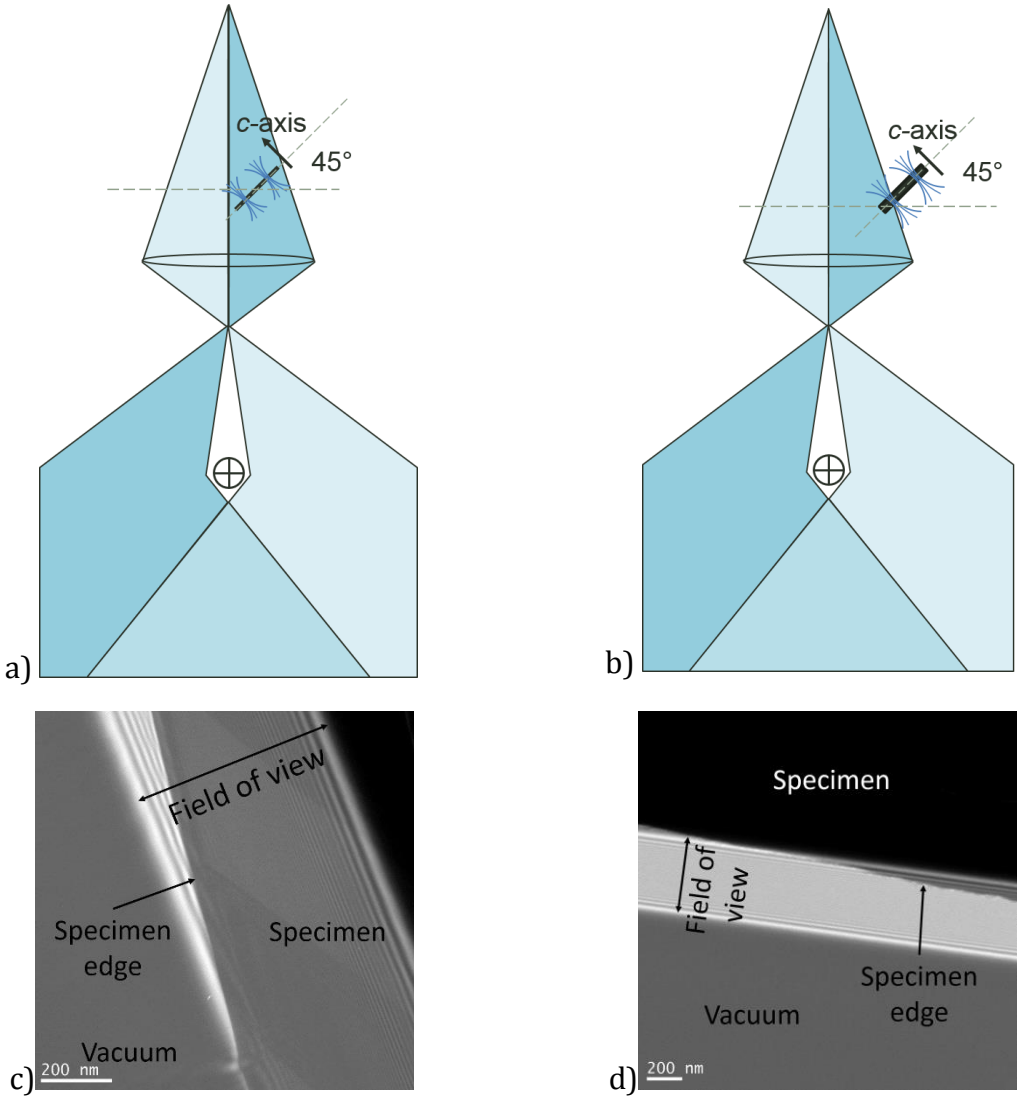

Figure 2-11: Schematic of the specimen position with regard to the electron beam in off-axis holography a) with the specimen in the field of view and b) with the edge of the specimen in the field of view for imaging the magnetic field leaking from the specimen. c) and d) are the corresponding recorded holograms for a) and b) configurations respectively.

In both cases the specimen was mounted at 45° with respect to the electron beam. As mentioned in section 1.6, the magnetic field was applied to the sample using the objective lens. As discussed by Loudon and Midgley [15], the axis of the vortices will run through

the thinnest section of the sample. If an un-tilted sample was to be observed this would provide no magnetic field perpendicular to the incident electron beam and as such would provide little beam deflection for imaging the magnetic vortices. As such, the specimen was mounted in an intermediate position at 45°, between the electron beam and the applied field angle for good beam deflection [79].

2.6.3.2 Specimen thickness

Vortex observation conditions are improved by increasing the specimen thickness in order to maximise the phase shift of the electrons [15], but it still must be sufficiently thin to maintain electron transparency for Lorentz microscopy and off-axis holography. Both phase shift and inelastic scattering increase with the specimen thickness and give a better signal to noise ratio. To observe the magnetic field at the edge of the specimen in the vacuum area, this does not require the specimen to be electron transparent and a purposely-thick specimen was prepared. This specimen was approximately 800 nm thick and the Ni and the buffer layers were removed during ion milling.

2.6.4 Reference hologram

During the previous experiment, the specimen was under a constant stable applied magnetic field and the holograms were recorded at different temperatures. The following sections highlights the importance of recording a reference hologram for each object hologram recorded. For each hologram recorded at a temperature, a reference hologram was recorded too. The intensity profiles taken at different temperatures on reference holograms (that is to say with no specimen in the field of view) are shown in Figure 2-12.

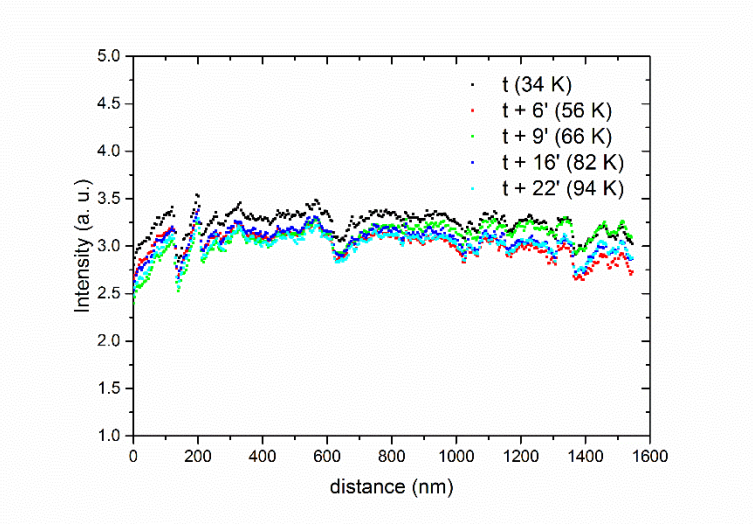

Figure 2-12: Intensity of reference holograms with no sample in the field of view at different instant t (and different temperatures).

The variation of intensity is similar at each different temperature showing an overall stability in the TEM chamber. In theory, the reference hologram does not depend on the specimen temperature. However, this figure shows that the intensity changes over time and that whenever an object hologram is recorded at an instant, a reference hologram has to be recorded too for accuracy of the reconstruction and phase comparison.

2.7 Magnetic properties and critical temperature of YBCO crystal

The critical temperature and the lower critical field were measured using a Quantum Design physical property measurement system (PPMS) operated in vibrating sample magnetometer (VSM) mode. The instrument can apply a static and uniform magnetic field up to 9 T in a temperature range of 2-400 K. The measurements consist of physically vibrating the sample in a uniform applied magnetic field to detect the induced voltage which is proportional to the sample's magnetic moment. The sample was cooled to the chosen temperature under zero applied magnetic field.

The YBCO crystal was positioned in order to apply the field along the *c* direction and perpendicular to *ab* plane. The critical temperature was determined by measuring the sample's magnetic moment between 10 and 200 K under 1 mT applied magnetic field. The lower critical field was determined from magnetisation curves at 10 and 20 K, between 0-500 mT.

2.8 YBCO coated conductor electrical measurements

The critical current provides information about the magnetic flux pinning of the thin films as explained in section 1.2.2.

The interest in measuring the critical current as a function of the applied magnetic field angle relative to the sample is to detect film orientations that exhibit strong vortex pinning. This aims to correlate the isotropic and anisotropic structural defects with the measured critical current. A schematic of the applied magnetic field ***B*** and the current ***I*** direction is presented in Figure 2-13. At 0° the magnetic field is perpendicular to the plane of the sample (along the *c* direction), while at 90° it is parallel to the *ab* plane. The axis of rotation is the same as the current direction to keep ***B*** normal to ***I*** to maintain a constant Lorentz force acting on the vortices for all field angles.

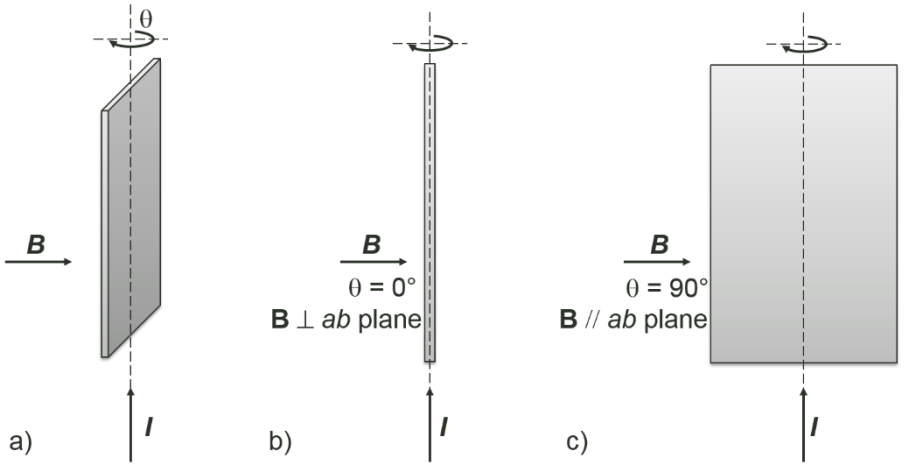

Figure 2-13: Schematic of the applied magnetic field and current angles relative to the films for critical current measurements: a) arbitrary angle, b) *B* perpendicular to the *ab* plane and c) *B* parallel to the *ab* plane.

The electrical measurements were performed with instruments built in the Robinson Research Institute, the first one has a 3 T magnet and can reach 77 K using liquid nitrogen, the second one has a 8 T magnet and is equipped with a cryocooler that allows measurements as low as 20 K, with currents up to 850 A [131].

The thin films were coated with a silver layer to provide good electrical contact for critical current measurements. The coating was made prior to the oxygenation cycle as the annealing both performed full oxygenation of the YBCO and also a good contact between the silver and the YBCO. Silver has the advantage that it does not react with the YBCO and it lets the oxygen go through to fully oxygenate the YBCO during the oxygenation cycle.

A bridge was patterned into the sample to provide a defined current pathway and voltage tap spacing, and to reduce the required current for the measurements and avoid the low quality regions at the edges of the thin film created by spin coating deposition [132]. The 5 × 0.5 mm bridge was patterned by photolithography and wet etching, using an aqueous solution of ammonia and hydrogen peroxide to etch the silver layer, and an EDTA solution to etch the YBCO.

The sample was soldered to the measurement holder using a silver foil to ensure good electrical contact between the film and the current leads. Two wires were soldered to the film at 5 mm from each other using indium-bismuth low temperature solder to measure the voltage.

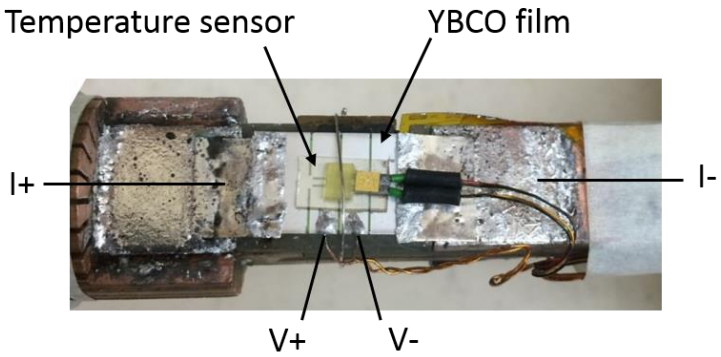

Figure 2-14: YBCO film mounted for electrical measurements. Silver foils are soldered to the sample to create good contacts and prevent from heat when the current is applied. Two wires are attached to measure the voltage, separated by a distance corresponding to the length of the bridge. A Safire plate is placed on the film's surface to measure the sample's temperature.

For each applied magnetic field angle, the voltage, V, versus the current, I, is measured as shown by Figure 2-15.

The curves were fitted using a power function as shown by the following equation:

$$V = V_0 \left(\frac{I}{I_0}\right)^n \qquad \textbf{(2-4)}$$

where V_0 , I_0 and n are fitted parameters.

As long as there is no resistance, the voltage as a function of the current is null. The critical current is then determined for a non-null conventional criterion of 1 μV/cm. The critical current over the bridge width is then calculated, giving I_c/w (A/cm), for applied magnetic field angles ranging between 0-180° (Figure 2-16). Throughout the thesis, only I_c/w data is presented, and the critical current, I_c in the text always refers to I_c/w. The I_c

measurements were made at 77 K and 30 K for applied magnetic field of 1 T and for temperature between 20-90 K under no applied magnetic field. Under no applied magnetic field, the critical current is referred to as the self-field critical current I_c.

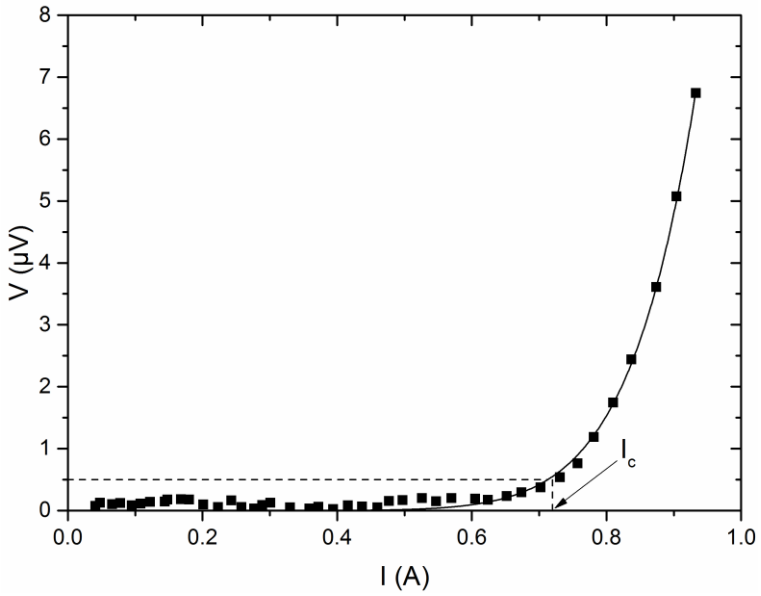

Figure 2-15: Example of voltage versus current measured on a YBCO film, with *B* perpendicular to the *ab* plane (θ = 0°). The typical bridge length is 5 mm, the voltage criterion for which $I = I_c$ is therefore 0.5 μV. The line corresponds to the power function fit.

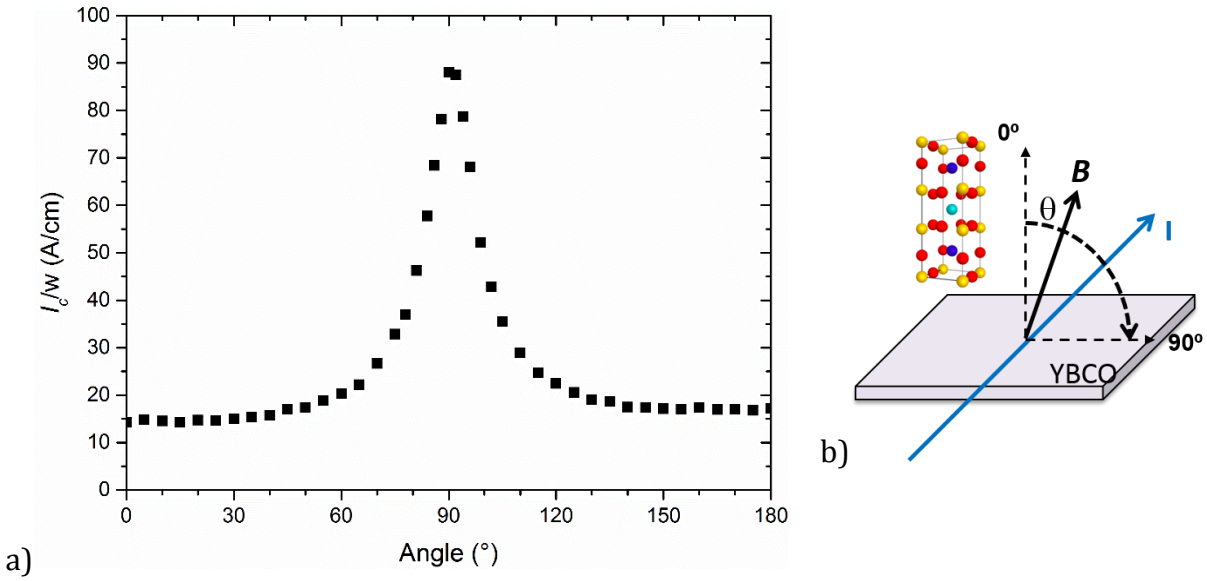

Figure 2-16: a) Example of critical current as a function of the applied magnetic field angle measured on a YBCO film. b) Schematic of the applied magnetic field angle θ relative to the electrical current and the YBCO film.

2.9 Summary of experimental methodology

This chapter described the experimental methods used to investigate vortex/defect interaction in YBCO superconductors. It first described the synthesis procedure and the samples studied. To start with, pure YBCO and Dy-doped YBCO coated conductors will be studied, using XRD, TEM and electrical measurements, and the results are presented in Chapter 3 and Chapter 4 respectively. A YBCO crystal and YBCO coated conductor will be studied using off-axis electron holography and Lorentz microscopy. These results are presented in Chapter 5.

Chapter 3 Pure YBCO film microstructure and electrical properties

The aim of this chapter is to study the effect of low (LT), intermediate (IT) and high (HT) oxygenation temperature on the microstructure and the electrical properties of pure YBCO coated conductors synthesised as described in Chapter 2. As explained in Chapter 1 (Section 1.2.1), the influence of the successive synthesis steps of YBCO coated conductors has been widely studied, but little literature was found on the effect of the oxygenation temperature on the YBCO microstructure and electrical properties.

The growth of the film is first presented with the X-ray diffraction (XRD) results, followed by the surface porosity using scanning electron microscopy (SEM), and the chemical analysis with energy dispersive spectroscopy (EDS). The structure of the samples is then characterised using high resolution transmission electron microscopy (HRTEM). This chapter ends with the critical current, I_c, results. All the presented results also aim to provide a baseline for comparison with the effect of Dy addition in Chapter 4.

3.1 X-ray diffraction

XRD measurements were performed to determine the phases present, the film texturing, the film lattice parameters, the out-of-plane misorientation and the in-plane misorientation.

Figure 3-1 shows a θ-2θ XRD patterns of the LT, IT and HT YBCO samples. The log of the intensity is plotted versus the diffraction angle 2θ and the maximum intensity is normalised to the Ni peak. In Figure 3-1, the following peaks are labelled: (00*l*) YBCO, (200) Ni substrate, (200) CeO_2, (400) Y_2O_3 and (200) yttrium stabilised zirconia (YSZ) of the buffer layers, NiO (∗) and $BaCeO_3$ (◊).The YBCO *c*-axis epitaxial growth on the substrate is confirmed by only the (00*l*) YBCO peaks being observed. Similarly, the strong texturing of the buffer layers on the Ni substrate is confirmed by only the CeO_2 (200), YSZ (200) and Y_2O_3 (400) being present. Finally, reaction impurities of NiO, Ba-Cu-O and $BaCeO_3$ are observed.

The *c*-axis lattice parameter of the YBCO is determined from the (006) peak position and is approximately 1.173 nm, 1.172 nm and 1.172 nm for the LT, IT and HT YBCO samples respectively (Table 3-1), showing that the oxygenation temperature does not strongly

affect the *c*-axis lattice parameter. This also confirms the similar oxygen doping of the films despite the different oxygenation temperatures [133].

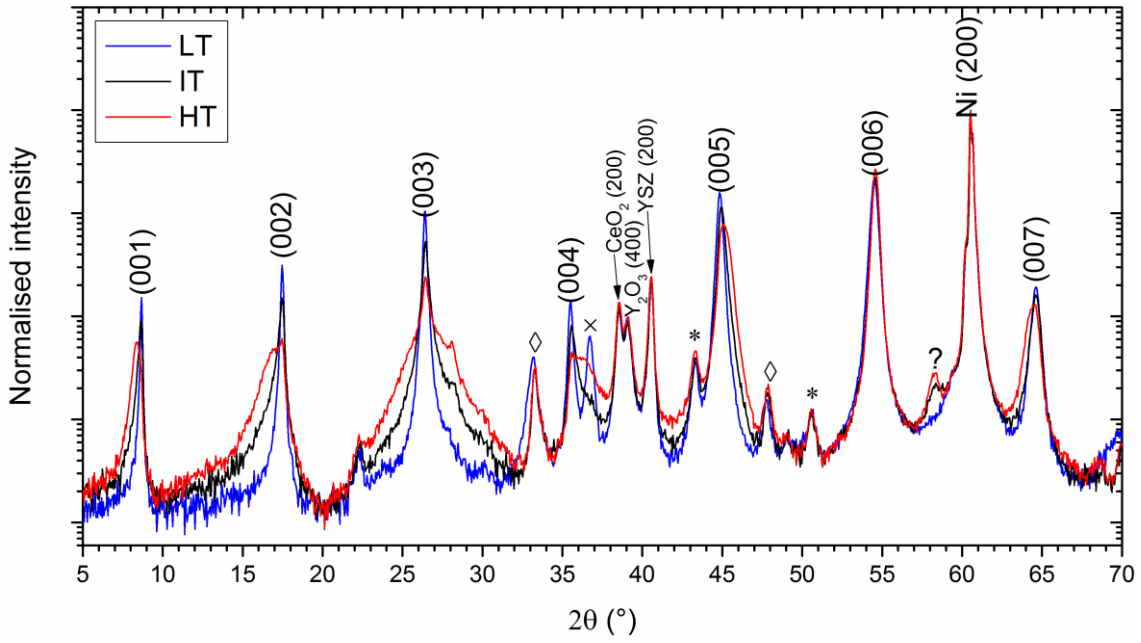

Figure 3-1: X-ray diffraction θ-2θ scans of pure YBCO thin films oxygenated at low (blue), intermediate (black) and high (red) temperature. The first seven (00*l*) peaks originating from YBCO, the (200) Ni substrate, (200) CeO_2 buffer layer, (400) Y_2O_3 buffer layer and (200) YSZ buffer layer are indexed. Other phases present are labelled by symbols: ∗ NiO (No. 47-1049 EVA database), ◊ $BaCeO_3$, × Ba-Cu-O and ? unidentified peak.

With increasing oxygenation temperature the (001) and (002) YBCO peaks shift to lower 2θ values, the (004) and (005) YBCO peaks shift to higher 2θ values and the (003) and (006) peaks remain unmoved. Similar observations are made considering peak broadening, with increasing oxygenation temperature the (001) and (002) YBCO peaks broaden asymmetrically to lower 2θ values, the (004) and (005) YBCO peaks broaden asymmetrically to higher 2θ values, the (003) YBCO peaks broaden symmetrically and the (006) YBCO peaks show no broadening.

YBCO peak shifting and broadening have been previously attributed to increasing concentration of stacking faults in the YBCO thin film [60]. Interpreting the stacking fault as a $YBa_2Cu_4O_8$ (Y124) phase dispersed in a $YBa_2Cu_3O_{7-\delta}$ (Y123) matrix explains the relative shifting and broadening observed in the XRD YBCO peaks. The Y124 (002) and (004) peaks are located at lower 2θ values than the Y123 (001) and (002) peaks respectively, contributing to the Y123 peak shift and broadening towards lower angles. Similarly, the Y124 (0012) peak is located at higher angles than Y123 (005), contributing

to the Y123 (005) peak shift and broadening towards higher angles. Finally the Y124 (006) and (008) peaks are located on either sides of Y123 (003) peak contributing to its symmetrical broadening. The stacking fault density was calculated from the (001), (002), (005) and (007) peak positions as explained in section 2.2.2. The results are summarised in Table 3-2. It shows that there is a large increase of stacking faults with increasing oxygenation temperature which is an expected consequence of the oxygenation temperature [4].

Table 3-1: Lattice parameters of the pure YBCO thin films as a function of the oxygenation temperature. The *a*-axis and *b*-axis lattice parameters were measured on (020) and (200) peaks. The *c*-axis lattice parameter was calculated from the position of the YBCO (006) peaks of Figure 3-1. The uncertainties from the peak fits are less or equal to the number in brackets.

Oxygenation temperature	Low	Intermediate	High
a	0.3815(1) nm	0.3816(1) nm	0.3834(5) nm
b	0.3879(1) nm	0.3877(1) nm	0.3868(2) nm
c	1.1729(1) nm	1.1721(1) nm	1.1715(1) nm
Unit cell volume	0.1736(1) nm^3	0.1734(1) nm^3	0.1737(4) nm^3

Table 3-2: Stacking fault density of the pure YBCO films as a function of the oxygenation temperature.

Oxygenation temperature	Low	Intermediate	High
Stacking fault density	8 % ± <1 %	23 % ± 2 %	36 % ± 1 %

The YBCO *a*-axis and *b*-axis lattice parameters as a function of oxygenation temperature are also shown in Table 3-1 and were measured on the (020) and (200) peaks, using a θ-2θ scan at $\chi \approx 89°$ (see Chapter 2). The *a*-axis lattice parameter increases slightly with oxygenation temperature (0.382, 0.382 and 0.383 nm for the LT, IT and HT samples respectively) whereas the *b*-axis lattice parameter slightly decreases with oxygenation temperature (0.388, 0.388 and 0.387 nm for the LT, IT and HT YBCO samples respectively). This shows that as the oxygenation temperature increases, the degree of orthorhombicity decreases, and the *a*-axis and *b*-axis lattice parameter values tend towards the ones of the Y124 structure (Chapter 1, table 1-1, *a* = 0.3841 nm and

b = 0.3871 nm), which is in agreement with the increasing density of stacking faults. In addition, the unit cell volume was calculated to compare it to the oxygen content x in the $YBa_2Cu_3O_x$. Jorgensen *et al*. [41] showed that an increase of the unit cell volume leads to a decrease of the oxygen content in YBCO. Here, the unit cell volume is similar between samples (although slightly larger for the HT sample) and gives x = 6.90 ± 0.05 [41].

The *c*-axis misorientation (sometimes referred to out-of-plane misorientation in literature) was measured using a rocking curve on the (006) peak along the tape (at ϕ = 0°) and across the tape (at ϕ = 90°). The data is presented in Table 3-3. The *c*-axis misorientation is approximately 3.0°, 3.6° and 3.4° along the tape; and 4.2°, 5.1° and 4.7° across the tape for the LT, IT and HT samples respectively.

Table 3-3: FWHM of the rocking curve on the (006) peak (*c*-axis misorientation) and the ϕ–scan on the (103) peak (in-plane misorientation) of the pure YBCO films oxygenated low, intermediate and high temperature. The error in width from the peak fit is <0.02°.

Oxygenation temperature	*c*-axis misorientation (FWHM)		in-plane misorientation (FWHM)	
	along the tape	across the tape	along the tape	across the tape
Low	2.95°	4.23°	5.27°	6.08°
Intermediate	3.61°	5.14°	4.82°	5.46°
High	3.35°	4.71°	5.11°	6.20°

The in-plane misorientation (sometimes referred to as *ab* plane misorientation in literature) was determined using a ϕ–scan on the (103) peaks and then measuring the full width at half maximum (FWHM) of the peaks (Table 3-3). The in-plane misorientation is approximately 5.3°, 4.8° and 5.1° along the tape; and 6.1°, 5.5° and 6.2° across the tape for the LT, IT and HT samples respectively. No trend is therefore observed with the increasing oxygenation temperature. The films present a greater misorientation across the tape than along the tape due to the fabrication process of the substrate (RABiTS [24]). The substrate presents an out-of-plane and in-plane FWHM of 5-7° [24] which shows that there is an improvement in the film texturing compared to the substrate. Feldmann *et al.* had also observed that the trifluoroacetate metal organic deposition (TFA-MOD) process improves the YBCO film texturing compared to the substrate [134] which lead to a reduction of the grain boundaries in the YBCO, favourable to the critical current. Both the out-of-plane (*c*-axis) and in-plane misorientations exhibit no trend with the increasing oxygenation temperature. This non-monotonic variation was unexpected as the samples

are grown on the same substrates and the only major difference in lattice parameters is the smaller degree of orthorhombicity at high oxygenation temperature as mentioned above.

3.2 Scanning electron microscopy

Figure 3-2 presents SEM micrographs of the top surface of the pure YBCO thin films at low and high magnifications after an oxygenation cycle at different temperatures. As explained in Chapter 2, section 2.3, the micrographs exhibit a predominantly topographic contrast.

The low magnification images show homogeneous porosity at the sample surfaces. The samples' surface porosity is approximately 4.7 % for all three thin films (Table 3-4) showing that the oxygenation temperature does not have an effect on the surface porosity. The pore size was measured on the high magnification images and ranges between 20-350 nm.

Table 3-4: Pure YBCO film surface porosity as a function of the oxygenation temperature measured from the low magnification SEM micrographs of Figure 3-2.

Oxygenation temperature	Low	Intermediate	High
Porosity (%)	4.7	4.7	4.7

In addition to the porosity, the high magnification micrographs show a high density of surface particles whose size range is non-homogeneous between oxygenation temperatures as shown in Table 3-5. The HT sample presents the smallest particles while the IT sample exhibits larger particles. They were identified as Y_2O_3 that did not react to form the YBCO during the reaction cycle.

Table 3-5: Pure YBCO films surface particle diameter as a function of the oxygenation temperature measured from the high magnification SEM micrographs of Figure 3-2.

Oxygenation temperature	Particle diameter			
	Minimum	Maximum	average	Median
Low	30 nm	165 nm	87 nm	85 nm
Intermediate	55 nm	215 nm	100 nm	94 nm
High	30 nm	165 nm	80 nm	78 nm

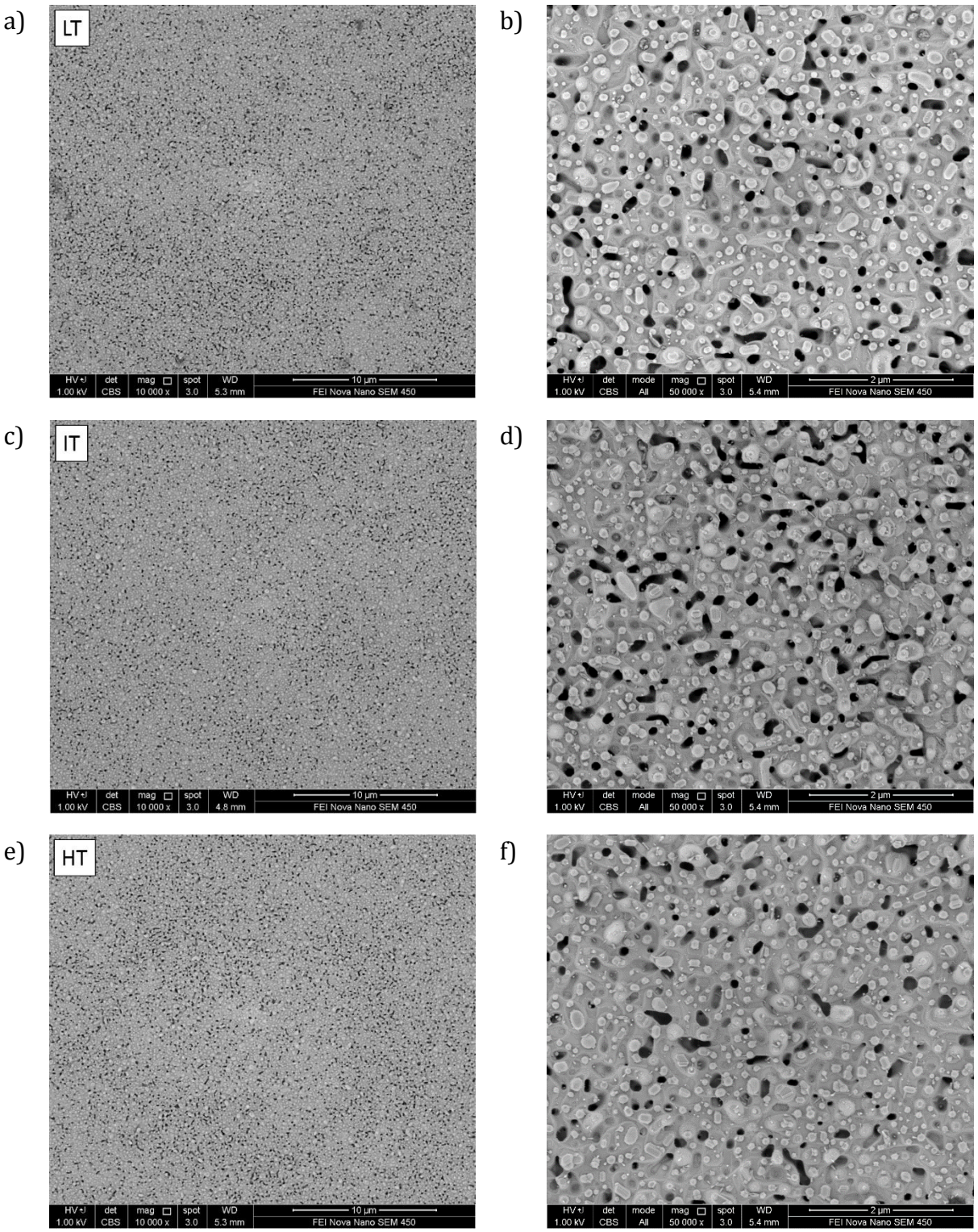

Figure 3-2: SEM micrographs of the top surface of pure YBCO thin films oxygenated at a)-b) low, c)-d) intermediate and e)-f) high temperature. Left: low magnification (10 µm scale bar). Right: high magnification (2 µm scale bar).

3.3 Energy dispersive spectroscopy

EDS analysis was performed to determine the phases present in the LT, IT and HT samples. Figure 3-3 is an example of an EDS spectrum from a IT sample. The EDS peaks used for elemental mapping are: O K_α (0.52 kV), Y L_α (1.93 kV), Ba L_α (4.46 kV) and Cu K_α (8.04 kV). These peaks do not present any major overlaps in the presented mapping regions.

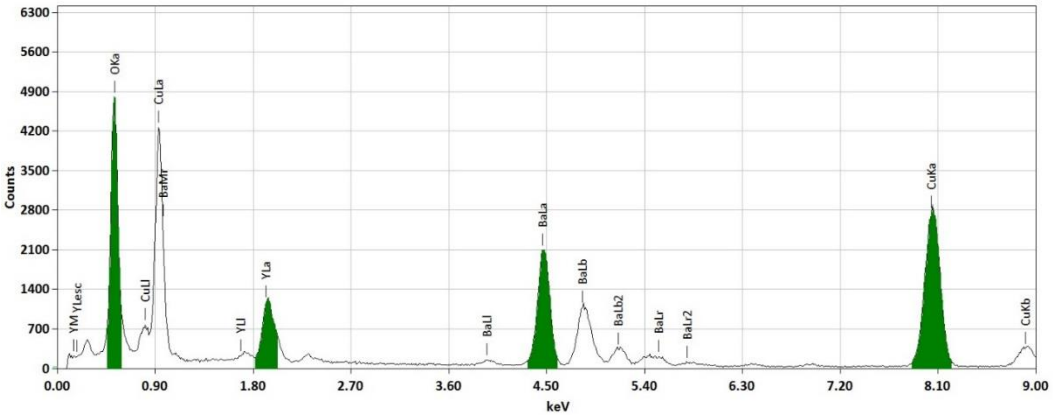

Figure 3-3: EDS spectrum of a pure YBCO thin film, with peaks used to generate elemental maps highlighted in green.

3.3.1 Low magnification elemental maps

The EDS elemental mapping presented in Figure 3-4 shows the Y, Ba, Cu and an overlay of the three elements of the LT, IT and HT samples. The maps were acquired using a JEOL 2100F operated at 200 kV. Although the resolution of the IT sample map is lower (256 × 256) than the LT and HT sample maps (512 × 512), the collection time per pixel is identical. The LT and HT specimens present a thinner region at the top right and top left respectively, which translates into a darker background visible in the maps.

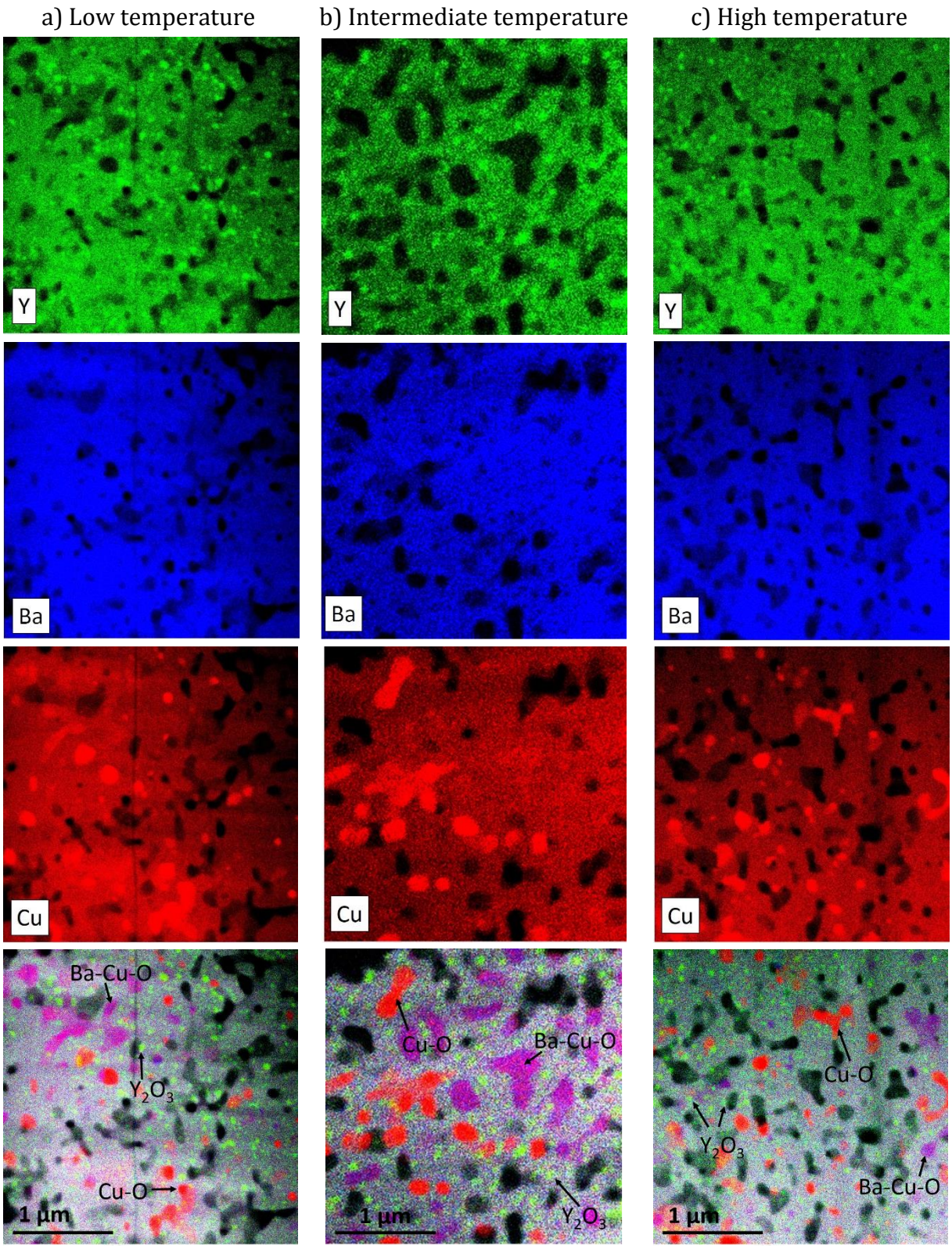

Figure 3-4: Low magnification EDS elemental maps of pure YBCO samples oxygenated at a) low, b) intermediate and c) high temperature. Y (green), Ba (blue), Cu (red). A selection of Ba-Cu-O, Cu-O and Y_2O_3 particles are highlighted in the overlay. Scale bar shown in overlay.

The Y elemental maps show an even background with periodic regions of high and low concentrations. The regions of localised high Y concentration correspond to low Ba and Cu concentration which confirms that these are Y_2O_3 particles. The regions of localised low Y concentration correspond with either an even Ba and Cu concentration (Ba-Cu-O); a high Cu concentration (Cu-O) or a low Ba and Cu concentration (voids).

These various regions in the YBCO thin films are more clearly seen in the EDS map overlay which shows the Ba-Cu-O, Cu-O, Y_2O_3 and voids respectively in an even white YBCO background. These maps show that the samples exhibit a high concentration of Y_2O_3 particles dispersed homogeneously through the bulk. The HT sample also presents the smallest density of Cu-O and Ba-Cu-O phases than the other samples.

3.3.2 High magnification elemental maps

Figure 3-5 shows high magnification EDS maps of the same samples as presented in Figure 3-4. The same elements (Y, Ba and Cu) and phases (Ba-Cu-O, Cu-O, Y_2O_3) are visible as in the lower magnification maps.

The Y_2O_3 particles size was measured on the Y EDS elemental maps from Figure 3-5. Similarly to the particles measured on the SEM micrograph, the IT sample presents bigger particles and the HT sample presents the smallest particles. The range of particle size also decreases with increasing oxygenation temperature.

Table 3-6: Y_2O_3 particle diameter measured on Figure 3-5 as a function of the oxygenation temperature.

Oxygenation temperature	Particle diameter			
	Minimum	Maximum	Average	Median
Low	32 nm	130 nm	52 nm	42 nm
Intermediate	31 nm	120 nm	63 nm	54 nm
High	24 nm	58 nm	35 nm	32 nm

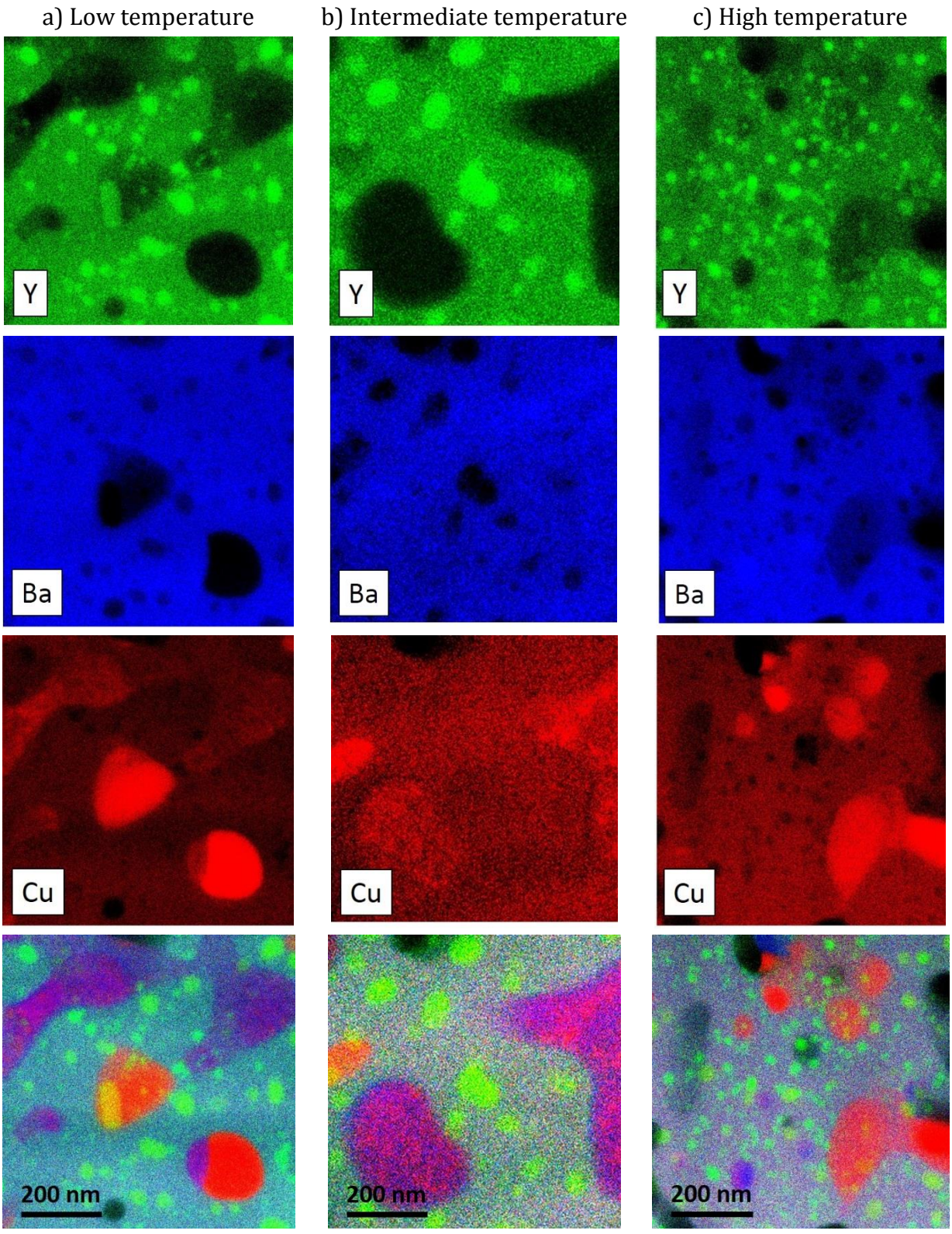

Figure 3-5: High magnification EDS elemental maps of pure YBCO samples oxygenated at a) low, b) intermediate and c) high temperature. Y (green), Ba (blue), Cu (red). Scale bar shown in overlay.

3.4 Transmission electron microscopy

3.4.1 Low magnification structure of the films

Figure 3-6 shows low magnification TEM micrographs of LT, IT and HT YBCO samples. The specimens are cross-sectioned, oriented with the *c* direction in the plane of the images as indicated by the white arrows. The Ni substrate, the Y_2O_3, YSZ and CeO_2 buffer layers and the YBCO are labelled. Between the CeO_2 and the YBCO, an interfacial reaction layer of $BaCeO_3$ can be observed. XRD shows that the $BaCeO_3$ layer is already present in the samples after the reaction cycle, before the oxygenation step. Finally, Y_2O_3 nanoparticles and Ba-Cu-O phases are also visible within the YBCO matrix at each of the oxygenation temperatures.

As expected the thickness of the films does not change with oxygenation temperature, remaining approximately 950 nm. The film thickness is controlled by the deposition process and the reaction cycle. At low magnification, the three films appear relatively similar in thickness, porosity and observed phases.

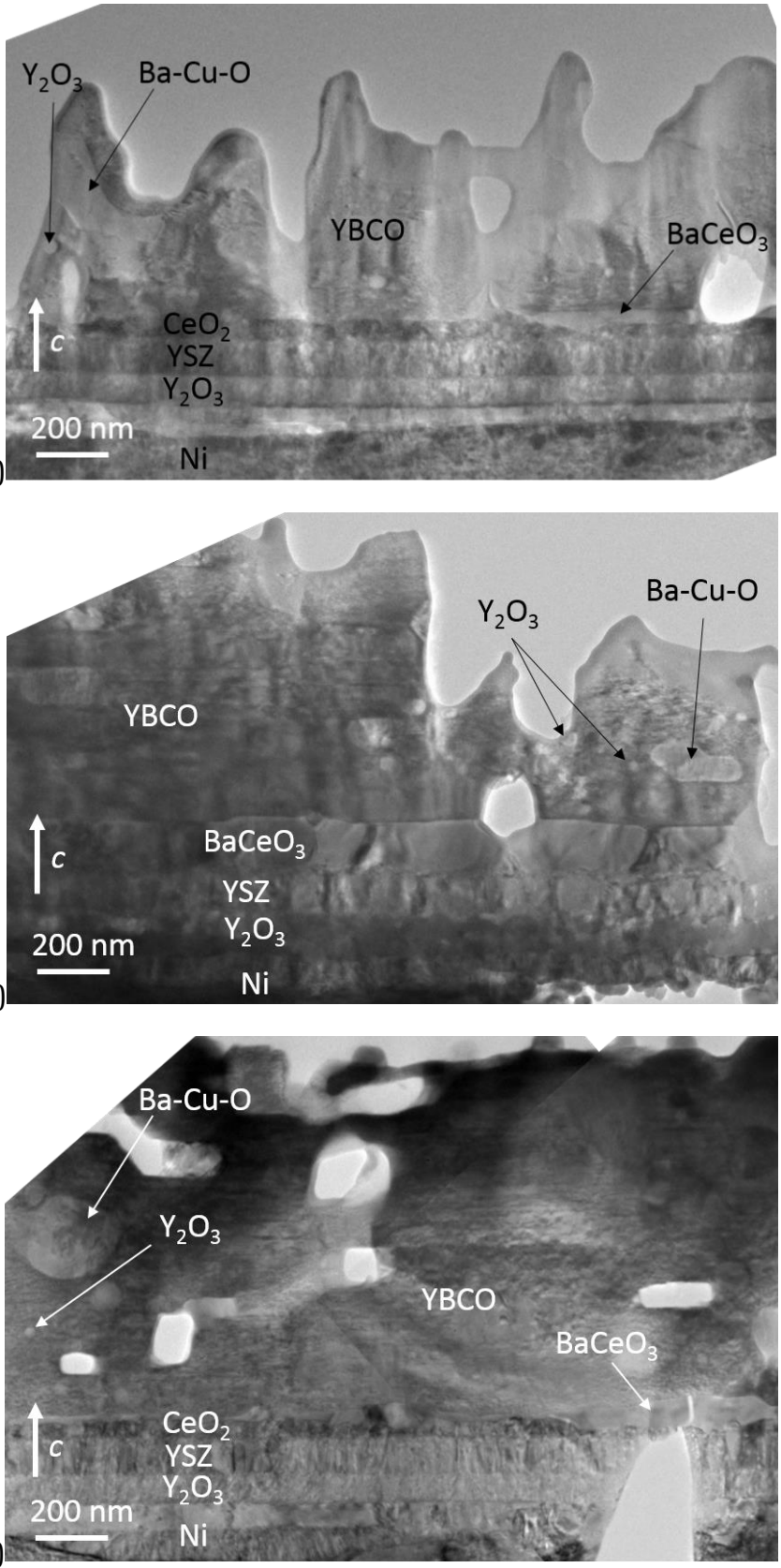

Figure 3-6: Low magnification TEM micrographs of pure YBCO samples oxygenated at a) low, b) intermediate and c) high temperature. The Ni substrate, Y_2O_3, YSZ and CeO_2 buffer layers and YBCO films are labelled. A selection of Ba-Cu-O, $BaCeO_3$ phases and Y_2O_3 particles are labelled.

3.4.2 High resolution imaging

HRTEM micrographs of the LT, IT and HT samples are presented in Figure 3-7, Figure 3-8 and Figure 3-9 respectively. Inset are the selected area diffraction (SAD) patterns of each corresponding micrograph. The micrographs were acquired within the YBCO film matrix, away from secondary phases (such as Ba-Cu-O and $BaCeO_3$) and particles (Y_2O_3) observed in the EDS data.

The three samples are oriented in the [100]/[010] zone axis as shown by their respective diffraction patterns. The SAD pattern for the LT sample shows sharp reflections with a small amount of angular scatter, suggesting disorder in the sample structure. The SAD pattern for the IT sample shows sharp reflections with homogeneous intensity. The SAD pattern for the HT sample shows streaking in the (00*l*) direction. This indicates a *c*-axis lattice parameter variation in the YBCO matrix, which is attributed to the high stacking fault density and is consistent with XRD observations (Figure 3-1). The (001) planar spacing, determined from the SAD patterns, is 1.20 ± 0.02 nm, 1.19 ± 0.02 nm and 1.26 ± 0.03 nm for the LT, IT and HT samples respectively. Those values are greater than the ones given by XRD (~1.17 nm) because the reflexions in the SAD pattern include the stacking faults present in the sample. In addition, considering the errors, those values are in agreement with the increasing stacking fault density with oxygenation temperature. Finally due to the similar values between the *a*-axis and *b*-axis lattice parameters of the YBCO structure, it is not possible to determine whether the specimen is oriented in the [010] or [100] zone axis by measuring the spacing on the SAD, considering the error.

In the HRTEM micrographs, the brightest lines of atoms correspond to CuO chains and are annotated on the right. The LT sample (Figure 3-7) shows a YBCO structure with some disorder. The presence of a stacking fault (region 2, indicated with the arrow) causes structural distortions extending approximately 5 nm into the adjacent YBCO. Several brighter areas (regions 1, 3, 4, 5 and 6) included in the matrix indicate local strain in the YBCO extending across regions of 2-5 nm size. The contrast of lattice fringes in the *c* direction is different between the top half and the bottom half of the image separated by the stacking fault. This contrast difference is likely due to a misorientation of the structure in the *c* direction as it is unlikely to be due to thickness or phase differences. All these elements contribute to the disorder of the YBCO stack.

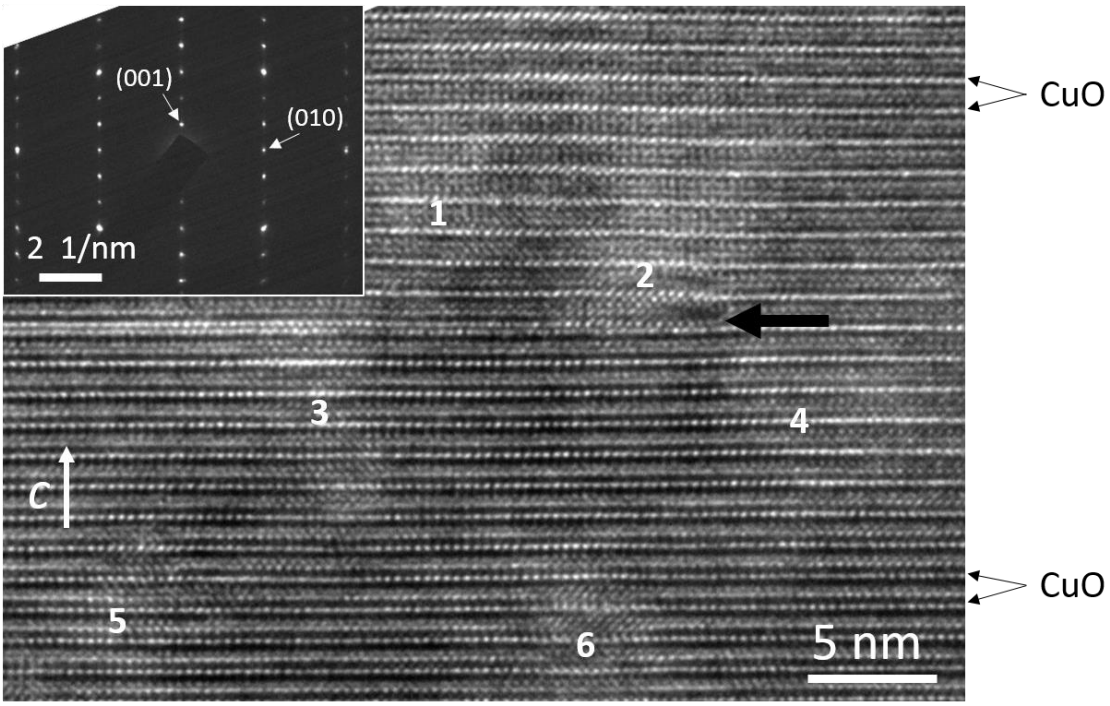

Figure 3-7: HRTEM micrograph of a pure YBCO film oxygenated at low temperature. The brightest planes of atoms correspond to CuO and are annotated on the right. A stacking fault in the middle of the image is highlighted with the large arrow, and six strained regions are numbered. Inset is the corresponding SAD pattern.

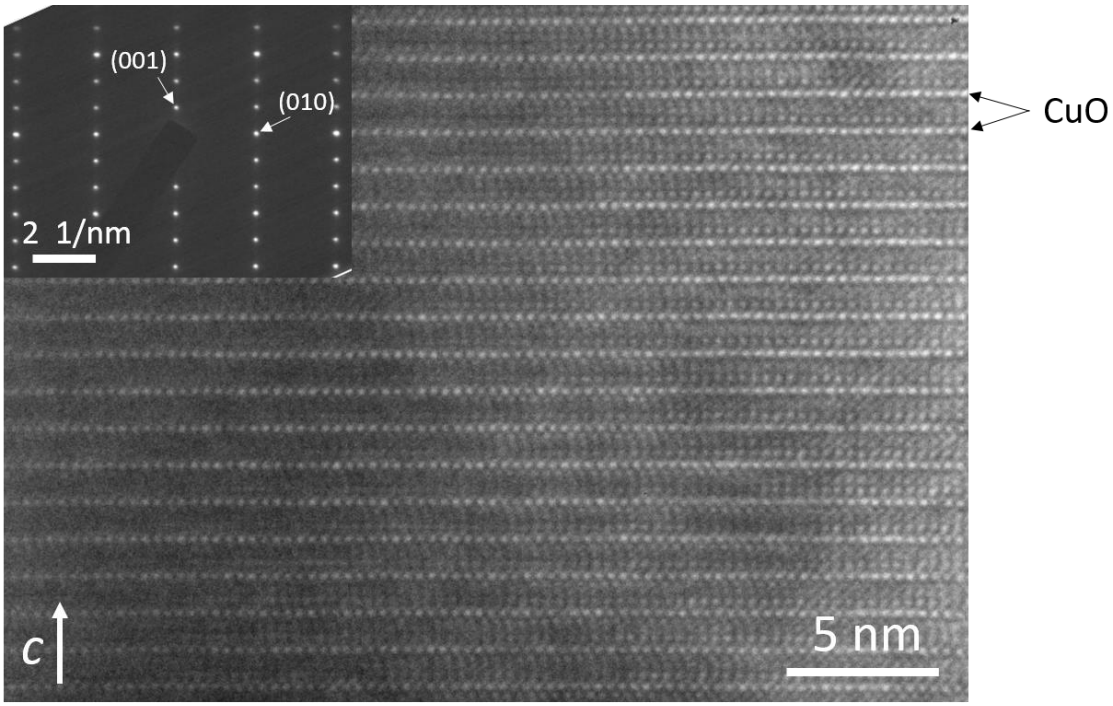

Figure 3-8: HRTEM micrograph of a pure YBCO film oxygenated at intermediate temperature. The brightest planes of atoms correspond to CuO and are annotated on the right. Inset is the corresponding SAD pattern.

The IT sample presents large areas of uniform and well stacked YBCO as shown in Figure 3-8. The left part of the image shows less well defined lattice fringes due to an increase in the sample thickness from right to left. The structure does not exhibit major disorder as seen in the LT sample.

The HT sample presents a high density of stacking faults throughout the entire film thickness as shown by Figure 3-9. Many of the YBCO unit cells contain an extra CuO layer, some of them running across the entire image (arrows on the right side), while others start in the middle of the image (arrows in the middle). The stacking faults exhibit either the square or triangular configuration characteristic of the [010] and [100] orientation respectively, as explained in Chapter 1. This shows that along the growth direction, the YBCO structure periodically switches from the [010] to the [100] direction.

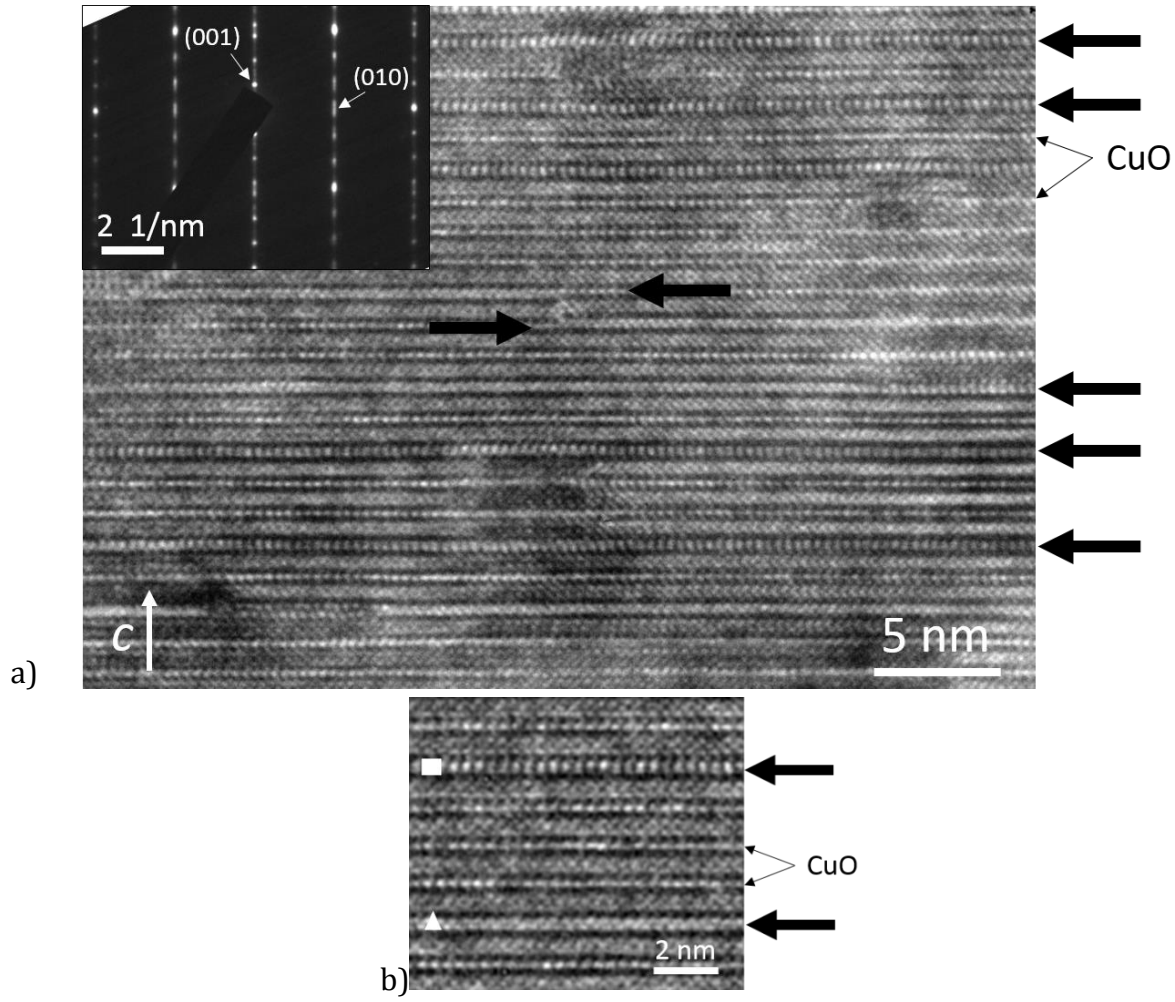

Figure 3-9: HRTEM micrographs of a pure YBCO sample oxygenated at high temperature showing a large stacking fault density. The brightest planes of atoms correspond to CuO. a) Stacking faults are highlighted with large arrows. Inset is the corresponding SAD pattern. b) Enlarged view showing two stacking faults with characteristic square and triangular configuration corresponding to [010] and [100] orientation respectively.

3.5 Microstructure summary of the pure YBCO films

The YBCO thin films were successfully epitaxially grown on the textured RABiTS substrate using TFA-MOD procedure. The following microstructural observations were made for the YBCO samples:

1. The surface porosity, size and distribution (4 %) are independent of the oxygenation temperature.
2. The film texturing (*c*-axis and in-plane misorientations) did not exhibit a monotonic trend.
3. The stacking fault density, increases dramatically with increasing oxygenation temperature (up to 36 %).
4. The *c*-axis lattice parameter does not change with oxygenation temperature.
5. The *a*-axis lattice parameter decreases (from 0.388 nm to 0.387 nm) and the *b*-axis lattice parameter increases (from 0.382 nm to 0.383 nm) with increasing oxygenation temperature, showing that the degree of orthorhombicity decreases with increasing oxygenation temperature.
6. All the samples showed the expected presence of Cu-rich phases, however the HT sample has the smallest Y_2O_3 particles and a lower density of Cu-rich phases.
7. From HRTEM imaging the YBCO exhibits: some disorder in the LT sample; little disorder in the IT sample and extensive disorder in the HT sample due to the high density of stacking faults. Further investigation is required to conclusively determine the origin of the variation in the LT sample.

The microstructural changes as a function of oxygenation temperature, as summarised by observations 3 to 6 above, are attributed to the mechanism of stacking fault density formation in YBCO.

The formation of YBCO thin films follows three main stages: decomposition, reaction and oxygenation. After the reaction stage the YBCO thin film contains $YBCO_{6.5}$, Y_2O_3 nanoparticles and Cu-rich phases (Ba-Cu-O and Cu-O). During oxygenation, $YBCO_{6.5}$ oxidises to $YBCO_{7-\delta}$, and the Cu-rich phases are used as source of Cu-O for the stacking fault formation [4]. The stacking faults grow as an intercalation growth into the parent YBCO structure. Furthermore, if the temperature is sufficiently high, further YBCO can form through the reaction of the Ba-Cu-O phase with the Y_2O_3. Due to improved kinetics

the concentration of stacking faults increases with increasing oxygenation temperature (observation 3).

If the stacking fault is considered as a Y124 phase dispersed in a parent Y123 matrix, it would be anticipated that an increasing stacking fault density would not alter the measured *c*-axis lattice parameter but lead to a decreased orthorhombicity through *a*-axis and *b*-axis lattice parameters change. The Y123 *c*-axis lattice parameter is distinct from the Y124 *c-axis* lattice parameter and as such the Y123 *c*-axis lattice parameter remains unaltered by the increasing stacking faults density with increasing oxygenation temperature (observation 4). However, the *a*-axis and *b*-axis lattice parameters of Y123 and Y124 are very similar in XRD. The *a*-axis lattice parameter is smaller for Y123 in comparison to Y124 and the *b*-axis lattice parameter is larger for the Y123 in comparison to Y124. As such, the observed decrease in orthorhombicity with increasing oxygenation temperature is consistent with the observation of increasing stacking fault density (observation 4).

It would be anticipated that, if the formation of stacking faults originates from the Cu-rich phases, Ba-O rich phases should be found in the YBCO thin films, but there is no clear evidence of this in the EDS and XRD data. It is as such, proposed that the Ba-Cu-O reacts with the Y_2O_3 nanoparticles to form additional YBCO in a similar way as in the reaction cycle for high enough oxygenation temperature [35]. This is consistent with the observation that the Y_2O_3 nanoparticle sizes are the smallest and the Ba-Cu-O phase density is the lowest for the HT sample.

3.6 Critical current

This section presents the electrical properties of the pure YBCO thin films. The self-field I_c is first presented. The critical current was then measured under a 1 T applied magnetic field at 30 K and 77 K as a function of the magnetic field angle. Finally, the I_c data at 1 T was normalised to the self-field I_c to study vortex pinning behaviour.

3.6.1 Self-field critical current

Figure 3-10 shows the self-field I_c as a function of operating temperature of the LT, IT and HT YBCO samples. Note that the word "operating" temperature is used to avoid confusion with the "oxygenation" temperature. As explained in Chapter 1, the self-field I_c corresponds to measurements of the critical current under no applied magnetic field. The

vortex pinning is therefore less significant in this case. This provides a baseline of the maximum current that can be supported by the samples. The measurements were performed at operating temperatures between 25-90 K. It is observed that the self-field I_c decreases with increasing operating temperature, reaching zero as the temperature approaches T_c. Like the other superconducting properties discussed in section 1.5, the critical current is temperature dependent and decreases with increasing temperature, to zero at T_c [39, 135]. The three samples exhibit a similar T_c of approximately 87 K, confirming the similar global oxygen content between the samples [136, 137], which is in agreement with the XRD results. This value is slightly lower than the maximum T_c achievable in YBCO (93 K) which occurs at slightly higher oxygen content [17].

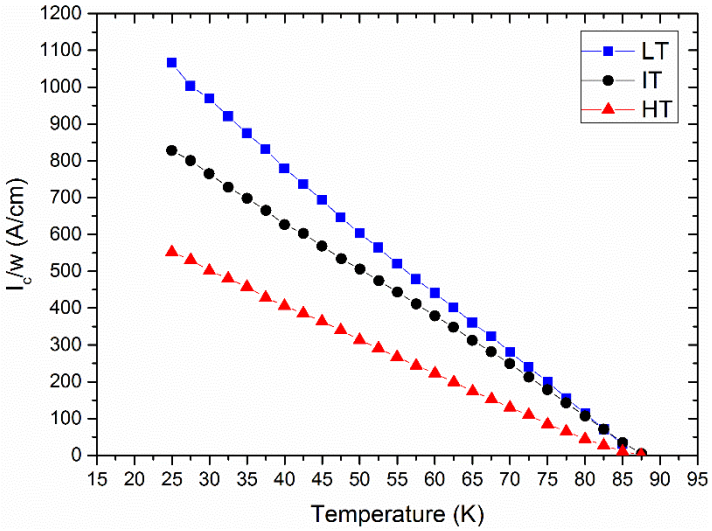

Figure 3-10: Self-field critical current as a function of temperature of pure YBCO thin films oxygenated at low (blue), intermediate (black) and high (red) temperature.

In addition, the self-field I_c is higher for lower oxygenation temperatures. A first hypothesis to explain the higher self-field I_c at lower oxygenation temperature would be to attribute it to the grain boundaries. Excellent film texturing is an important criterion for achieving high critical current as an increasing grain misorientation leads to a decrease of I_c [18, 134]. A FWHM of 5° or less is required to reach high I_c [138] as high angle grain boundaries act as barriers to the current flow. However, here it was shown from XRD analysis that no trend in film texturing (*c*-axis and in-plane misorientation) was observed with the oxygenation temperature. Similarly, the porosity of the samples is identical between oxygenation temperatures. Therefore grain boundaries and porosity being the sources of difference in self-field critical current here are dismissed.

The difference in self-field I_c with oxygenation temperature could be explained by a different amount of localised regions within the films that have a lower I_c. The clearest structural difference between the samples is the increase of Y124-like stacking fault defects with increasing oxygenation temperature. Besides having a lower T_c of 80 K, Y124 is known to have lower doped charge on the CuO_2 planes [139]. Underdoped cuprates present a low critical current, which some authors have attributed to the presence of competing electronic correlation that weakens superconductivity [124, 140]. Therefore the increase of stacking fault density is proposed to be the source that contributes to decreasing self-field critical current.

3.6.2 Critical current under 1 T magnetic field

Figure 3-11 shows the critical current as a function of the applied magnetic field angle measured at 77 K and 30 K under 1 T applied magnetic field.

At 77 K LT and IT samples present a similar isotropic component of the critical current of 15-20 A/cm. The HT sample has a very low, close to zero, isotropic I_c. At 90°, corresponding to measurements with the magnetic field in the *ab* plane, all samples exhibit a critical current peak characteristic of the current flowing in the *ab* plane. The IT sample presents the strongest peak with I_c^{max} = 90 A/cm, while the LT and HT samples present a lower I_c^{max} of 47 A/cm and 40 A/cm respectively. It is noted that at 77 K, the temperature is very close to T_c of Y124 (80 K), which possibly explains the lower I_c at any magnetic field angles of the HT sample, which presents a high density of stacking faults. In addition, at 0°, the higher proportion of non-superconducting Y124-like stacking faults may cause vortex bending [39]. Vortex bending is observed when there is a high proportion of a nearly non-superconducting phase and result in very low critical current.

In contrast, at 30 K (Figure 3-11b), the LT sample has the highest I_c at all magnetic field angles. At 90°, the critical current was 896 A/cm, 715 A/cm and 472 A/cm for the LT, IT and HT samples respectively.

For both 77 K and 30 K measurements, it was expected that the high density of stacking faults in the HT sample would improve the critical current at 90° and give higher I_c than the two other samples. However it appears that at both 77 K and 30 K, this sample presents the lowest I_c suggesting that its microstructure, and especially the high stacking fault density, is detrimental to critical currents at 1 T as it was proposed for the self-field I_c.

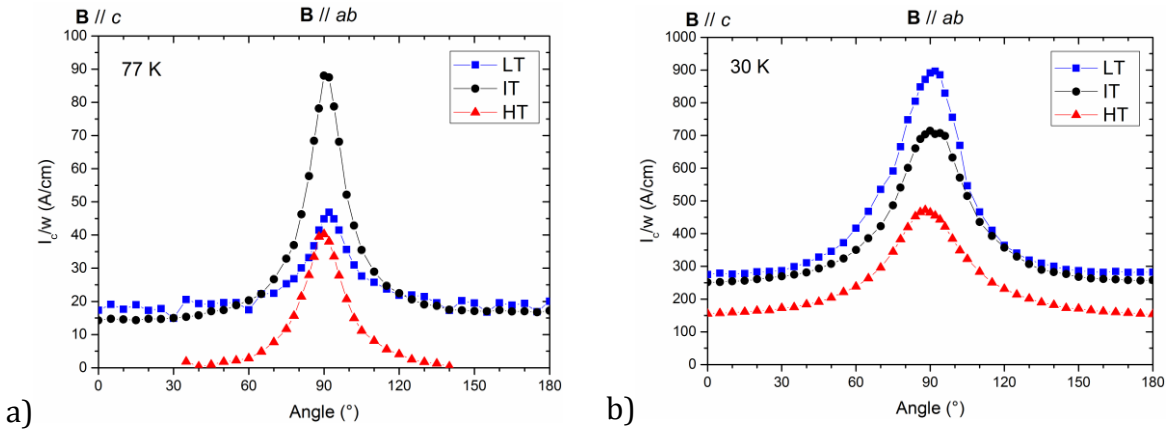

Figure 3-11: Critical current as a function of the applied magnetic field angle measured at a) 77 K and b) 30 K of pure YBCO thin films oxygenated at low (blue), intermediate (black) and high (red) temperature.

3.6.3 Vortex pinning under 1 T magnetic field

Following reference [124], to compare the pinning characteristic of the thin films, the data was normalised to the self-field I_c at the corresponding measurement temperature of each thin film (Figure 3-12). This plot then provides information about the collective pinning behaviour of the entire defect landscape, by removing the self-field I_c component.

At 77 K the LT and IT samples show a similar isotropic pinning, while the HT sample shows a very weak isotropic pinning. The LT and IT samples present the smallest and the largest *c*-axis misorientation respectively (Table 3-3), suggesting that this misorientation within this range does not affect the isotropic pinning. The same observation is made for the variation in Y_2O_3 particle size which does not seem to influence the isotropic pinning. This suggests that despite the structural disparities of the LT and IT samples, the microstructure contributes in a similar way to isotropic vortex pinning at 77 K.

Moreover at 90°, the IT and HT samples have an equivalent anisotropic pinning from the stacking faults, while the LT sample exhibits a much smaller peak. Despite the equivalent absolute anisotropic pinning for the IT and HT samples, the difference between the isotropic pinning (at 0°) and the maximum anisotropic pinning (at 90°) is very strong for the HT sample. This suggests that the large stacking fault density in the HT sample does contribute to increasing the pinning at 77 K under 1 T applied magnetic field. Finally, in spite of the small Y_2O_3 nanoparticles in the HT samples the isotropic pinning is low.

In contrast at 30 K, the three samples have very similar pinning behaviour for the three different oxygenation temperatures (Figure 3-12). This suggests that the differences in

the defect landscape created by the different oxygenation temperatures do not influence the vortex pinning at 30 K. More specifically, the stacking faults, which are providing significant pinning at 77 K, do not have an effect at 30 K and the anisotropic pinning that remains is due to intrinsic pinning. The stacking faults contributing to vortex pinning at 77 K, but not at 30 K, is in agreement with previous observation [124], the explanation being that the Y124 phase is only weakly superconducting at 77 K, but more strongly superconducting at 30 K.

Overall, the films present a higher normalised I_c when measured at 30 K than at 77 K. At low operating temperature, the coherence length (calculated in Chapter 1) is much smaller (1.7 nm) than at 77 K (3.4 nm). This allows the smaller defects present in the samples to play a role in the vortex pinning at low temperature [39].

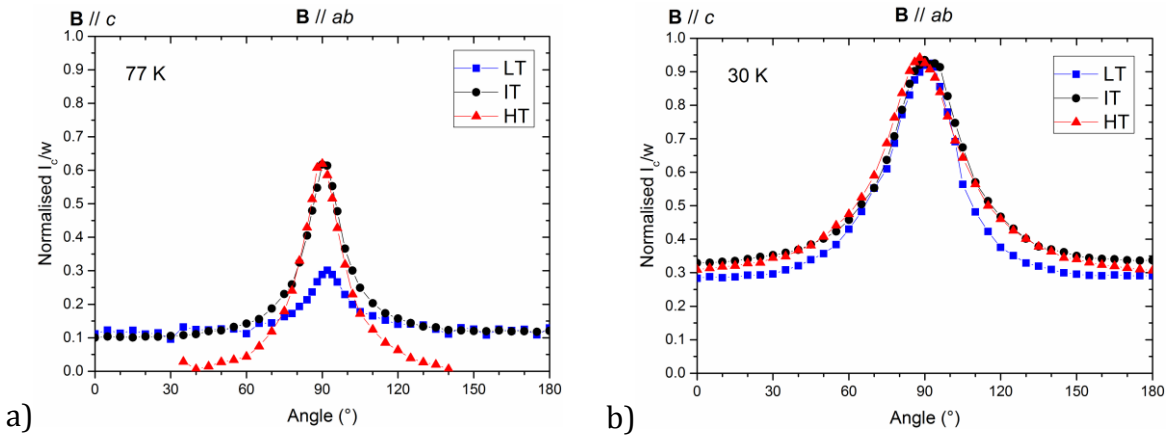

Figure 3-12: Normalised critical current data of Figure 3-11 to the self-field I_c (Figure 3-10) at a) 77 K and b) 30 K of pure YBCO thin films oxygenated at low (blue), intermediate (black) and high (red) temperature.

3.7 Summary

This chapter presented the structural and electrical characterisation of the pure YBCO films. It was shown that the sample's microstructure is sensitive to increasing oxygenation temperature with the main consequence to increase the stacking fault density.

From critical current measurements, the self-field I_c decreases with increasing oxygenation temperature. Under a 1 T applied magnetic field, the pinning behaviour at 30 K is similar for all oxygenation temperatures, while at 77 K, the low and high oxygenation temperature samples exhibit the lowest anisotropic and isotropic pinning respectively.

It was concluded that the stacking faults have two main effects on the critical current. Firstly they have a detrimental effect on the self-field I_c. Secondly, although they enhance pinning at 77 K, they do not improve the pinning at 30 K. It is proposed that this is due to low critical temperature of the Y124 phase (80 K), and which make this phase weakly superconducting at 77 K and strongly superconducting at 30 K.

The observations made in the microstructure and in the electrical behaviour of the pure YBCO samples provided a baseline for comparison with the effect of introducing Dy into the samples which is presented in Chapter 4.

Chapter 4 Dy-doped YBCO film microstructure and electrical properties

This chapter presents the structural and electrical characterisation of Dy-doped YBCO thin films oxygenated at low (LT), intermediate (IT) and high temperature (HT). The aim of this chapter is to conduct a detailed microstructural characterisation of the Dy-doped YBCO, for which the oxygenation temperature modifications were identical to the pure YBCO samples studied in Chapter 3, and correlate the microstructural features with the measured critical current. The samples were prepared following the same procedure as the pure YBCO samples presented in Chapter 3, with an addition of 50 % Dy in the precursor solution as described in Chapter 2. Similarly to Chapter 3, and for ease of comparison, the X-ray diffraction (XRD), scanning electron microscopy (SEM), energy dispersive spectroscopy (EDS), transmission electron microscopy (TEM) and critical current (I_c), results are presented with the aim of studying the influence of the oxygenation temperature on the microstructure and I_c. Finally the microstructure-critical current relationship of Dy-doped YBCO samples are compared with the pure YBCO samples.

4.1 X-ray diffraction

XRD measurements were performed to determine the phases present, the phase texturing, the film lattice parameters, the out-of-plane misorientation and the in-plane misorientation.

Figure 4-1 is a θ-2θ XRD pattern of the Dy-doped YBCO thin films oxygenated at low (blue), intermediate (black) and high (red) temperature. For ease of comparison, and similarly to the pure YBCO samples presented in Chapter 3, the plots are normalised to the maximum intensity of the (200) Ni peak from the substrate. The three XRD patterns are almost identical presenting the same peaks, at the same 2θ position with similar intensity, suggesting that the oxygenation temperature does not strongly affect the phases and the lattice parameters of the Dy-doped YBCO thin films. Similarly to the pure YBCO samples, the presence of the (00*l*) peaks only confirms the *c*-axis epitaxial growth of the films on the substrate. Similarly, the strong texturing of the buffer layers on the Ni

substrate is confirmed by only the CeO_2 (200), YSZ (200) and Y_2O_3 (400) peaks being present.

It would be expected that the Dy partially substitutes the Y in the YBCO unit cell due to the small difference in ionic radius between the Y^{3+} (1.019 Å) and the Dy^{3+} (1.027 Å) [47]. This is verified further by chemical analysis in section 4.3. The superconducting film is therefore referred to as (Y,Dy)BCO in the text. In addition, it is assumed that the peaks labelled as $(Y,Dy)_2O_3$ are a solid solution between Y_2O_3 and Dy_2O_3. Y_2O_3 (No. 41-1105 EVA database) and Dy_2O_3 (No. 22-0612 EVA database) both have a cubic crystal structure with very similar lattice parameters of 1.060 nm and 1.067 nm respectively. As many of the $(Y,Dy)_2O_3$ peaks are present in the XRD pattern, this suggests that the $(Y,Dy)_2O_3$ particles are randomly oriented within the film.

NiO and $BaCeO_3$ peaks are also both observed. The NiO forms due to a small extent of Ni substrate oxidation and the $BaCeO_3$ forms at the YBCO-CeO_2 buffer layer interface [75, 141].

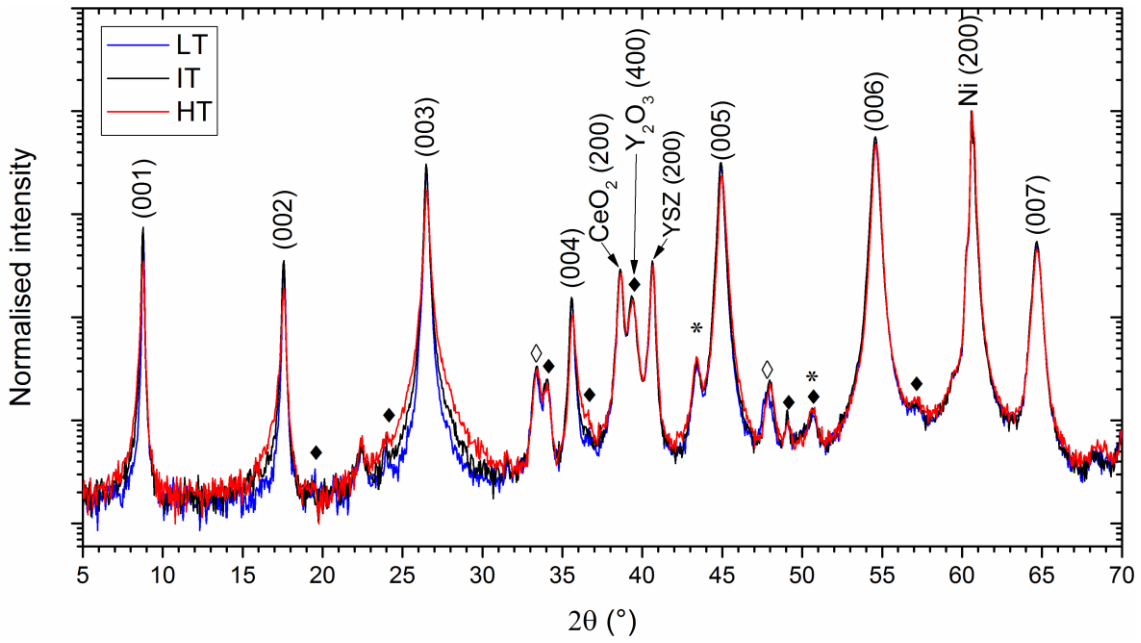

Figure 4-1: X-ray diffraction θ-2θ scan of Dy-doped YBCO thin films oxygenated at low (blue), intermediate (black) and high (red) temperature. The first seven (00*l*) peaks originating from (Y,Dy)BCO, the (200) Ni substrate, the (200) CeO_2 buffer layer, the (400) Y_2O_3 buffer layer and the (200) YSZ buffer layer peaks are indexed. Other phases present are labelled by symbols: ◆ $(Y,Dy)_2O_3$, ◊ $BaCeO_3$ and ∗ NiO.

The (Y,Dy)BCO *c*-axis lattice parameter is determined from the (006) peak position as 1.173 nm and does not change with oxygenation temperature. This is similar to the values measured in Chapter 3 for the pure YBCO thin films (Figure 3-1). This suggests that the *c*-axis lattice parameter remains unchanged with Dy addition, which is expected as the ionic radius of Dy^{3+} is only 0.8 % larger than the one of Y^{3+}.

The (Y,Dy)BCO peaks still present a slight broadening (asymmetrical for (001), (002) and (004)) with increasing oxygenation temperature but they are not as broad as the pure YBCO (00*l*) peaks (Figure 3-1). The (Y,Dy)BCO (00*l*) peaks present a small decrease of intensity with increasing oxygenation temperature. The combination of (00*l*) (Y,Dy)BCO peak broadening and intensity reduction with oxygenation temperature therefore still suggests an increasing stacking fault density with the oxygenation temperature, however the calculated density is low in comparison with the pure YBCO thin films. The stacking fault density was calculated based on the (001), (002), (005) and (007) peaks position using the method explained in Chapter 2. Those peaks do not shift and broaden as much as the peaks from the pure YBCO samples and as such the density of stacking fault (Table 4-1) is much lower than for the pure YBCO films. This is in agreement with previous research [4] that the addition of rare-earth in YBCO coated conductors hinders the formation of stacking faults.

Table 4-1: Stacking fault density of the Dy-doped YBCO films as a function of the oxygenation temperature.

Oxygenation temperature	Low	Intermediate	High
Stacking fault density	6 % ± <1 %	10 % ± 2 %	12 % ± 2 %

The *a*-axis and *b*-axis lattice parameters were measured using the (200) and (020) peaks of a θ-2θ scan at χ = 90° (see Chapter 2). Table 4-2 presents the *a*-axis and *b*-axis lattice parameters of the Dy-doped YBCO thin films as a function of the oxygenation temperature. For the Dy-doped YBCO thin films, the in-plane lattice parameters are relatively similar between the films: *a* = 0.382 nm and *b* = 0.388 nm. In addition, the unit cell volume is similar between the samples and close to the one of the pure YBCO samples, showing that the samples present a similar oxygen content x = 6.90 ± 0.05 [41].

Table 4-2: Lattice parameters of the Dy-doped YBCO thin films as a function of the oxygenation temperature. The *a*-axis and *b*-axis lattice parameters were measured on (020) and (200) peaks. The *c*-axis lattice parameter was calculated from YBCO (006) peaks of Figure 4-1. The uncertainties from the peak fits are less than the number in bracket.

Oxygenation temperature	Low	Intermediate	High
a	0.3817(1) nm	0.3817(1) nm	0.3822(1) nm
b	0.3877(1) nm	0.3877(1) nm	0.3876(1) nm
c	1.1733(1) nm	1.1730(1) nm	1.1726(1) nm
Unit cell volume	0.1736(1) nm^3	0.1736(1) nm^3	0.1737(1) nm^3

The *c*-axis misorientation was measured from a rocking curve on the (006) peak along the tape (at 0° and 180°) and across the tape (at 90° and 270°) and then measuring the full width at half maximum (FWHM) of the peaks. The data is presented in Table 4-3. The three thin films present similar *c*-axis misorientations along the tape (3°) and across the tape (4°) and do not show oxygenation temperature dependence.

The average misorientation of the grain in the *ab* plane was determined using a ϕ–scan on the (103) peaks and then measuring the FWHM of the peaks (Table 4-3). The in-plane rotation for the (Y,Dy)BCO films is about 5° along the tape and 6° across the tape and does not change substantially with the oxygenation temperature.

Similarly to the pure YBCO samples, the out-of-plane and in-plane misorientations are overall greater across the tape than along the tape due to the fabrication process of the rolling-assisted biaxially textured substrate (RABiTS) [24]. As opposed to the pure YBCO samples, the in-plane and out-of-plane misorientation of the Dy-doped samples are independent of the oxygenation temperature.

Table 4-3: FWHM of the out-of-plane (*c*-axis misorientation) and in-plane (*ab* plane rotation) of the Dy-doped YBCO thin films oxygenated at low, intermediate and high temperature. The error from the curve fit is <0.01°.

Oxygenation temperature	*c*-axis misorientation (FWHM)		*ab* in-plane rotation (FWHM)	
	along the tape	across the tape	along the tape	across the tape
Low	3.10°	4.29°	4.99°	5.98°
Intermediate	3.12°	4.33°	5.16°	5.92°
High	3.11°	4.30°	5.16°	6.38°

4.2 Scanning electron microscopy

Figure 4-2 presents SEM micrographs at low and high magnification of the top surface of Dy-doped YBCO thin films after the oxygenation cycle at low, intermediate and high temperature.

Unlike the pure YBCO films (Figure 3-8), the porosity of the (Y,Dy)BCO thin films is non-homogeneous. The film is characterised by porous regions (dark) surrounding denser areas of about 5-15 μm in diameter. The pore size is between 50-200 nm.

The surface porosity was determined using the method described in Chapter 2 (section 2.3). The surface porosity results are presented in Table 4-4 and are approximately 2 %. This is less than half the porosity of the pure YBCO thin films, suggesting that the addition of Dy leads to denser films. As for the pure YBCO thin films, the oxygenation temperature does not have an effect on the thin films porosity.

Table 4-4: Dy-doped YBCO thin film surface porosity measured from the low magnification SEM images of Figure 4-2.

Oxygenation temperature	Low	Intermediate	High
Porosity (%)	2.1	1.9	2.1

In addition to the porosity, the high magnification micrographs show a high density of small particles (light grey) identified as $(Y,Dy)_2O_3$ between 10-60 nm in diameter at the surface of the film and a few larger precipitates of about 500 nm identified as Cu-O.

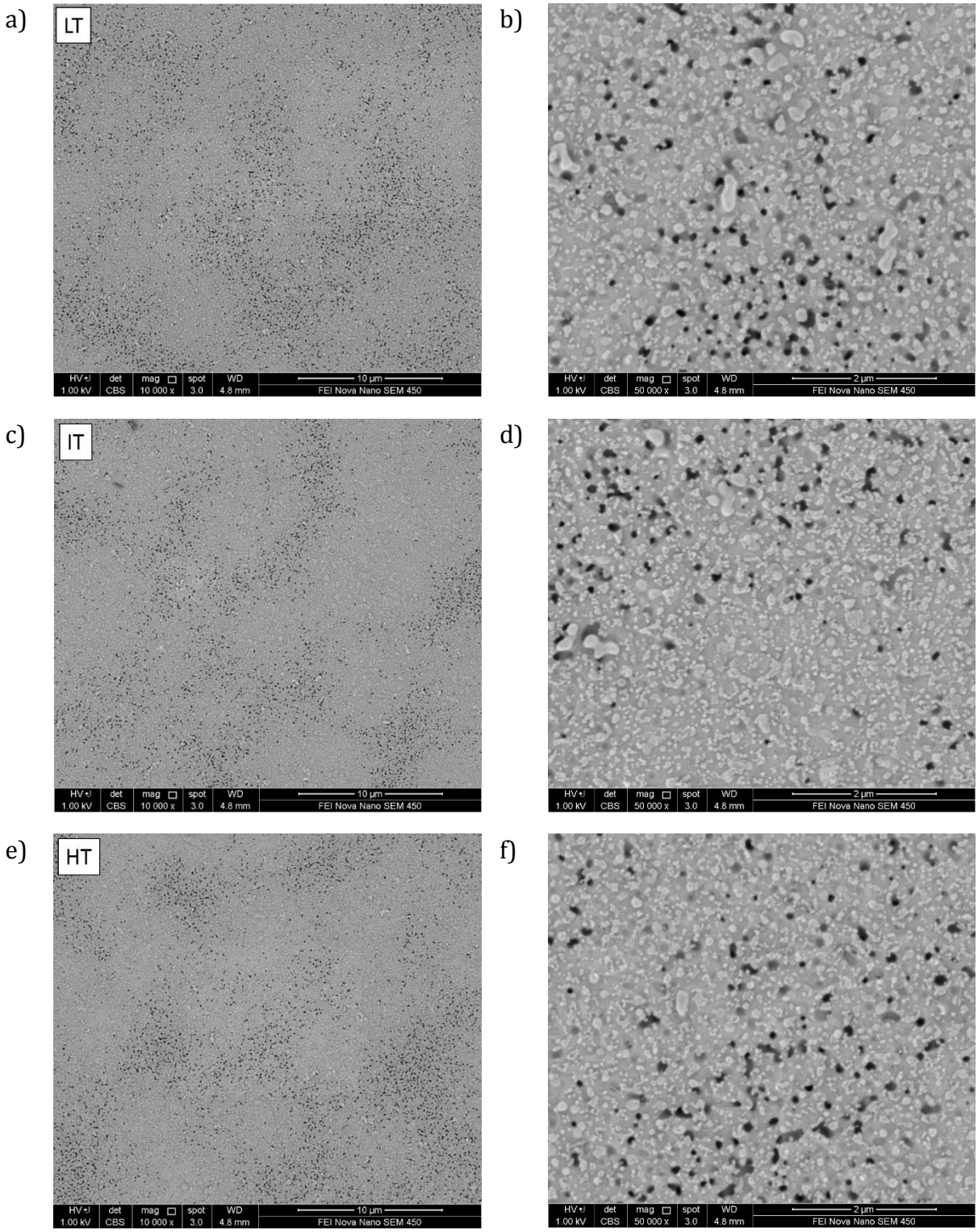

Figure 4-2: SEM micrographs of the top surface of Dy-doped YBCO thin films oxygenated at a)-b) low (LT), c)-d) intermediate (IT) and e)-f) high temperature (HT). Left: low magnification (10 µm scale bar). Right: high magnification (2 µm scale bar).

4.3 Energy dispersive spectroscopy

The EDS analysis of the Dy-doped YBCO was performed on TEM samples within the film bulk and at the interface between the film and the buffer layers. STEM-EDS was used to observe the phases formed after the oxygenation cycle and to monitor the phase changes with the oxygenation temperature.

Figure 4-3 is an example of an EDS spectrum from a Dy-doped YBCO thin film oxygenated at high temperature. The EDS peaks used for elemental mapping were: O K_α (0.52 keV), Y L_α (1.93 keV), Zr L_α (2.04 keV), Ba L_α (4.46 keV), Ce L_α (4.85 keV), Dy L_α (6.50 keV) and Cu K_α (8.04 keV). From this spectrum it is evident that it is not possible to distinguish Y from Zr when one of the elements is dominant; and that it is difficult to determine a low concentration of Ce in the presence of a strong Ba concentration.

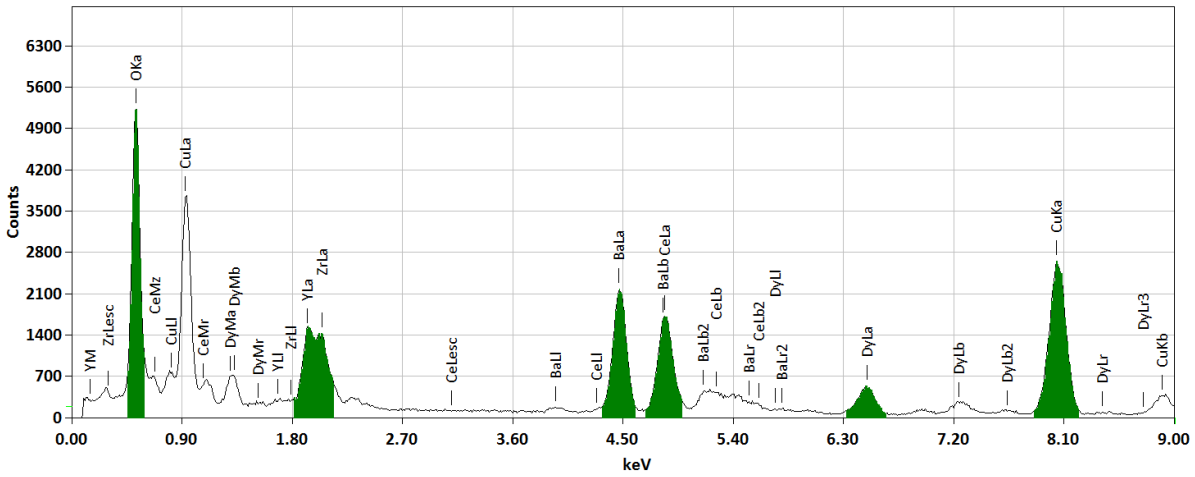

Figure 4-3: EDS spectrum of a Dy-doped YBCO thin film, with peaks used to generate elemental maps highlighted in green.

4.3.1 Sample bulk

Figure 4-4 presents the Y, Dy, Ba and Cu EDS elemental maps of the LT, IT and HT Dy-doped YBCO samples.

There is a noticeable difference in EDS mapping resolution between the three specimens due to different dwell times and map resolutions used to accommodate for sample drift. The high temperature EDS elemental map was acquired using the 300 kV FEI Titan ATEM with an EDS mapping resolution of 512 × 512 and a dwell time of 2 µs per pixel. The low temperature EDS elemental map was acquired using the 300 kV FEI Titan ATEM with an EDS mapping resolution of 256 × 256 and a dwell time of 1 µs per pixel.

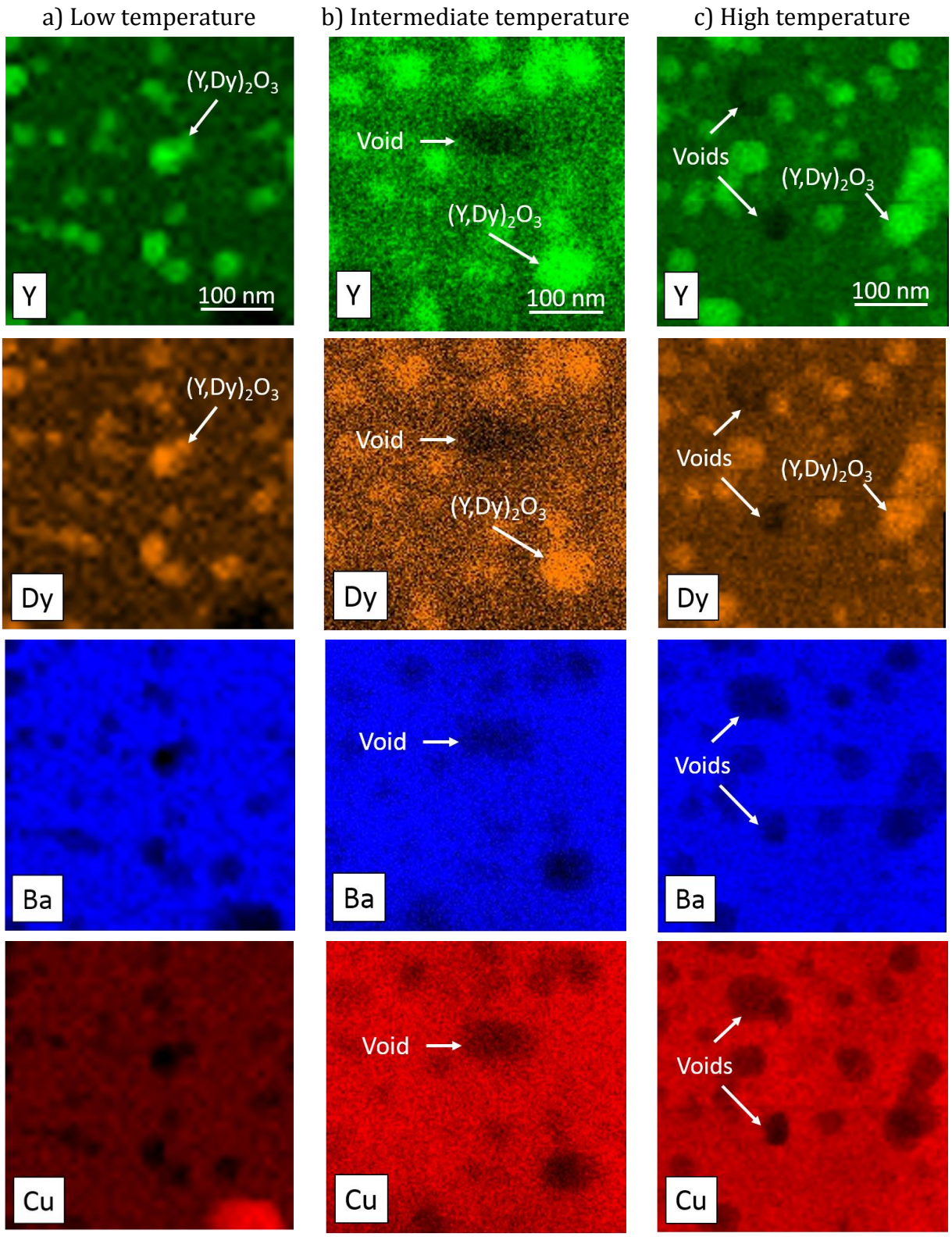

Figure 4-4: EDS elemental maps acquired in the bulk of Dy-doped YBCO thin films oxygenated at a) low, b) intermediate and c) high temperature. Y (green), Dy (orange), Ba (blue) and Cu (red). A selection of $(Y,Dy)_2O_3$ particles and voids are labelled. Scale bar shown in Y map.

The intermediate temperature EDS elemental map was acquired using the 200kV JEOL 2100F with an EDS mapping resolution of 256 × 256 and a dwell time of 2 ms per pixel. The EDS map acquired on the 2100F clearly has a lower signal to noise ratio. Despite these differences it is still possible to extract information about sample composition from these EDS maps.

The Y and Dy EDS elemental maps show an even background for the (Y,Dy)BCO bulk with periodic regions of high concentration, corresponding to low Ba and Cu concentrations, which confirms these nanoparticles are $(Y,Dy)_2O_3$. The Y L_α (1.93 kV) and Dy L_α (6.50 kV) peaks, used for EDS mapping, do not overlap and as such this correlation is not an artefact. The $(Y,Dy)_2O_3$ nanoparticles are homogeneously dispersed throughout the thin film. The low concentration regions shared between the Y, Dy, Ba and Cu maps, visible in the IT and HT samples, are voids of size ranging between 50-100 nm.

A few Cu-O particles were also observed in the three samples. One is seen as a high Cu concentration in the low temperature sample (left column). These particles are larger in size and lower in concentration than the $(Y,Dy)_2O_3$ particles.

Ortalan *et al.* [63] investigated the addition of Dy in YBCO in the form of Dy_2O_3 and also found that the Dy partially substitute Y in the YBCO structure. The co-ordination number for the Y in the YBCO is 8 therefore has an ionic radius for the trivalent atom of 1.019 Å. The trivalent Dy in the same co-ordination has an ionic radius of 1.027 Å. The small 0.8 % difference in ionic radius allows the Dy to easily incorporate into the matrix.

Finally, as opposed to the pure YBCO films, no Ba-Cu-O phase was observed in the Dy-doped films, which is explained by the reduction of phase segregation for rare-earth doped YBCO samples [4].

Here, it is shown that the 50 % addition of Dy completely compensates from the lack of Y in the pure YBCO films and completely inhibits the formation of Ba-Cu-O phases as shown by the XRD and EDS data. The absence of Ba-Cu-O phase in the Dy-doped sample therefore also explains the lower stacking fault density in the three samples after the oxygenation cycle.

4.3.2 Substrate-film interface

The Y, Dy, Ba, Cu and Ce EDS elemental maps of the Dy-doped YBCO samples at the substrate-film interface are shown in Figure 4-5. The Y and Dy EDS elemental maps present similarities to the bulk EDS maps. The (Y,Dy)BCO matrix shows an even Y and Dy background concentration with regions of higher Dy and Y concentration corresponding to the $(Y,Dy)_2O_3$ particles and to low Ba and Cu concentration.

The low temperature Cu map also shows one region with increased Cu concentration which corresponds to a Cu-O particle.

Looking at the (Y,Dy)BCO-CeO_2 interface, the low temperature Ba map shows one region with a high Ba concentration which is attributed to $BaCeO_3$. The interface regions for the intermediate temperature and high temperature sample also suggest some interaction between Ce and Ba, but these maps are less conclusive due to the energy overlap of the Ce and Ba EDS peaks.

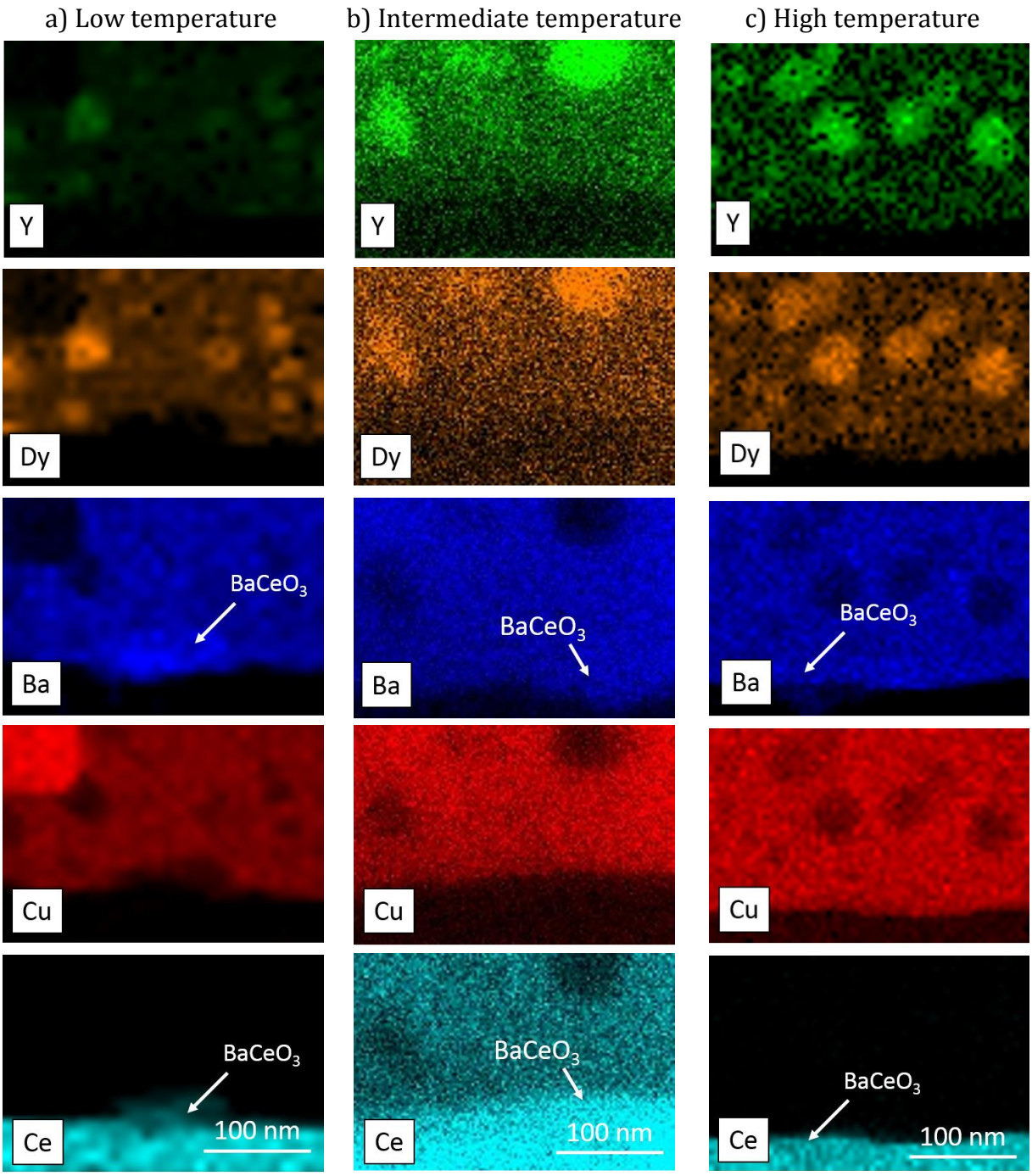

Figure 4-5: EDS elemental maps of Dy-doped YBCO thin films oxygenated at low, intermediate and high temperature. Y (green), Ba (blue), Cu (red), Dy (orange) and Ce (cyan). Scale bar shown in Ce map.

4.4 Transmission electron microscopy

TEM was used to investigate the structural differences of the Dy-doped YBCO samples when oxygenated at different temperatures and to compare the microstructures with those of the pure YBCO. High resolution scanning transmission electron microscopy (HRSTEM) was used to investigate the bulk and the stacking faults. 3D tomography was used to study the distribution of the $(Y,Dy)_2O_3$ particles and the data was correlated with EDS and STEM images.

4.4.1 $(Y,Dy)_2O_3$ particles

Figure 4-6 is a bright field STEM image of the Dy-doped YBCO sample oxygenated at low temperature, oriented with the *c*-axis in the plane of the image. The CeO_2 buffer layer and the Pt layer (lighter grey) from specimen preparation using a focused ion beam (FIB) SEM are visible at the bottom and top of the (Y,Dy)BCO layer respectively. Voids are visible in white within the matrix with a size ranging between 90-200 nm which is similar to the surface porosity observed in the SEM micrographs (Figure 4-2). The (Y,Dy)BCO layer is about 950 nm thick for the three oxygenation temperatures.

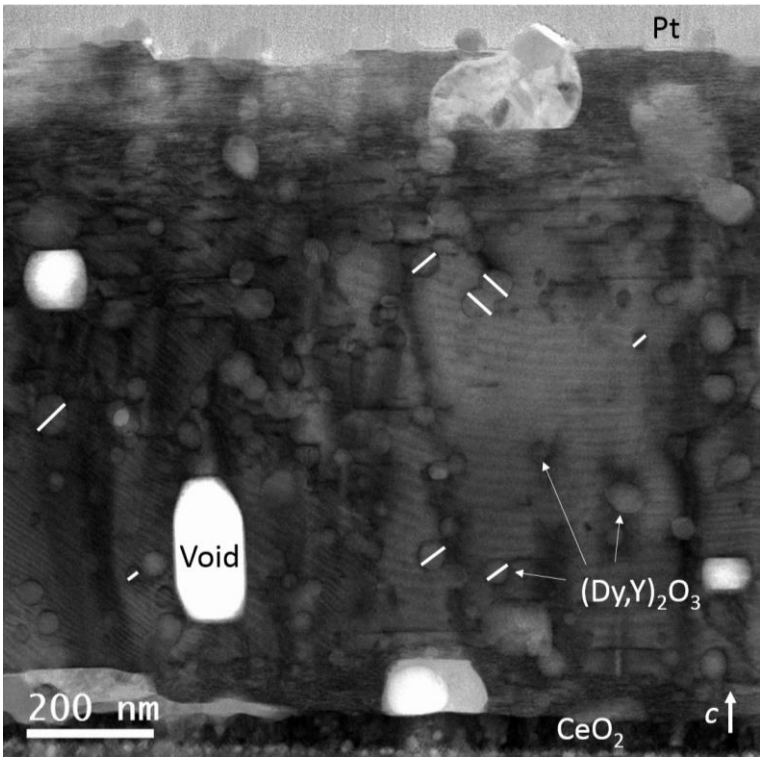

Figure 4-6: Bright field STEM micrograph of a Dy-doped YBCO sample oxygenated at low temperature, showing voids in bright and the sample in dark contrast. White lines are examples of $(Y,Dy)_2O_3$ particles measured.

The size of the $(Y,Dy)_2O_3$ particles were measured with ImageJ and range between 15-70 nm, 20-65 nm and 15-65 nm for the LT, IT and HT samples respectively. The three Dy-doped YBCO samples therefore contain particles of similar sizes, showing that the oxygenation temperature does not affect the size of the $(Y,Dy)_2O_3$. This is in contrast to the pure YBCO sample that exhibit Y_2O_3 particles that vary in size with oxygenation temperature. The measured porosity and $(Y,Dy)_2O_3$ particle size is in agreement with the SEM image analysis (Figure 4-2).

Figure 4-7 presents high resolution transmission electron microscope (HRTEM) micrographs of the Dy-doped thin films oxygenated at low (a), intermediate (b) and high (c) temperature oriented in [100]/[010] direction with their corresponding selected area diffraction (SAD) patterns inset. As opposed to the YBCO samples presented in Chapter 3, the three SAD patterns present sharp reflections, with no streaking in the (00*l*) direction, confirming the low stacking fault density in the three Dy-doped samples.

The high resolution images in Figure 4-7 show incoherent $(Y,Dy)_2O_3$ particles in the thin films matrix at all oxygenation temperatures. The particles visible in the micrographs range from 15-30 nm in size.

Figure 4-7a shows an incoherent $(Y,Dy)_2O_3$ particle in the LT sample. The flat interfaces between the particle and the matrix at the bottom and top suggest semi-coherency between the particle and the matrix in the *c* direction. Figure 4-7b show an incoherent $(Y,Dy)_2O_3$ particles in IT sample. The top right bright area corresponds to the vacuum at the edge of the specimen. Lattice fringes are visible in the $(Y,Dy)_2O_3$ particle, however these are not oriented with the parent (Y,Dy)BCO matrix. Finally, Figure 4-7c shows an incoherent nanoparticle in the HT sample. The top left corner of the image is clearly oriented in the zone axis, but the bottom right presents a change in the lattice fringes visibility suggesting a change in the orientation of the structure along the *ab* plane or a change in the specimen thickness.

The particle incoherency with the matrix is in agreement with the XRD data where most of the peaks of Y_2O_3/$(Y,Dy)_2O_3$ are observed (Figure 4-1), confirming randomly oriented nanoparticles.

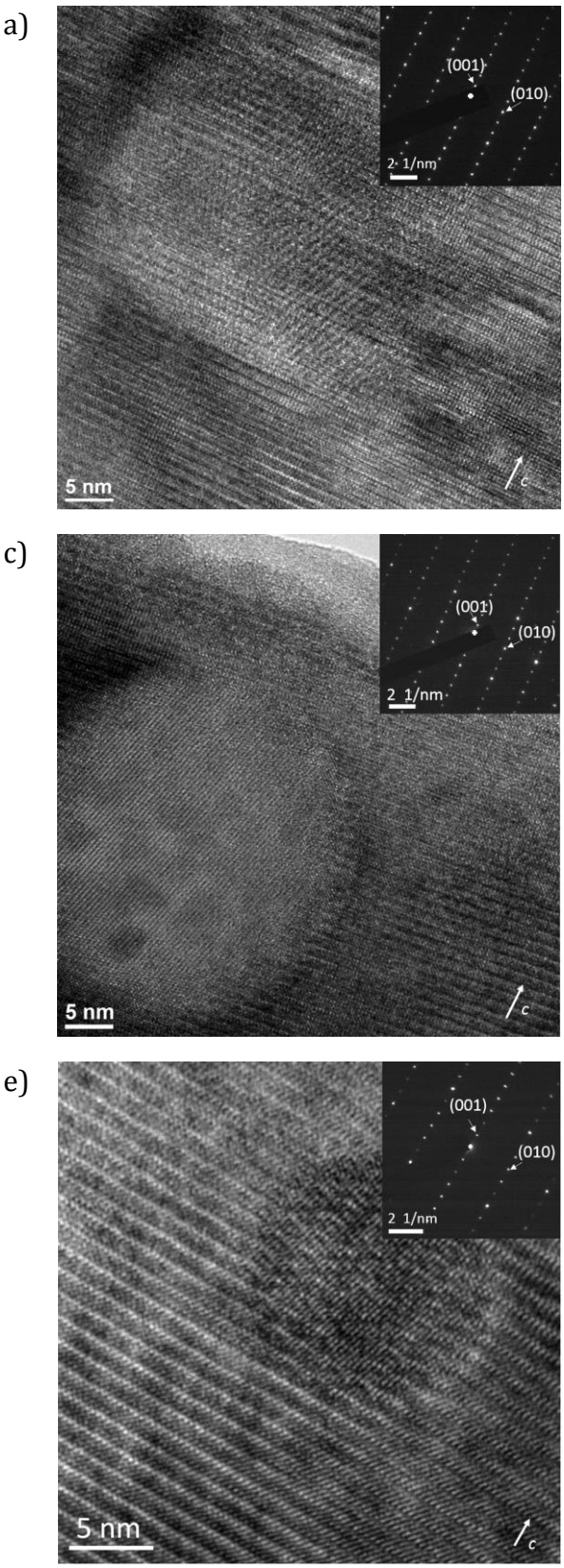

Figure 4-7: HRTEM micrographs of Dy-doped YBCO thin films oxygenated at a) low, b) intermediate and c) high temperature, highlighting the $(Y,Dy)_2O_3$ particles embedded in the matrix. Inset each image is the corresponding selected area diffraction pattern.

4.4.2 Sample bulk structure

Figure 4-8 presents representative HRTEM micrographs of the Dy-doped YBCO thin film oriented in the [010]/[100] direction with their corresponding SAD patterns inset.

The HRTEM micrograph of the LT sample (Figure 4-8a) shows a relatively well ordered (Y,Dy)BCO matrix. A dark band divides the micrograph and represents a region where the (Y,Dy)BCO is oriented slightly off the zone-axis in comparison to the surrounding regions. In the bottom right-hand corner of the micrograph there is a region which only displays strong *ab* planes suggesting a misalignment in the *c*-axis. This is confirmed by the inset SAD pattern which shows bright (*h*00) reflections.

The HRTEM micrograph of the IT sample (Figure 4-8b) shows regions of well-ordered (Y,Dy)BCO (white square). This well-structured region is located between two extended defects (indicated by two white arrows), where the YBCO structure is less well defined. These extended defects are accompanied by darker regions indicating straining/misorientation in the surrounding regions.

The HT sample in Figure 4-8 shows two orientations in the structure. The top right region is well oriented down the zone axis, while the bottom left region does not have clear lattice fringes suggesting a misorientation. The interface between these two regions is indicated with two black arrows and exhibits a large structural defect.

High magnification high angle annular dark field (HAADF) micrographs were acquired in the thin films matrix to compare defect free areas. As explained in Chapter 1, in HAADF micrographs, the contrast predominantly originates from atomic numbers variation and as such, atoms appear bright on a dark background and the heavier elements are brighter. Figure 4-9 shows the HAADF micrographs in the [010]/[100] direction of the bulk of the LT, IT and HT Dy-doped samples. The Y/Dy (green), Ba (blue) and Cu (red) atoms are superimposed on the micrographs, and the rows of CuO chains, Y/Dy and BaO are clearly visible showing a perfectly stacked (Y,Dy)BCO structure.

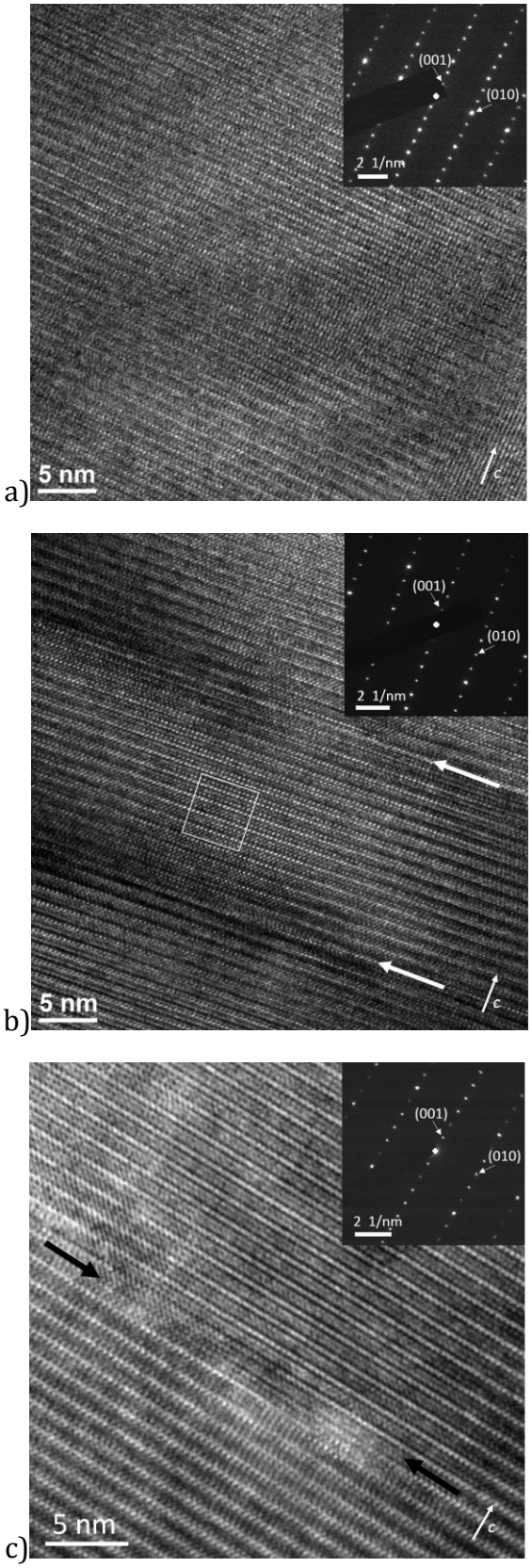

Figure 4-8: HRTEM micrographs of Dy-doped YBCO thin film oxygenated a) low, b) intermediate and c) high temperature. Inset are the corresponding SAD patterns oriented in the [010]/[100] zone axis.

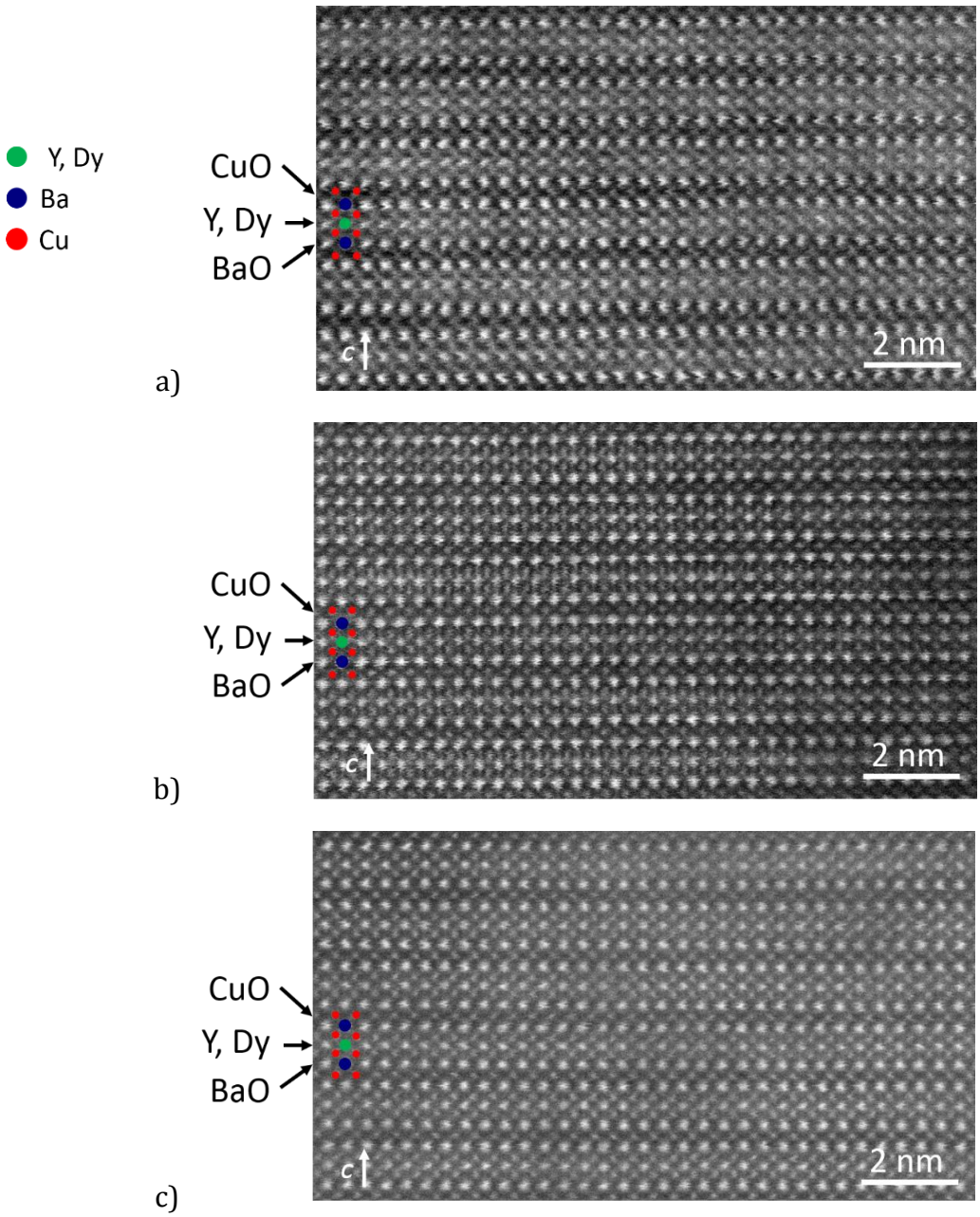

Figure 4-9: HAADF HRSTEM micrographs of bulk Dy-doped YBCO thin films oxygenated at a) low, b) intermediate and c) high temperature. The atomic arrangement of the (Y,Dy)BCO is superimposed on each micrograph.

The nature of each row of atoms was ensured by comparing the intensity profiles of the acquired images with simulated HAADF images of pure $YBa_2Cu_3O_7$ (Y123) and pure $DyBa_2Cu_3O_7$ (Dy123) using the Java electron microscopy software (JEMS) [43]. The two simulated images were made for the same conditions (specimen thickness and using a FEI Titan operated at 300 kV). Figure 4-10 shows the simulated HAADF images of pure Dy123 and pure Y123, as well as an enlarged area of Figure 4-9c corresponding to a Dy-doped YBCO oxygenated at high temperature. The corresponding atoms, Y, Dy, Ba and Cu are labelled on each image. The intensity profiles in the *c* direction (corresponding to the lines between the black arrows) are plotted in Figure 4-11. The intensities were normalised to the Ba for comparison. As expected, the simulations show the Dy with the highest intensity (heaviest element with Z = 66), then Ba (Z = 56) and Y (Z = 39). The acquired image (blue line) shows variation of intensities even for the Ba, which is likely due to surface inhomogeneity. However, despite the variation, the Ba columns are consistently more intense than the Re (Y/Dy), confirming that the matrix has a mixture of Y and Dy.

Finally the line profile of the acquired image shows that the *c*-axis spacing of the sample is about 1.230 nm, which is larger than the theoretical *d*-spacing of the pure Y123 and pure Dy123. This value is also larger than the XRD results (1.189 nm) but is within the 3.1 % error calculated in Chapter 2 (section 1.3.6).

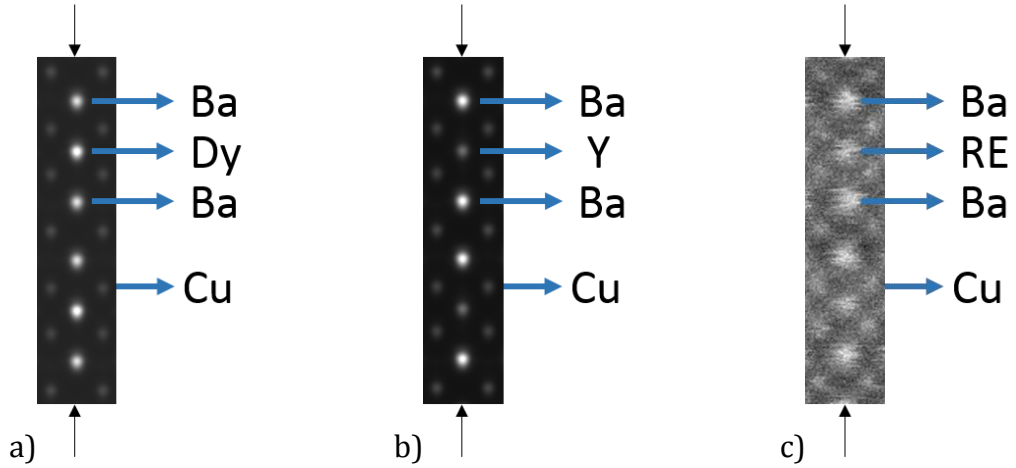

Figure 4-10: Comparison of atomic column intensities from acquired and simulated HAADF HRSTEM images: a) simulated pure Dy123, b) simulated pure Y123 and c) acquired image (enlarged from Figure 4-9c).

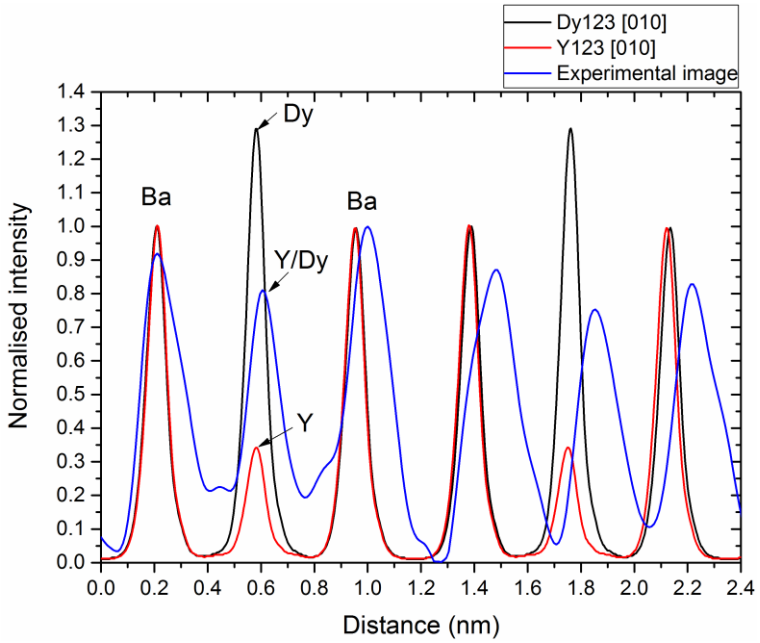

Figure 4-11: Normalised intensity profile of the Re-Ba column along the *c*-axis of simulated intensity of pure Dy123 (black), simulated HRSTEM image of pure Y123 (red) and experimental micrograph (blue) corresponding to Figure 4-10 a), b) and c) respectively.

4.4.3 Stacking faults

Figure 4-12 shows a series of representative bright field STEM micrographs in the bulk of Dy-doped YBCO thin films oriented in the [010]/[100] direction.

Regions of the sample in each of the STEM micrographs are seen to exhibit darker and brighter contrast. The darker regions arise from nanoparticle inclusions ($(Y,Dy)_2O_3$) which will scatter the beam due to the different diffraction conditions and atomic composition.

Other noticeable features in the STEM micrographs are the darker lines running across the images that are identified as stacking faults. The LT sample exhibits a low concentration of stacking faults. At this magnification the remaining (Y,Dy)BCO appears to have the standard (Y,Dy)BCO structure. Considering the fast Fourier transform (FFT) for the low temperature sample, the (00*l*) reflections are sharp confirming a low concentration of extended stacking faults. The IT sample (Figure 4-12b) presents more stacking faults that run through the image. Looking at the FFT, the (00*l*) reflections show an increased streaking in the [*00l*] direction confirming an increased stacking fault density. The other noticeable feature in this micrograph is the distinct mottled appearance however, this is attributed to a sample artefact and not a (Y,Dy)BCO defect. Finally, the HT sample exhibits extended stacking faults running across the entire image suggesting that not only a higher stacking faults density, but also that the stacking faults are larger. Looking at the FFT, the (00*l*) reflections also show streaking in the [*00l*] direction confirming the high concentration of the stacking faults.

These micrographs confirmed that as the oxygenation temperature increases, the stacking fault density and length increase.

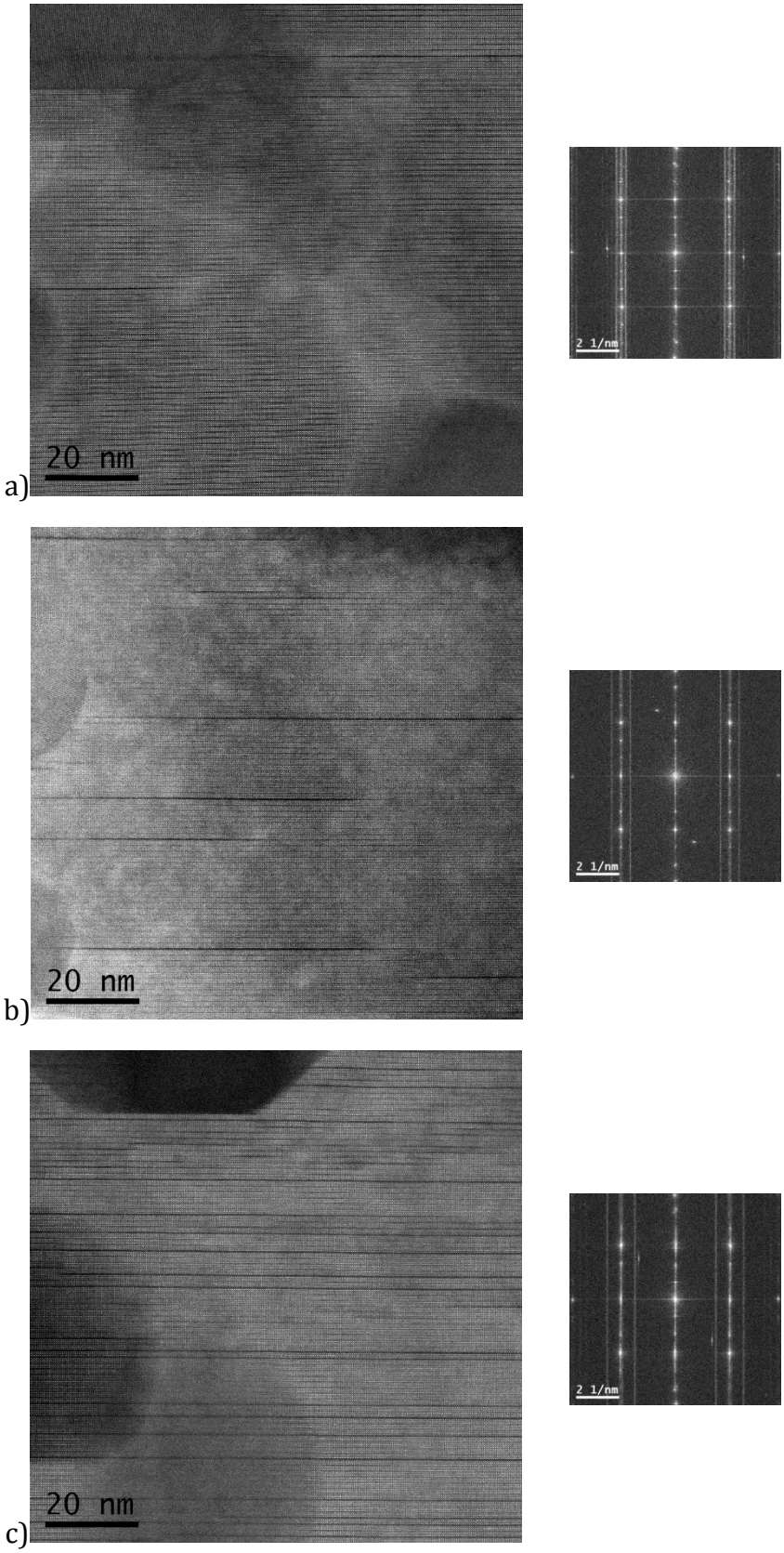

Figure 4-12: HAADF STEM micrographs and the corresponding FFT of Dy-doped YBCO thin films oxygenated at a) low, b) intermediate and c) high temperature, showing an increasing presence of stacking faults.

Representative high magnification HAADF STEM images of individual stacking faults observed in the LT, IT and HT samples are presented in Figure 4-13. Once again, the stacking in the *c* direction is well ordered.

The HAADF micrograph of the LT sample (Figure 4-13a) shows two stacking faults. The first one, on the left hand side, present the CuO plane stacked in a triangle-shape and the second one, located between the dashed arrows, is short and exhibits a square-shape stacking which is representative of projections down the [100] and [010] directions respectively [70]. The HAADF micrograph of the IT sample (Figure 4-13b) shows the end of one stacking faults with the triangular shape corresponding to the [100] direction. The HT sample micrograph (Figure 4-13c) shows two stacking faults: one on the left hand side oriented in the [100] direction and one on the right hand side oriented in the [010] direction. As it was previously observed in Chapter 3 in the pure YBCO samples, the (Y,Dy)BCO structure periodically switches from the [010] to the [100] direction.

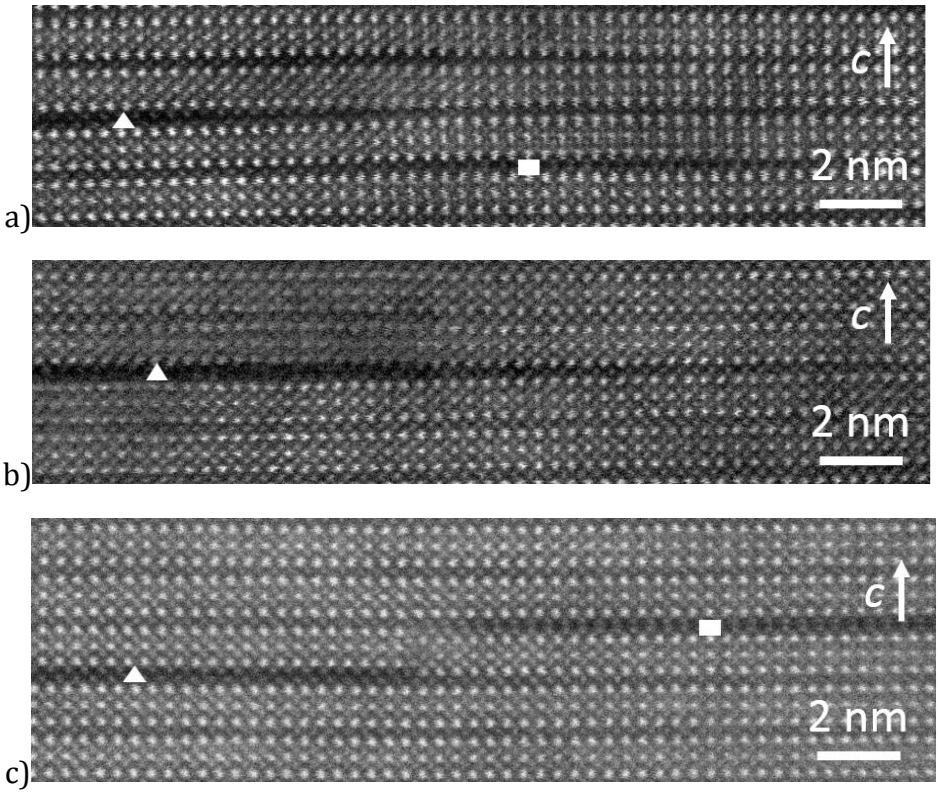

Figure 4-13: High resolution HAADF STEM micrographs of Dy-doped YBCO thin films oxygenated at a) low, b) intermediate and c) high temperature.

4.4.4 Induced strain

The previous section highlighted the presence of stacking faults in the samples. It would be anticipated that such faults generate lattice distortion in the parent (Y,Dy)BCO matrix. Low magnification HRSTEM bright field images of the same samples are shown in Figure 4-14, showing $(Y,Dy)_2O_3$ nanoparticles and stacking faults in the (Y,Dy)BCO matrix. The micrographs were acquired using the bright field detector, which collects the electrons directly transmitted. Therefore the dark areas correspond to electrons that were scattered away from the directly transmitted beam and were attributed to lattice distortions (strain). For the three different oxygenation temperatures, the particles generate strain, visible as a darker contrast that is 2-3 nm thick all around the particles into the matrix. Due to the random orientation, and the incoherent interface of the particles, seen in Figure 4-7, it is not surprising that strain is induced into the surrounding matrix.

In addition to the nanoparticles, the stacking faults also induce strain in the surrounding matrix as observed in Figure 4-7a and c. Extended strain is especially visible at the end of the stacking faults, up to 4 nm into the matrix, on each side of the fault. It is however remarkable that the strain is only extended to a few nanometres for both the stacking faults and the nanoparticles, and that the (Y,Dy)BCO matrix remains unstrained and epitaxial on a longer range.

$(Y,Dy)_2O_3$ nanoparticles have been previously observed in Dy-doped YBCO thin films with a size ranging between 10-50 nm [11, 61], which is similar to the observations (15-65 nm, compared to the pure YBCO samples with 30-130 nm for the low and intermediate oxygenation samples). Similar to the Y_2O_3 nanoparticles in pure YBCO films, these $(Y,Dy)_2O_3$ particles form during the decomposition stage (i.e. before YBCO growth) [4] and as such are incoherent with the surrounding YBCO matrix. Nonetheless, the incoherency of the $(Y,Dy)_2O_3$ only creates short range strain and the overall epitaxial growth of the YBCO matrix is not affected.

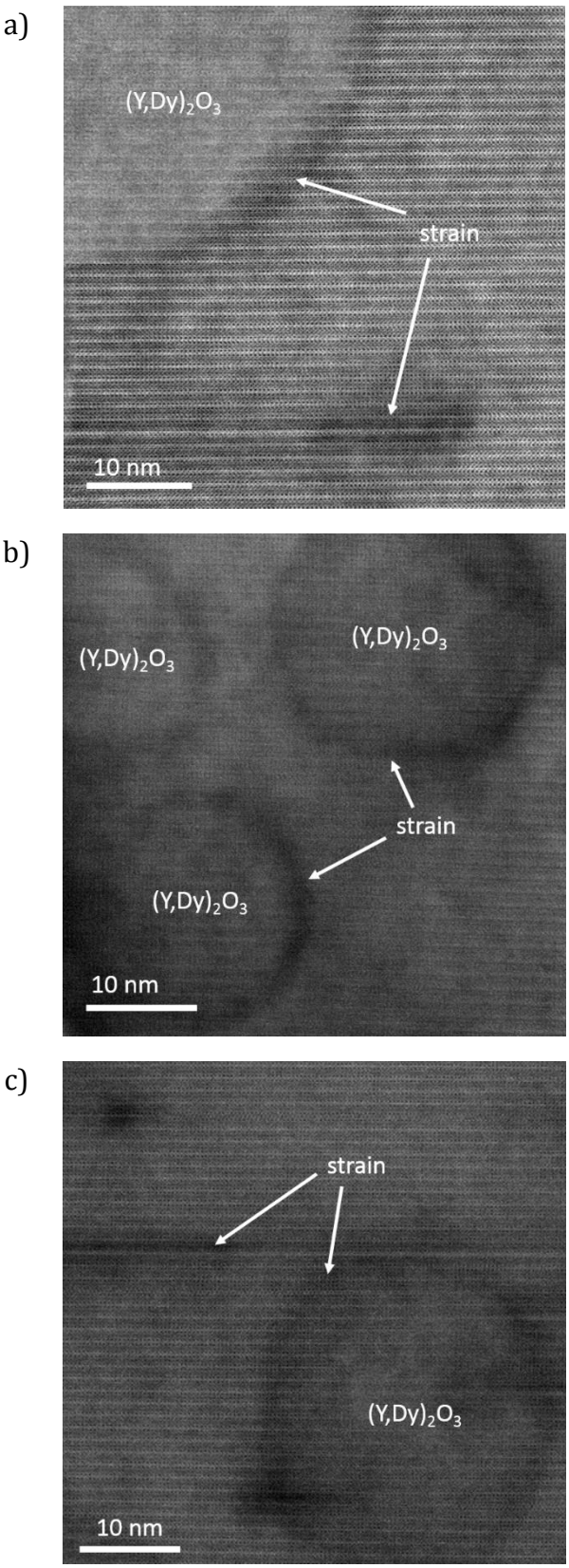

Figure 4-14: HRSTEM bright field images of the Dy-doped thin films oxygenated at a) low, b) intermediate and c) high temperature, highlighting the strain in the matrix around the $(Y,Dy)_2O_3$ particles and at the end of stacking faults.

4.4.5 $(Y,Dy)_2O_3$ nanoparticle distribution

Although particles can be imaged with EDS elemental mapping, conventional TEM and STEM, these techniques only provide two dimensional information. Some particle clusters may appear as an individual particle in EDS elemental mapping while not all particles are visible in a single TEM/STEM micrograph due to scattering and diffraction conditions. 3D electron tomography provides three dimensional information about the particle and void distribution within the film. This section compares and contrasts the information provided by the EDS elemental maps with the 3D tomogram for the high temperature oxygenated (Y,Dy)BCO sample to provide a deeper understanding of $(Y,Dy)_2O_3$ particle size and distribution.

A 3D electron tomogram is generated through a series of steps. First a series of STEM images is acquired for different specimen tilt angles. Second, the images from the tilt series are aligned along the tilt axis to adjust the specimen position. Third the tilt series is reconstructed in an *x*, *y* and *z* volume. Finally, the elements of interest (here $(Y,Dy)_2O_3$ particles) are generated in the 3D volume by the segmentation step. The relevant details of each step mentioned above were given in Chapter 2 (Section 1.4.3).

Figure 4-15 shows representative bright field STEM images of the tilt series recorded at different tilt angles: 4° (a), 16° (b), 30° (c) and 44° (d). The *c* direction is indicated in image a), and the CeO_2 buffer layer is visible at the bottom of the images. The cross in the middle of the images highlights the small shift in position of the sample as it is tilted, as indicated by the movement of the nearby void. The arrows show particles that are visible at certain tilt angles but not at others. The top arrow for example shows a particle in image a), which is not visible in the other images. The bottom arrow shows a particle in image b), invisible at other tilt angles.

In addition, these images present an inconsistency in the contrast due to the change in diffraction conditions between the images in the tilt series. The bottom half of images a) and b) is dark with bright particles and white with dark particles respectively. This leads to challenges in the data set reconstruction and segmentation because the use of a simple threshold is not possible to locate the same particles between images.

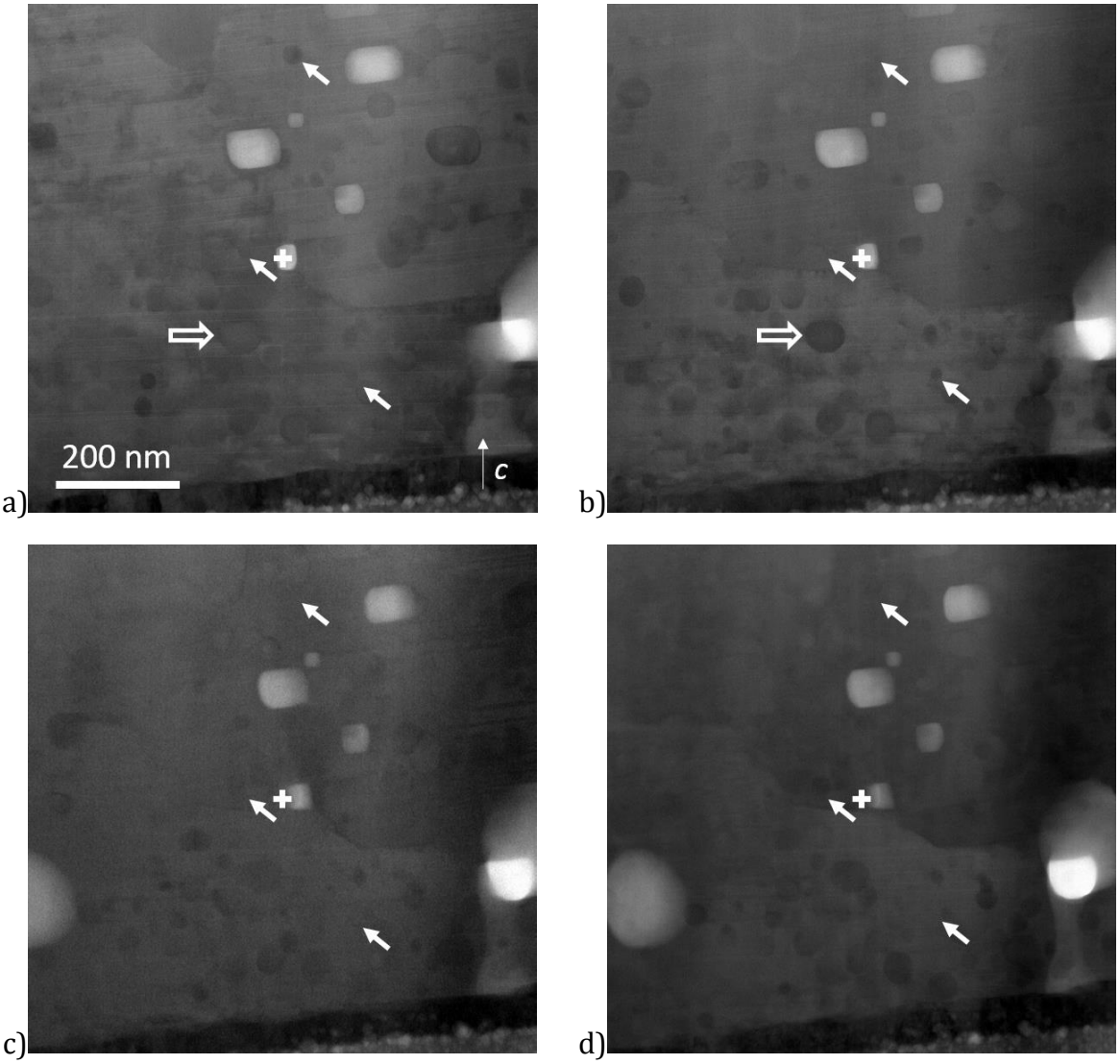

Figure 4-15: Bright field STEM images of the high oxygenation temperature Dy-doped YBCO sample from the tilt series at different α tilt angles: a) 4°, b) 16°, c) 30° and d) 44°. The arrows indicate the same particles whose visibility changes for different tilt angle.

Figure 4-16 shows a 3D segmentation of the $(Y,Dy)_2O_3$ particles in a thin film oxygenated at high temperature. The *c*-axis direction is along the bottom axis (red), and the CeO_2 buffer layer is the green axis. The blue and purple volumes correspond to voids and $(Y,Dy)_2O_3$ particles respectively.

It would be interesting to understand the 3D particle shape, however it is not possible due to the manual segmentation process. An automatic thresholding was not possible due to the large changes in contrast between images, as explained from Figure 4-15, leading to the double cone particle shape. This particle shape also impacts on the volume size and

therefore no conclusions were drawn in regards to the particle volume sizes from the tomography data.

This 3D segmentation shows that the $(Y,Dy)_2O_3$ particles are uniformly distributed along the film growth and within the film bulk. However, this 3D reconstruction is not appropriate for particle sizing and shape analysis.

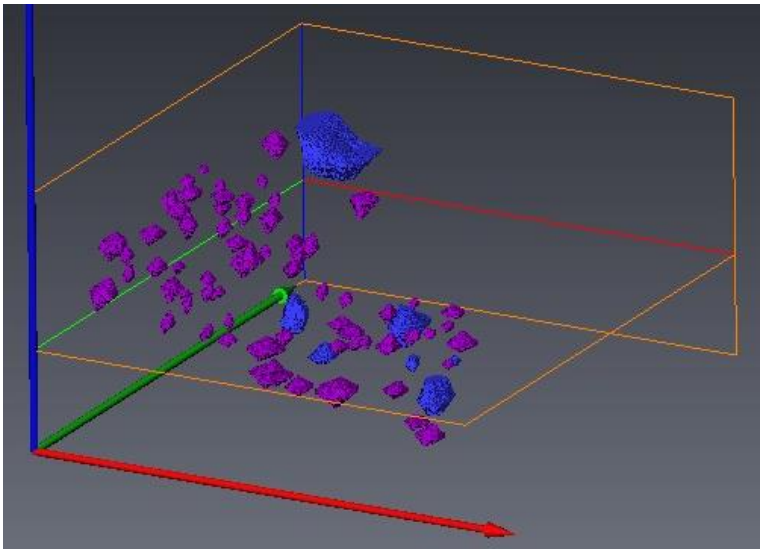

Figure 4-16: 3D segmentation of the $(Y,Dy)_2O_3$ particles (purple) and voids (blue) distributed in the (Y,Dy)BCO thin film oxygenated at high temperature. The bottom axis (red) corresponds to the film *c*-axis.

The 3D segmentation was compared to the EDS data and a bright field STEM image (Figure 4-17). Figure 4-17 presents a dark field STEM image, an EDS Y elemental map and the 3D segmentation of the Dy-doped YBCO specimen oxygenated at high temperature. The white rectangle in the STEM image corresponds to the EDS map and 3D segmentation region and includes a small fraction of the buffer layer at the bottom where no Y is visible in the elemental map. Three arrows highlight the voids present in the specimen. Seven of the $(Y,Dy)_2O_3$ particles are numbered to guide the eye and correspond to the same particles in each data set. Particles No.3 and No.4 are particularly interesting because they are easily distinguishable in the STEM micrograph but appear as a single large particle in the EDS map, while the 3D tomography reveals that there are four particles in the area.

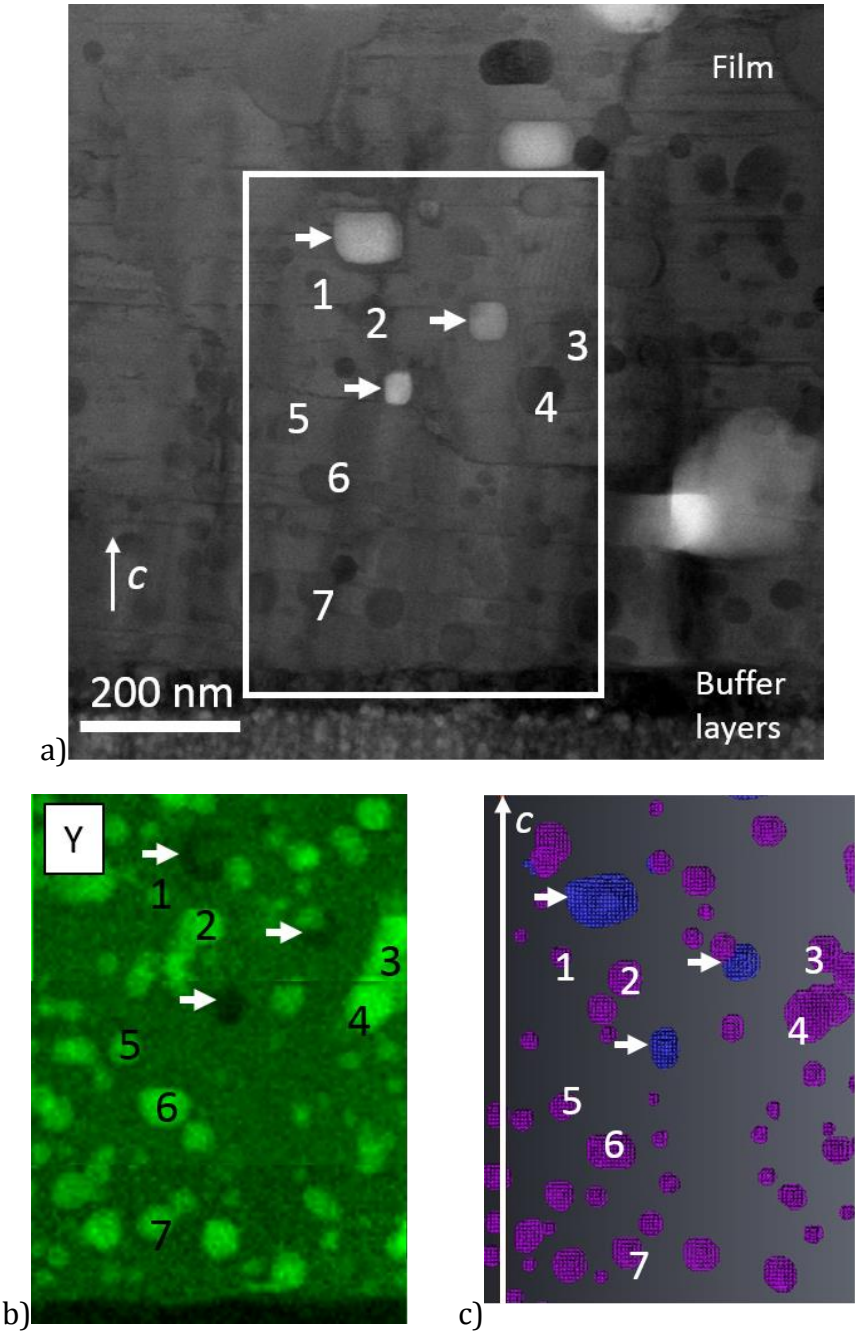

Figure 4-17: Data set comparison of $(Y,Dy)_2O_3$ particle distribution between: a) bright field STEM micrograph, b) Y EDS map and c) 3D tomography segmentation. Seven particles are numbered to guide the eye. The arrows indicate the same voids in each data set. Scale bar in a).

This demonstrates that the 3D segmentation was successful and is representative of the sample as it matches both the STEM image and the EDS data.

The STEM images are useful for particle sizing, however they do not show all of the particles present in the thin films. The EDS data allows to visualise all of the particles with the Y and Dy elemental maps. However those maps need to be interpreted carefully as they do not separate multiple particles that are close to each other as several small particles appear as a single bigger particles (No. 3-4 in Figure 4-17). The tomography data presents the particle distribution in 3D, allowing separation of multiple particles that are indistinguishable in the EDS mapping or STEM imaging. It is possible to use the EDS data to consider the distribution of the particles along the film growth.

4.5 Microstructure summary of the Dy-doped films

The Dy-doped YBCO thin films were successfully epitaxially grown on the textured RABiTS substrate using TFA-MOD deposition. The following microstructural observations were made:

1. The *c*-axis lattice parameter is approximately 1.173 nm and does not change with oxygenation temperature.
2. The *a*-axis lattice parameter decreases slightly and the *b*-axis lattice parameter increases slightly with increasing oxygenation temperature, showing that the degree of orthorhombicity decreases with increasing oxygenation temperature.
3. The film's texturing is independent of oxygenation temperature with the c-axis misorientation and the ab in-plane misorientation being 3.1° and 5.1° respectively.
4. The porosity is inhomogeneously distributed with denser areas of approximately 35 µm, surrounded by more porous regions. The porosity size is about 90-200 nm and represents 2 % of the surface. Those observation are independent of the oxygenation temperature.
5. The (Y,Dy)BCO bulk presents the known Y123 structure with the Dy partially substituting in the Y site.
6. The Dy also partially substitutes the Y in the Y_2O_3 nanoparticles. The $(Y,Dy)_2O_3$ nanoparticles are approximately 10-60 nm in size, they grow homogeneously dispersed through the film and are predominately incoherent with the parent (Y,Dy)BCO matrix. All these factors show no dependence on oxygenation temperature.

7. No Ba-Cu-O phase is observed and only a few Cu-O particles are present with a maximum size of approximately 500 nm at the surface.
8. The stacking fault density, increases with increasing oxygenation temperature (from 6 % to 12 %)
9. The stacking fault length increases with increasing oxygenation temperature
10. Both the stacking faults and the incoherent particles generate localised strain in the (Y,Dy)BCO matrix.

The excess Dy in the Dy-doped YBCO samples suppresses Ba-Cu-O formation in the reaction stage. However, the Cu-O phase still forms and is observed after sample oxygenation. The reduction in these Cu-rich phases removes the primary source of the Cu-O for stacking fault formation during the oxygenation stage. Accordingly, the stacking fault density is considerably lower in the Dy-doped YBCO samples and shows a weaker oxygenation temperature dependence than for the YBCO samples. The reduction in the *a*-axis lattice parameter and the increasing *b*-axis lattice parameter are concomitant with the increasing stacking fault concentration.

4.6 Critical current

Similarly to the pure YBCO samples presented in Chapter 3, the critical current at self-field and under 1 T applied magnetic field of the Dy-doped YBCO samples are presented. The vortex pinning behaviour was also studied by normalising the I_c data at 1 T with the self-field I_c. For each section, the Dy-doped samples are also compared to the pure YBCO samples from Chapter 3.

4.6.1 Self-field critical current

The self-field I_c as a function of operating temperature for the Dy-doped YBCO thin films is presented in Figure 4-18. The Dy-doped samples exhibit broadly similar behaviour to the pure YBCO samples. The self-field I_c decreases with increasing measurement temperature, reaching zero as the temperature approaches T_c (88 K). This value is slightly higher than T_c of the pure YBCO samples (87 K, Chapter 3) but still confirms the similar oxygen content in the samples [136, 137]. The samples carry a considerably higher current at low measurement temperature (> 1300 A/cm at 30 K) than at higher temperature (~ 230 A/cm at 77 K). For operating temperatures higher than 60 K, the three thin films present a similar self-field I_c. However, at lower temperatures, the I_c of

the different films diverge to reach 1820 A/cm, 1580 A/cm and 1390 A/cm for the LT, IT and HT samples respectively at 30 K.

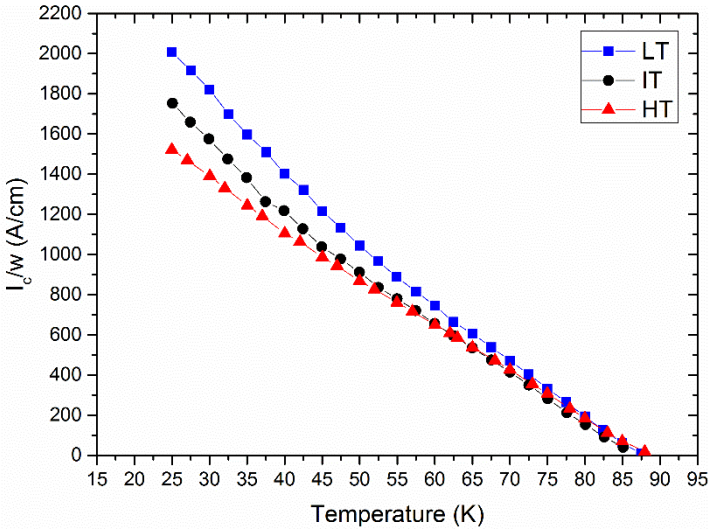

Figure 4-18: Self-field critical current as a function of temperature of Dy-doped YBCO thin films oxygenated at low (blue), intermediate (black) and high (red) temperature.

4.6.1.1 Comparison with pure YBCO

The self-field I_c at 77 K of the Dy-doped samples reaches value of 210-270 A/cm which is approximately 70 % higher compared to the pure YBCO (for the LT samples).

The addition of excess Dy in the sample hinders the formation of the non-superconducting Ba-Cu-O phase and halves the porosity of the films compared to pure YBCO samples. Both these microstructural features block the current path through the film, reducing I_c [142]. Efforts have been conducted to reduce the porosity that appears during the decomposition and reaction stages [33, 143]. In this work, with Dy addition, the film is densified and the maximum pore size is significantly reduced. Although the oxygenation cycle contributes to the film's densification, the observed porosity is independent of the oxygenation temperature in the present study. The Dy-doped YBCO films' densification and the reduced non-superconducting phase concentration (created by the Dy addition) are therefore a source of the critical current improvement compared to the YBCO films.

In addition, similarly to the pure YBCO samples, the same trend of self-field I_c decreasing with increasing oxygenation temperature is observed. As for the pure YBCO samples, the film texturing and the porosity being a factor of decreasing I_c is dismissed. The Dy-doped samples present the same values of *c*-axis and *ab* plane misorientation (3.1° and 5.1°

respectively) and porosity (~2 %) for the different oxygenation temperatures. The stacking fault density, however, was observed to increase with increasing oxygenation temperature, even though the density reaches lower values for the Dy-doped samples (up to 12 %) than the pure YBCO samples (up to 36 %). This confirms that the increase of Y124-like stacking fault defects with increasing oxygenation temperature in the sample is detrimental to the self-field I_c of the films.

4.6.2 Critical current under 1 T magnetic field

Figure 4-19 shows the critical current as a function of the applied magnetic field angle measured at 77 K and 30 K, under 1 T applied magnetic field, of the Dy-doped YBCO samples. At 77 K, the samples present a similar isotropic component of the critical current of 40-50 A/cm. However the 90° peak value increases with increasing oxygenation temperature with a maximum I_c of 57 A/cm, 70 A/cm and 115 A/cm for the LT, IT and HT samples respectively. At 30 K, and at all applied magnetic field angles, the critical current is higher for the films oxygenated at lower temperatures.

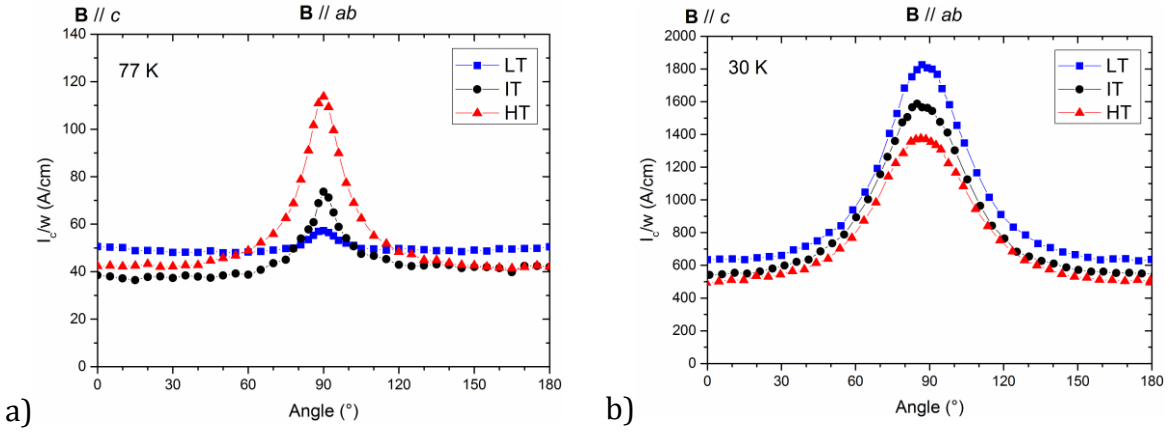

Figure 4-19: Critical current as a function of the applied magnetic field angle measured at a) 77 K and b) 30 K of Dy-doped YBCO thin films oxygenated at low (blue), intermediate (black) and high (red) temperature.

4.6.2.1 Comparison with pure YBCO

The microstructural analysis has shown that the stacking fault density increases with oxygenation temperature for both the (Y,Dy)BCO and YBCO thin films; the density increase being more prominent in the YBCO thin films. Figure 4-20 shows the isotropic and anisotropic critical currents plotted as a function of the stacking fault density for both type of samples at 77 K and 30 K. The value used were for an applied magnetic field at 0° (B // c-axis) and 90° (B // ab plane) which are representative for the isotropic and the

anisotropic I_c respectively. It highlights that a 30 K, both isotropic and anisotropic I_c decrease with increasing stacking fault density. The successful reduction of stacking fault density by Dy addition contributes to an increase of the critical current. The same effect is observed for the isotropic I_c at 77 K, but is less pronounced.

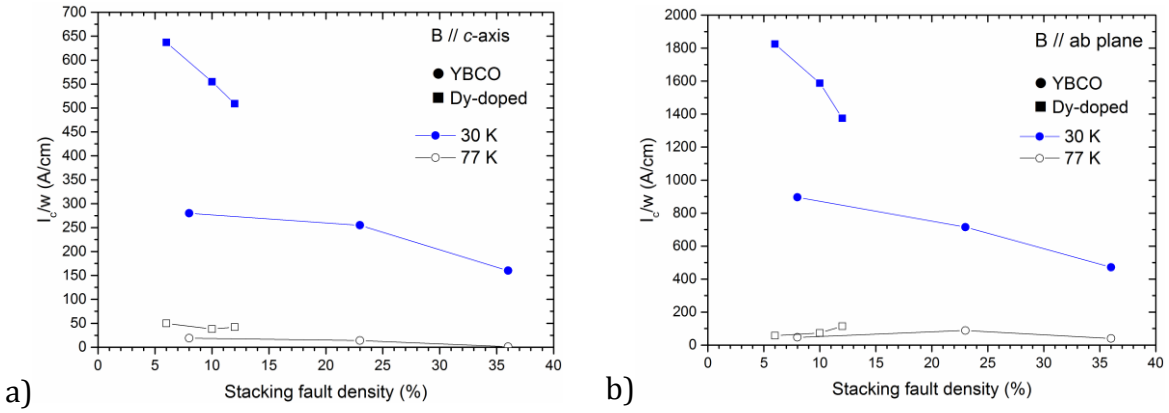

Figure 4-20: Critical current as a function of the stacking fault density of pure YBCO films (●) and Dy-doped YBCO films (■) at 30 K (filled blue symbols) and 77 K (hollow symbols). a) Isotropic I_c (*B* // *c*-axis) and b) anisotropic I_c (*B* // *ab* plane).

4.6.3 Vortex pinning under 1 T magnetic field

Similarly to the pure YBCO critical current analysis, the pinning characteristic of the thin films was studied by normalising the I_c data (from Figure 4-19) to the self-field I_c (from Figure 4-18) at the corresponding measured temperature for each thin film. Figure 4-21 shows the normalised I_c plots at 77 K and 30 K.

At 77 K (Figure 4-21a) the samples exhibit the same isotropic pinning showing that the microstructure of the samples contributes to vortex pinning in a similar way. This is attributed to the $(Y,Dy)_2O_3$ nanoparticles that are present in a similar sized range and homogeneously distributed for the three oxygenation temperatures. In contrast, the pinning at 90° is stronger for higher oxygenation temperatures. This highlights again the increasing density of stacking faults that enhances the vortex pinning in the *ab* plane. The peak is almost non-existent in the LT sample which has a low stacking faults density (6 %, Table 4-1).

At 30 K (Figure 4-21b) the normalised I_c is independent of oxygenation temperature at all applied magnetic field angles. This shows that the differences in the pinning occurring in the thin films at 30 K remains unchanged for different oxygenation temperatures, and

is only due to intrinsic pinning [39], and that the stacking faults density variation does not affect the pinning at 30 K, in comparison to 77 K measurements.

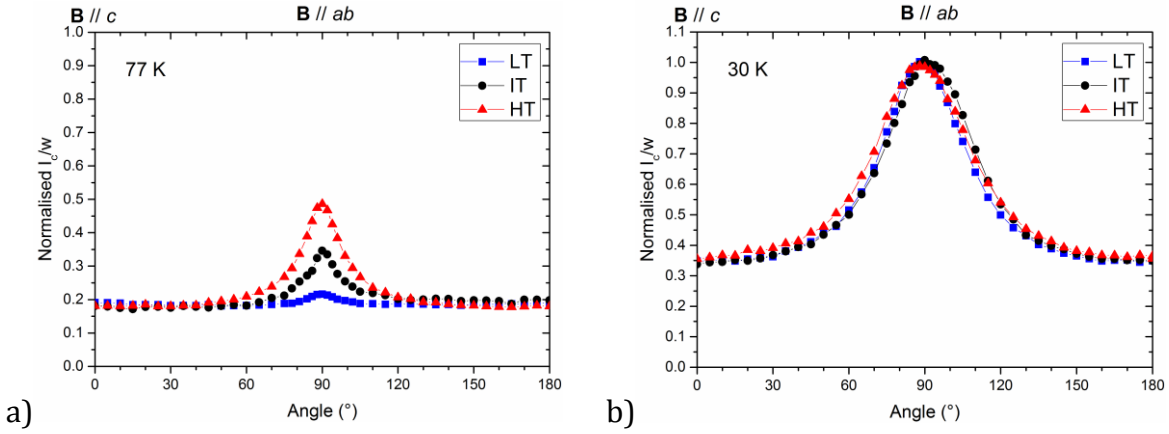

Figure 4-21: Normalised critical current data of Figure 4-19 to the self-field I_c (from Figure 4-18) measured at a) 77 K and b) 30 K of Dy-doped YBCO thin films oxygenated low (blue), intermediate (black) and high (red) temperature.

4.6.3.1 Comparison with pure YBCO

The major differences in pinning behaviours between the pure YBCO and the Dy-doped samples occur at 77 K. The Dy-doped samples present a similar isotropic pinning which was attributed to the similar size and density of $(Y,Dy)_2O_3$ nanoparticles. In contrast in the pure YBCO samples, despite the smaller Y_2O_3 nanoparticles, the HT sample presents a low isotropic pinning than at other oxygenation temperatures. It is understood that this combination of small nanoparticles and high stacking fault density is unfavourable at 77 K for the isotropic pinning in the HT sample. The 90° peak intensity is seen to increase, for both pure YBCO and Dy-doped YBCO samples, which is due to the increasing stacking fault density.

At 30 K the pinning is almost identical between the pure YBCO and the Dy-doped YBCO thin films with a difference <8 % between the six samples. This shows that despite the microstructural differences between the samples, in the form of porosity, non-superconducting Ba-Cu-O phase, stacking fault density and nanoparticles size and density, the effect on the pinning at 30 K is almost identical. The most obvious difference here is the change of the effect of the stacking faults. The increasing stacking fault density gives a pronounced increase in the anisotropic pinning behaviour at 77 K, but this effect completely disappears at 30 K.

The effect of the isotropic pinning behaviour is less pronounced. For the LT and IT pure YBCO samples, the normalised isotropic I_c increases from 0.10 to 0.30 for temperature from 77 K to 30 K respectively. For the LT, IT and HT Dy-doped YBCO samples, the normalised isotropic I_c increases from 0.20 to 0.35 for temperature from 77 K to 30 K. This increasing pinning at lower operating temperatures can be attributed to a reduced thermal depinning at lower temperatures.

An additional source of pinning can be from an increased density of pinning sites at low temperature. Reducing the operating temperature from 77 K to 30 K the coherence length approximately halves from 3.4 nm to 1.7 nm (*c*-axis) and from 0.8 nm to 0.4 nm (*ab* plane). The coherence length is of importance as it defines how large a defect needs to be to pin a vortex. In the Dy-doped samples, small regions of strain (2-5 nm) on the order of twice the coherence length at 30 K were observed (section 4.4.4). These microstrained regions may contribute to vortex pinning and explain the enhancement of the normalised I_c at 30 K compared to 77 K. These pins are always present in the sample, and are effective at 30 K, but are too small to pin a vortex at 77 K. Although they were not observed in the pure YBCO samples, similar strained regions are also likely to be present in those samples at the end of the stacking faults. Although the source of isotropic pinning is subtle and speculative, there is a marked change of the effect of stacking fault density on pinning from 77 K to 30 K. The increased stacking fault density gives a pronounced increase in the anisotropic pinning behaviour at 77 K, but this effect completely disappears at 30 K and the anisotropic pinning at low temperature is attributed to intrinsic pinning for all thin film samples.

4.7 Summary

This chapter presented XRD, SEM, EDS, TEM and I_c characterisation of the Dy-doped YBCO thin films as well as a comparison with the pure YBCO samples.

Overall, the addition of 50 % Dy affected the microstructure of the superconducting films, consequently improving the critical current. It was found that the microstructure of the Dy-doped samples was significantly less sensitive to the oxygenation temperature in contrast to the pure YBCO samples.

The 50 % Dy addition contributed to densifying the superconducting films and to inhibiting the formation of the non-superconducting Ba-Cu-O phase present in the pure YBCO films. As a result, the self-field critical current was greatly improved compared to the pure YBCO samples. The Dy-doped YBCO thin films have a mixed Dy and Y matrix. The EDS data and HRSTEM images show that the Dy and the Y are homogeneously dispersed in the matrix. The three thin films exhibit a high density of $(Y,Dy)_2O_3$ particles that are homogeneously distributed within the film and along the film growth direction, as shown by the 3D tomography results. The density of stacking faults was quantified and was found to be approximately 6 %, 10 % and 12 % at low, intermediate and high oxygenation temperature respectively. The Y124 stacking faults, although effective anisotropic pinning defects at 77 K, are detrimental to the self-field I_c. The stacking fault density was correlated (for both the YBCO and the Dy-doped YBCO samples) to the isotropic I_c at 1 T and shows that I_c increases with decreasing stacking fault density.

Chapter 5 Vortex imaging in YBCO using electron holography techniques

The aim of the chapter is to present the experimental achievements performing in-situ imaging of vortices in YBCO crystal and YBCO coated conductor using both off-axis electron holography and Lorentz microscopy. The experiments were performed using an FEI Titan 80-300 ATEM operated at 300 kV at the Center for electron nanoscopy at the Technical University of Denmark (DTU Cen). Performing off-axis electron holography and Lorentz microscopy required a preliminary understanding of the challenges of the experiments. As detailed in Chapter 1, imaging magnetic vortices in YBCO as only been successful using a 1 MV TEM [7, 107, 110] and the use of a TEM operated at 300 kV to observe vortices in YBCO is the main challenge.

The chapter first presents the crystal structure, the lower critical field (B_{c1}) and the critical temperature (T_c) characterisation results for the YBCO crystal using X-ray diffraction (XRD) and vibrating sample magnetometry (VSM) techniques. Then both Lorentz microscopy and off-axis holography results are presented for the YBCO crystal and pure YBCO coated conductor. Finally, off-axis holography was performed in the adjacent vacuum of the YBCO coated conductor at different temperature. These results also discuss the importance of experimental conditions to succeed in vortex imaging using electron holography techniques.

5.1 YBCO crystal characterisation

5.1.1 YBCO crystal purity and structure

Figure 5-1 shows three X-ray diffraction (XRD) scans of the YBCO crystal (black line) after the oxygenation cycle (section 1.5), the empty holder (red line) and the YBCO crystal scan with the holder background subtracted (blue line). In the raw YBCO scan (Figure 5-1), distinct peaks are observed at 2θ values of 8.7°, 17.6°, 26.6°, 35.7°, 45.1°, 54.7° and 64.8° which correspond to the first seven (00*l*) peaks. The overall curve of the background is due to the holder (Figure 5-1 red line). The minor peaks at 25°, 32°, 35°, 42° and 64° were also identified as being the holder contribution. As no other YBCO peaks are observed, it is concluded that the crystal has a good *c*-axis alignment. In addition, there are no unidentified peaks, indicating a high purity of the YBCO phase.

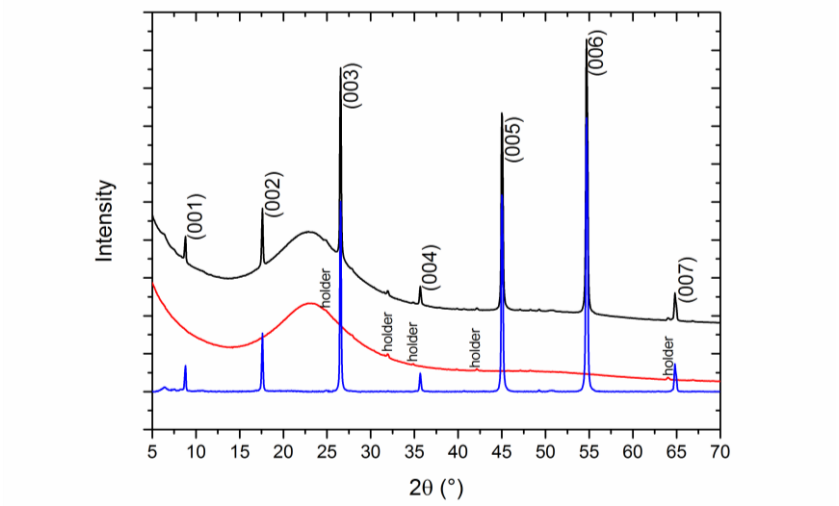

Figure 5-1: XRD θ-2θ scan of the YBCO crystal after oxygenation. The black line is the raw scan of the crystal on the holder, the red line is the scan of the empty holder only and the blue line is the result of subtracting the holder contribution from the raw scan. YBCO peaks are indexed. The intensity of the scans has been offset for clarity.

5.1.2 Critical temperature and oxygen doping

Figure 5-2 shows the magnetic moment as a function of the temperature of the YBCO crystal before and after the oxygenation cycle presented in section 2.6.1.

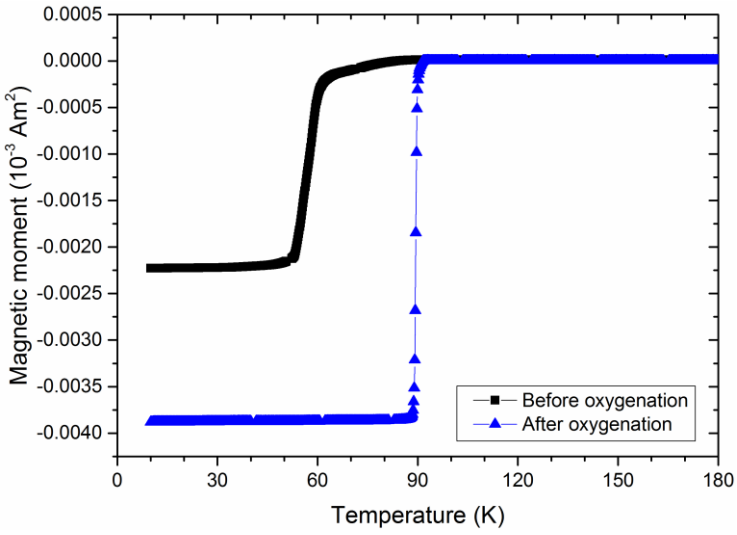

Figure 5-2: Magnetic moment of the YBCO crystal as a function of temperature before (■) and after (▲) the oxygenation cycle presented in section 2.6.1.

The critical temperature increased from 57 K before oxygenation to 90 K after oxygenation, which shows that the crystal was successfully fully oxygenated. In addition, the sharpness of the transition notably improved after oxygenation indicating good oxygen-doping homogeneity.

5.1.3 Penetration depth calculation

The YBCO crystal penetration depth is plotted as a function of temperature in Figure 5-3. It was calculated using equation (1.2), where T_c is the experimental YBCO crystal critical temperature value of 90 K and the penetration depth at zero temperature is taken to be 140 nm (Table 1-2).

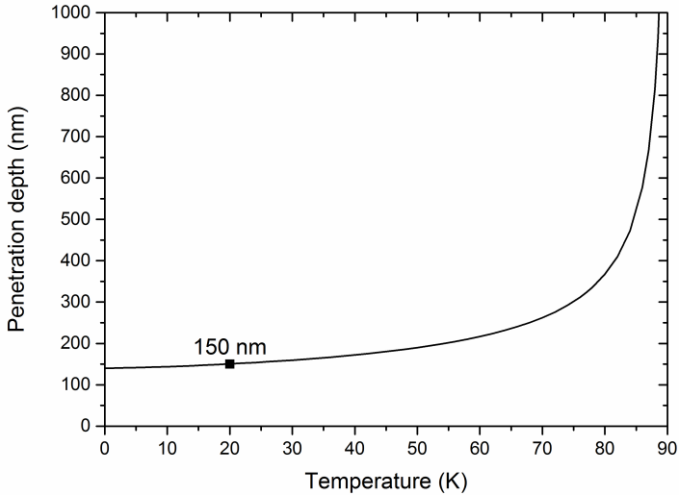

Figure 5-3: Calculated penetration depth as a function of temperature using equation (1.2), for a YBCO with a critical temperature of 90 K and λ(0) = 140 nm.

The penetration depth varies little at low temperature. However, as the temperature approaches T_c (90 K), the size of the vortex increases reaching 1 μm a few Kelvin below T_c. The He holder used for electron holography experiment reaches stable temperatures between 10 and 20 K. The observed vortices are therefore expected to have a radius around 150 nm.

5.1.4 Lower critical field

The lower critical field, B_{c1}, of the YBCO crystal after oxygenation was measured using a VSM to determine the minimum field to apply during electron holography experiments. The magnetisation $M(H)$ curves in Figure 5-4 present a linear dependence of the magnetisation at low fields.

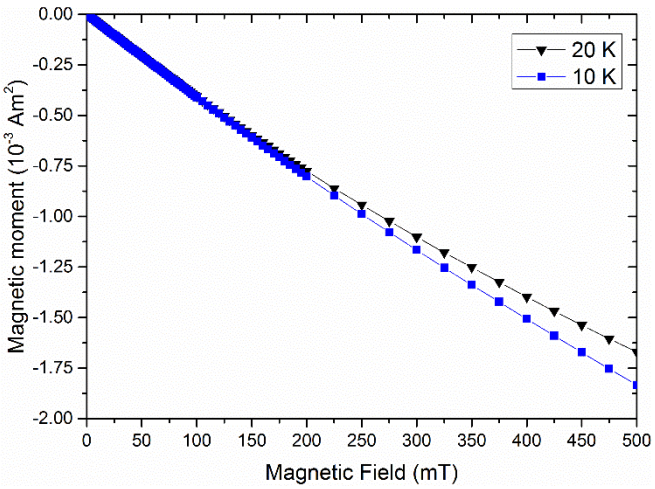

Figure 5-4: Magnetisation curves *M*(*H*) of the oxygenated YBCO crystal by VSM at 10 K (blue ■) and 20 K (black ▼).

B_{c1} corresponds to the magnetic field at which the curve departs from linearity. The determination of B_{c1} from the $M(H)$ curves was done using the method described by Li *et al.* [118] as follows. The linear dependence at low magnetic field, called the Meissner line, was determined between 2-20 mT at 10 K. The Meissner line was then subtracted from the $M(H)$ curves, giving ΔM, as plotted in Figure 5-5. For each temperature, B_{c1} is the value of the magnetic field for which the curves depart from zero. The curves were then plotted on a logarithmic scale (Figure 5-5b) and an appropriate criterion was chosen to determine B_{c1}. For ΔM smaller than 5×10^{-4} the data points are more scattered, especially at 20 K. So a criterion larger than 5×10^{-4} is preferable. For a criterion between 5×10^{-4} and 10^{-3} the lower critical field measured on the YBCO crystals after oxygenation sits between 38-48 mT at 20 K and 42-56 mT at 10 K.

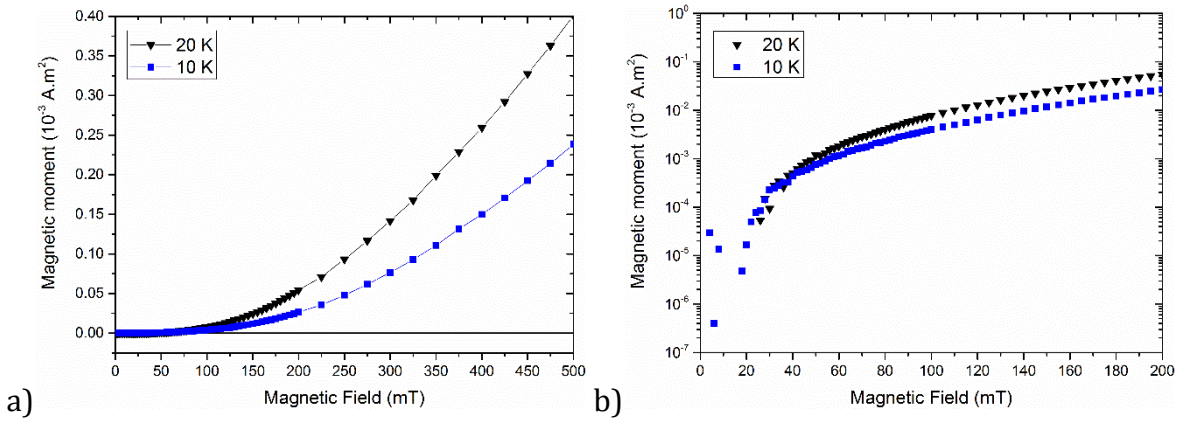

Figure 5-5: Difference between the Meissner line and the *M*(*H*) curve of the oxygenated YBCO crystal as a function of applied magnetic field at fixed temperatures of 10 K and 20 K, a) linear and b) log scale.

5.2 Electron holography on YBCO crystal

5.2.1 Lorentz microscopy

A conventional TEM micrograph of the FIB-prepared YBCO crystal is shown in Figure 5-6. The specimen has a large twinning density visible in two domains oriented at about 75° from each other. The domain at the bottom half of the image contains twins of 190 nm and 300 nm wide and the upper domain has smaller twins about 140 nm wide. The three arrows indicate darker lines characteristic of thickness differences across the specimen surface created by ion milling during FIB specimen preparation.

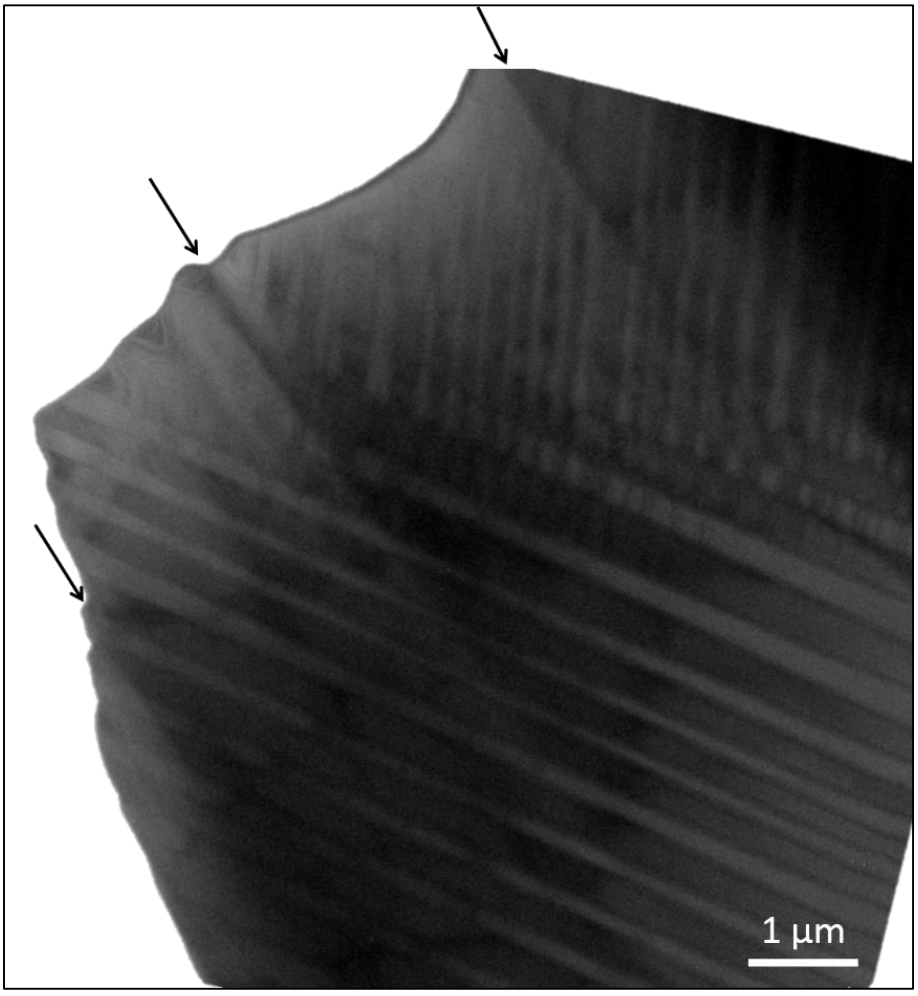

Figure 5-6: Conventional TEM micrograph of a YBCO crystal. The arrows indicate thickness contrast.

Figure 5-7 is a Lorentz micrograph of the YBCO crystal at 20 K with a defocus of -620 µm under an applied magnetic field of -6.5 mT. The two twin domains, as seen in Figure 5-6, are still visible in this image. There are black and white Fresnel fringes around the specimen edges, characteristic of a defocused image. Similar to the edges of the specimen,

the specimen thickness change also creates Fresnel fringes, especially on the area indicated by the white arrow where the thickness change is greater. The last noticeable contrast in Figure 5-7a are the round features located within the twinning bands and more clearly present at the bottom right of the image.

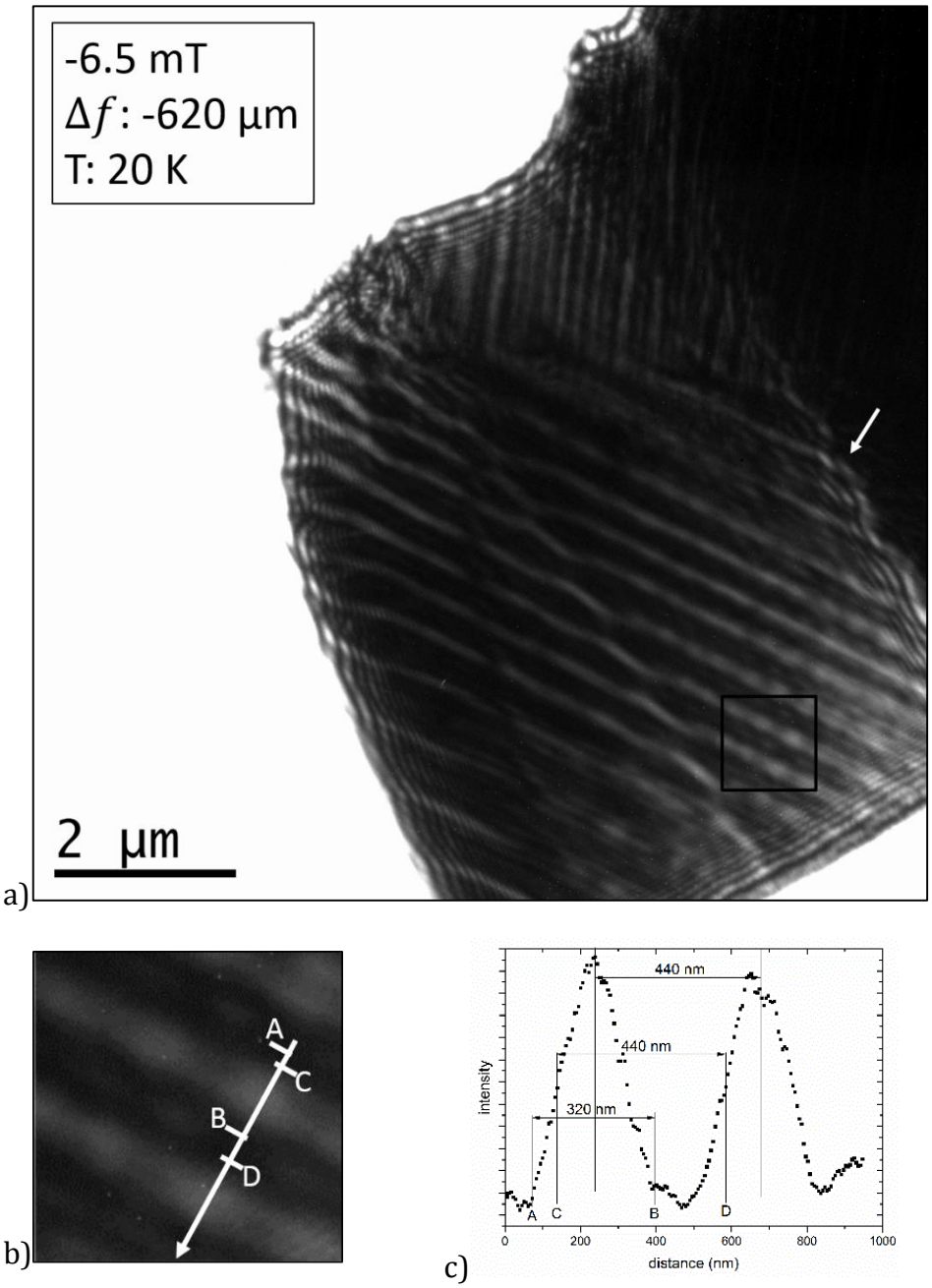

Figure 5-7: a) Lorentz micrograph of a YBCO crystal at 20 K with a defocus of about -620 µm at -6.5 mT applied magnetic field, b) the enlarged square area, c) line profile corresponding to the white arrow in b).

A magnified region highlighting the round features is shown in Figure 5-7b. A line profile was drawn to show the intensity along two of these features (Figure 5-7c) and it can be interpreted in two ways:

1. As a bright round feature (between A and B), sitting in the twin band with a maximum intensity in the centre and an intensity decay towards the outer edges. The diameter is then measured as 330 nm and the features' centres are spaced by 440 nm.
2. Or as a bright and dark feature as described in section 1.6.2 (between C and D). The size of the features is then 440 nm and their edges are directly adjacent to one another giving a spacing between their centres of 440 nm.

Several Lorentz micrographs recorded at the same temperature (20 K) but under different applied magnetic fields and defocus conditions are presented in Figure 5-8.

In all the micrographs, the contrast created by the thickness variations and the twin bands are still visible. The micrographs are ordered with increasing applied magnetic field (left to right) and defocus (top to bottom) as indicated by the arrows. Figure 5-8d is the same as Figure 5-7 and is reproduced for completeness. The top micrograph (Figure 5-8a) was recorded under a high applied magnetic field (+58.4 mT) close to focus (Δf = +47 µm). The contrasts are very similar to that seen in the conventional TEM micrograph (Figure 5-6) and almost no Fresnel fringes are visible. Two micrographs were recorded with -540 µm defocus under applied magnetic fields of +42.4 mT and +92.7 mT (Figure 5-8b and c). The contrast related to the twins is visible and the Fresnel fringes are less extended than in Figure 5-7 because of the lower defocus. Finally, Figure 5-8e was recorded with -813 µm defocus under an applied magnetic field of +35.7 mT. The Fresnel fringes on the micrograph are greatly extended and dominate the contrast of the twins that are less visible. The round features described previously seen in Figure 5-7 are not visible under higher applied magnetic fields or at other defocus conditions.

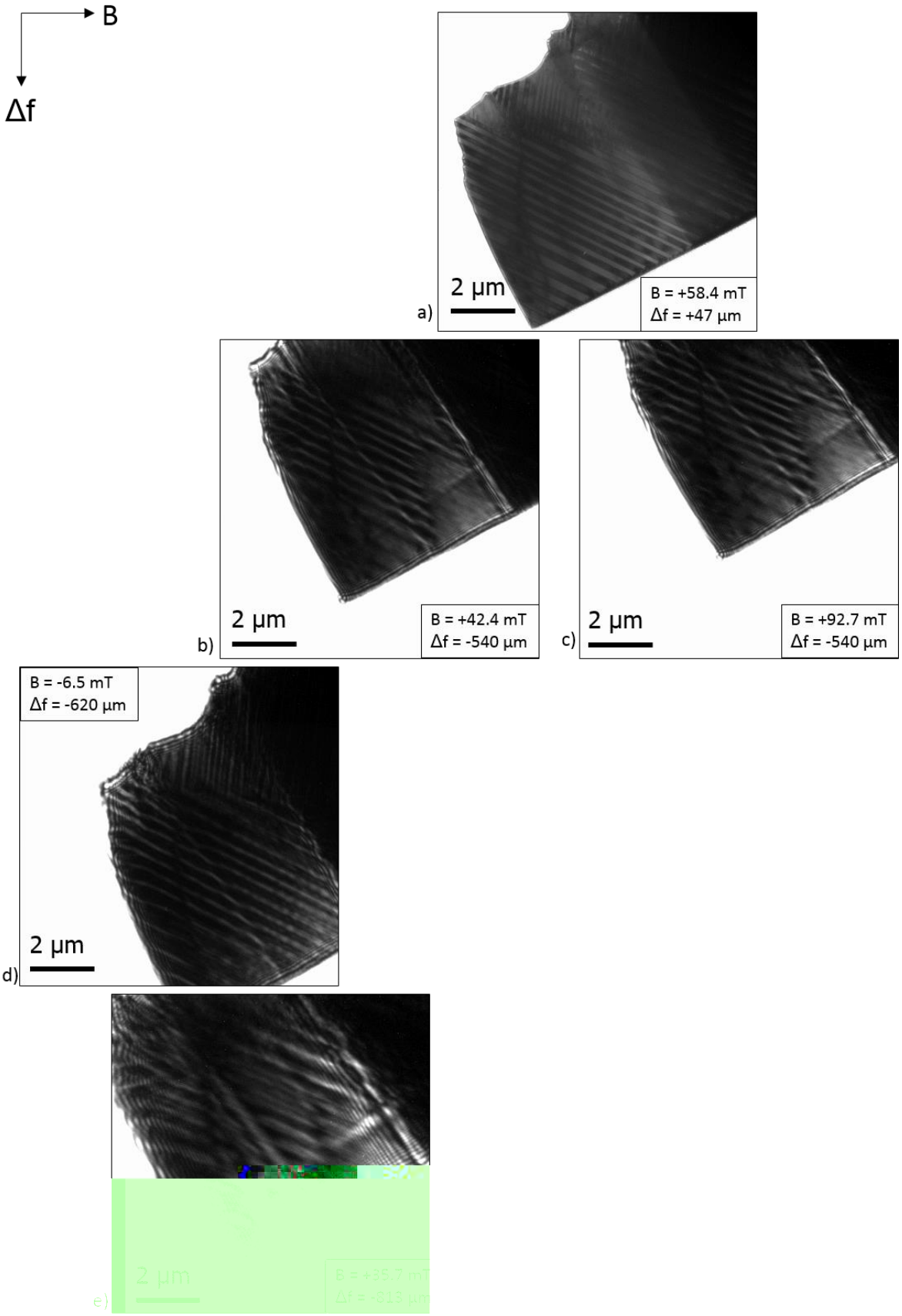

Figure 5-8: Lorentz micrographs of YBCO crystal at 20 K at different applied magnetic fields *B* and defocus conditions Δ*f* as indicated.

5.2.2 Off-axis holography

Off-axis holograms were taken of the YBCO crystal at 19 K with a -173 mT applied magnetic field. One interference micrograph is shown in Figure 5-9a. The features visible in the interference micrograph are highlighted in Figure 5-9b. The specimen is located on the right hand side of the continuous line which represents the specimen edge. The vacuum is located on the left hand side of the same line. The two parallel dotted lines are the limits of the interference fringes formed by the biprism. Finally the dashed lines are the twin boundaries that appear in two shades of grey.

In the phase image (Figure 5-9c), the regions outside the hologram field of view are not of interest as they will show only noise. Within the hologram field of view the darker grey vacuum shows a constant phase. In the sample region there are areas of various contrast. There is noise in the top band; a dark grey in the main central band; light grey in the smaller bottom band and then a dark grey (of similar contrast to the main central band) in the bottom banded region. It is interesting to see that there is noise in the bottom small band region and also at the interface between the main central band and the bottom band. The line profile within the sample region (Figure 5-9d), parallel to the sample edge to ensure any variation is not due to thickness change, shows constant intensity (the variations are of the size of a pixel and do not represent significant variation) indicating that no magnetic vortices are present. The grey variations in the top and bottom are created by crystal orientation change between the twinned regions.

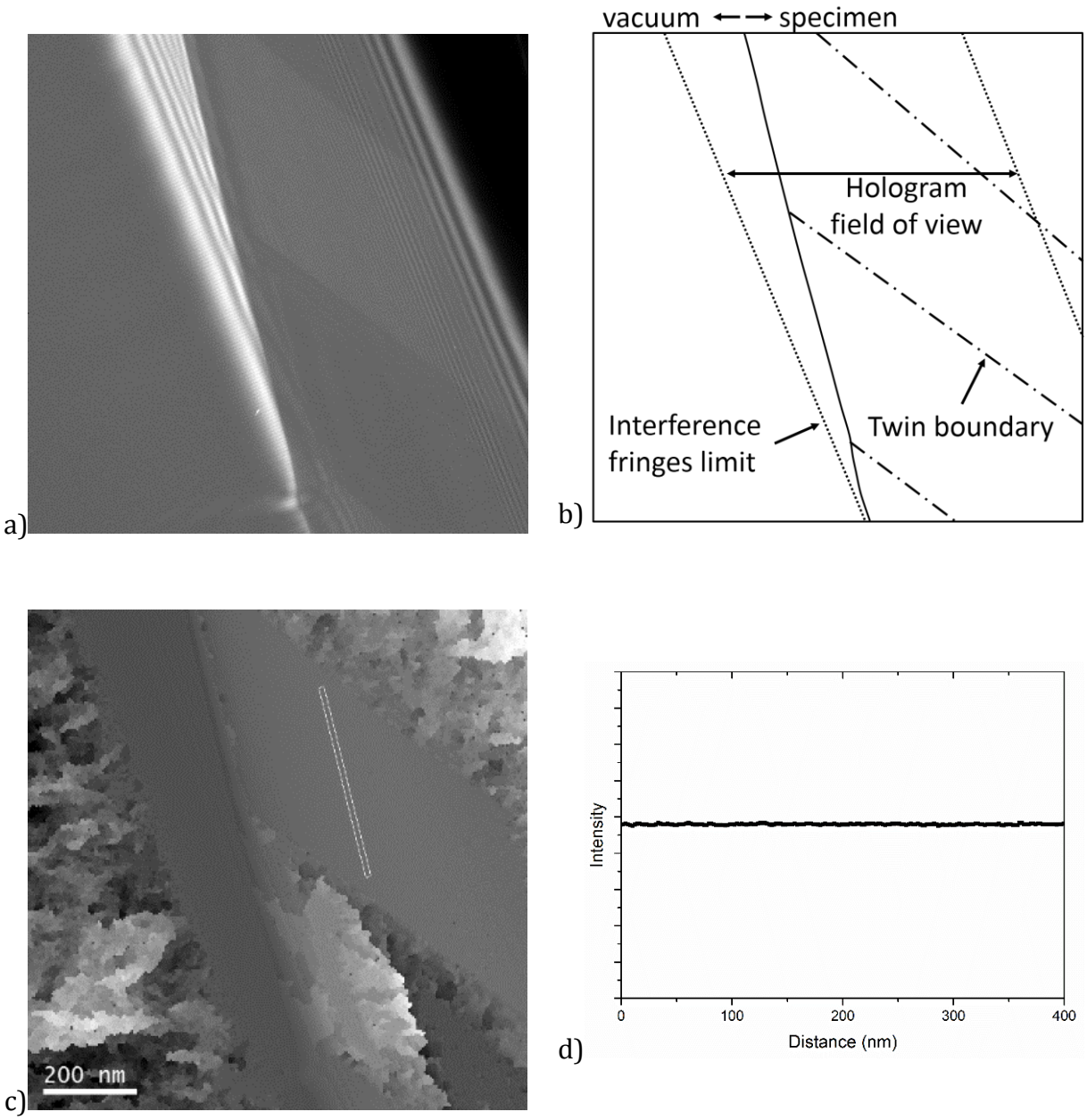

Figure 5-9: a) Interference micrograph of the YBCO crystal, b) schematic of features visible in the interference micrograph, c) phase image and d) line profile corresponding to the line in the phase image.

5.3 Electron holography on YBCO coated conductor

5.3.1 Lorentz microscopy

Figure 5-10 is a defocus series of Lorentz micrographs from the YBCO thin film at 10.8 K and -5.0 mT. The micrograph in Figure 5-10e is recorded at a defocus of 0 mm making it the focused image, equivalent to a conventional TEM micrograph. The specimen is the darker grey region in the centre of the image. The top right bright corner is the vacuum, and the black top left and bottom right corners are thicker areas of the specimen that are not electron transparent. The specimen has many voids in the electron transparent area. This is due to the porosity in the coated conductor sample accentuated during FIB preparation. Dark and bright stripes are also visible from the bottom left corner to the vacuum. This is a curtaining effect and the light and dark grey regions represent thickness variations created during specimen thinning (as described in section 2.6). The other micrographs (from a to i) show defocus values of -6.5 mm, -4.87 mm -3.85 mm and -1.62 mm; and +1.62 mm, +3.85 mm, +4.87 mm and +6.5 mm respectively. In those out-of-focus micrographs Fresnel fringes appear at the specimen edge and around the voids (Figure 5-10d and Figure 5-10f). Those fringes become more numerous and larger as the defocus increases. At high defocus (Figure 5-10b and Figure 5-10h), the fringes of neighbouring features interfere with each other. As the micrographs are dominated by the Fresnel fringes it is not possible to see any other contrast features, such as those anticipated from a vortex.

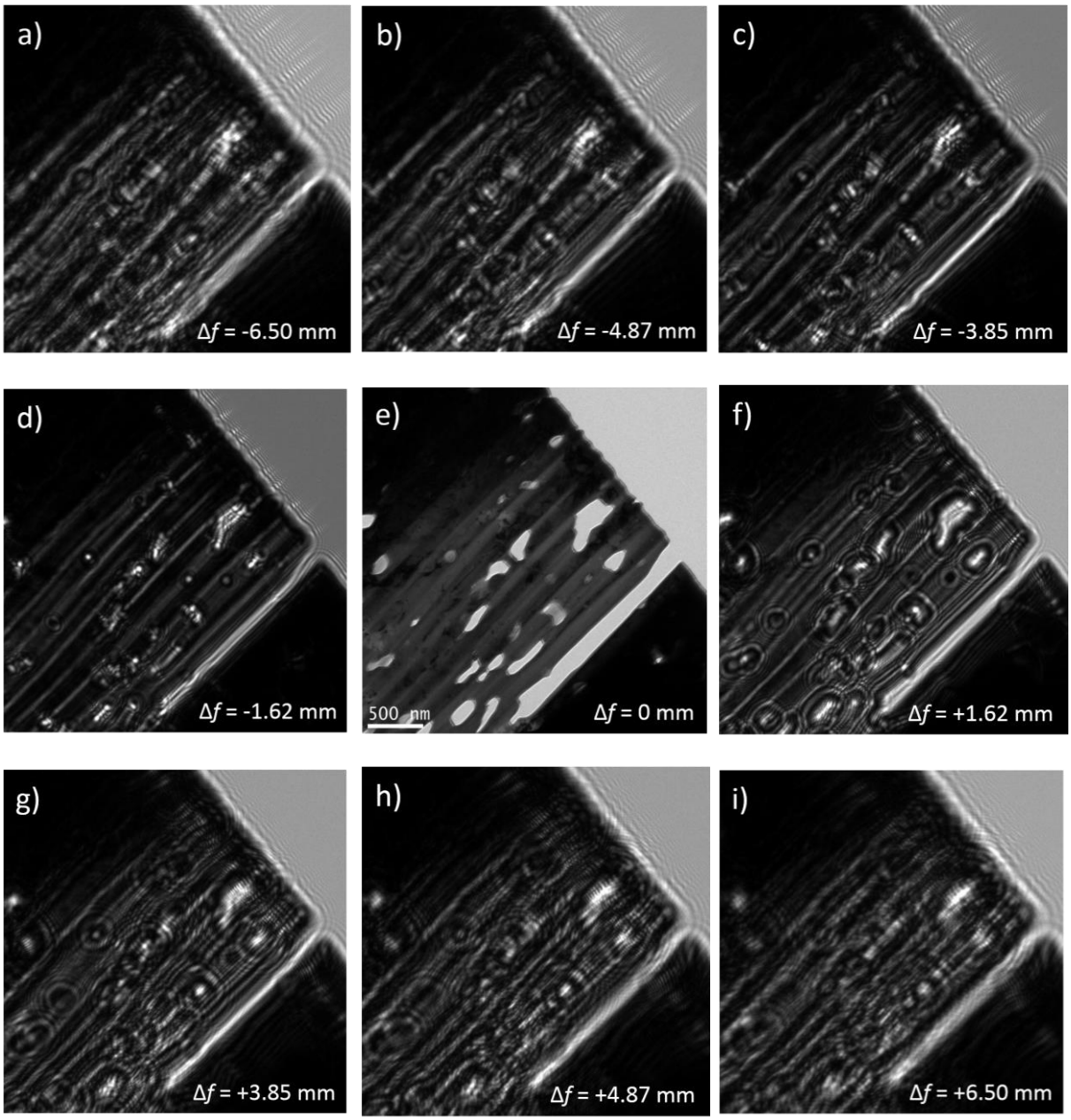

Figure 5-10: Lorentz micrograph defocus series on FIB prepared YBCO thin film at different defocus condition (indicated on the images). The specimen was hold at 10.8 K under -5.0 mT applied magnetic field. Scale bar in image e).

5.3.2 Off-axis holography – observation in the sample

A series of off-axis holograms were recorded from the YBCO thin film sample at stable temperatures between 10 K and 13 K for applied magnetic fields from -100 to 200 mT. Figure 5-11a is an interference micrograph of the YBCO thin film at 10 K and -100 mT, and Figure 5-11b and Figure 5-11c are the corresponding phase image and unwrapped phase image respectively.

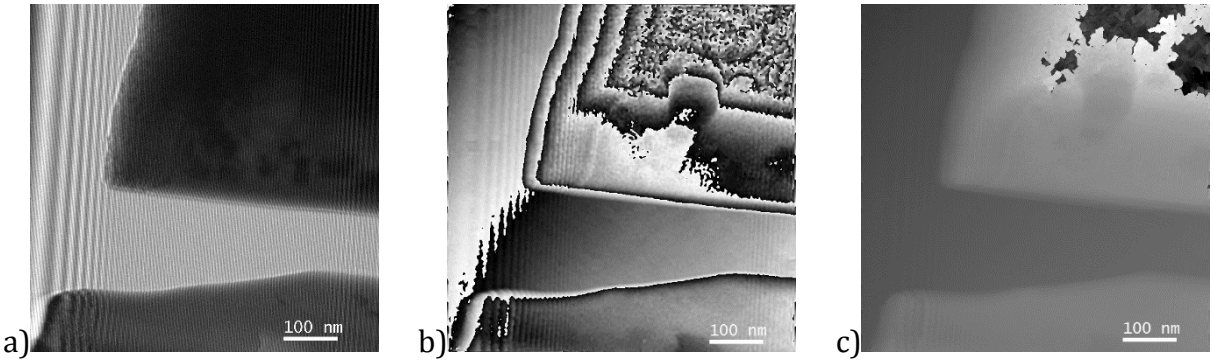

Figure 5-11: a) Interference micrograph of YBCO thin film, b) phase image and c) unwrapped phase image. The specimen was at 10 K under an applied magnetic field of -100 mT.

The dark parts of Figure 5-11a at the top right and the bottom are the specimen and the bright area with visible Fresnel and interference fringes is the vacuum. After reconstruction, the phase image (Figure 5-11b) is extracted and the black and white contrast is associated to phase variations. The top right corner of the upper part of the specimen is noise and is also visible in the unwrapped phase image (Figure 5-11c).

The phase image was amplified 4, 8 and 16 times and the resulting unwrapped phase images are shown in Figure 5-12. The phase amplification is done by displaying $\cos(n\varphi)$ with n = [4, 8, 16] and φ from Equation (1.14) [144].

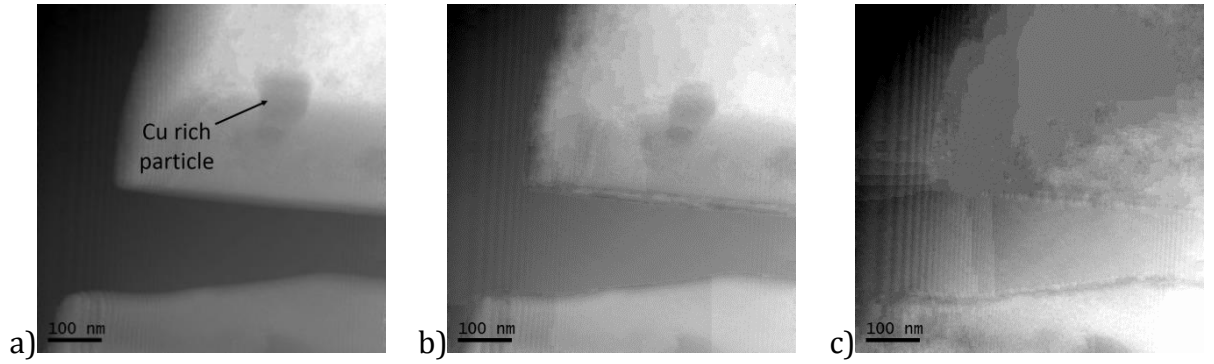

Figure 5-12: Unwrapped phase image after amplification a) 4×, b) 8× and c) 16× of the phase image in Figure 5-11b.

Amplifying the signal aims to highlight features like vortices but will also amplify noise. If the phase is originally constant, then the amplification has no effect and the phase remains constant after amplification like in the vacuum (Figure 5-12a and b).The noisy signal in the specimen at the top right corner of the image (Figure 5-12a) is only noisier after amplification (Figure 5-12b and c). In the vacuum area in Figure 5-12c discontinuities are visible on the extreme left side of the image. These areas correspond

to the edges of the interference fringes or, in other words, to the edges of the overlap width where Fresnel fringes appear. A darker area in the middle of the top part of the specimen is observed after phase amplification, but this is a copper-rich particle in the YBCO matrix. For this hologram, phase amplification highlights the phase noise that was not visible without amplification and no phase ramping or contours are observed in the sample that could be associated with vortices.

5.3.3 Off-axis holography – observation in the vacuum

A third experiment on the YBCO thin film was performed to observe magnetic lines leaking from the specimen into the vacuum. The specimen was made as thick as possible, 800 nm, only milling away the substrate and the buffer layers. It was cooled to cryogenic temperature under no applied magnetic field. Once at 10 K, 809.2 mT magnetic field was applied and holograms were recorded at different temperatures between 10 K and 94 K.

The object and reference interference micrographs acquired at 39 K are presented in Figure 5-13a and Figure 5-13b respectively. The edge of the specimen is visible in the object interference micrograph (as shown in the schematic by the black line in Figure 5-13c). The top part of the micrograph is black as the sample is not electron transparent and the bottom grey part, below the line, is the vacuum. The specimen was placed beside the interference fringes to allow observation of the magnetic lines leaking out of the sample as shown in Figure 1-15. The hologram was reconstructed using the reference hologram to get the phase image (Figure 5-13d). All the grey shades outside of the interference fringes are noise which contains no information.

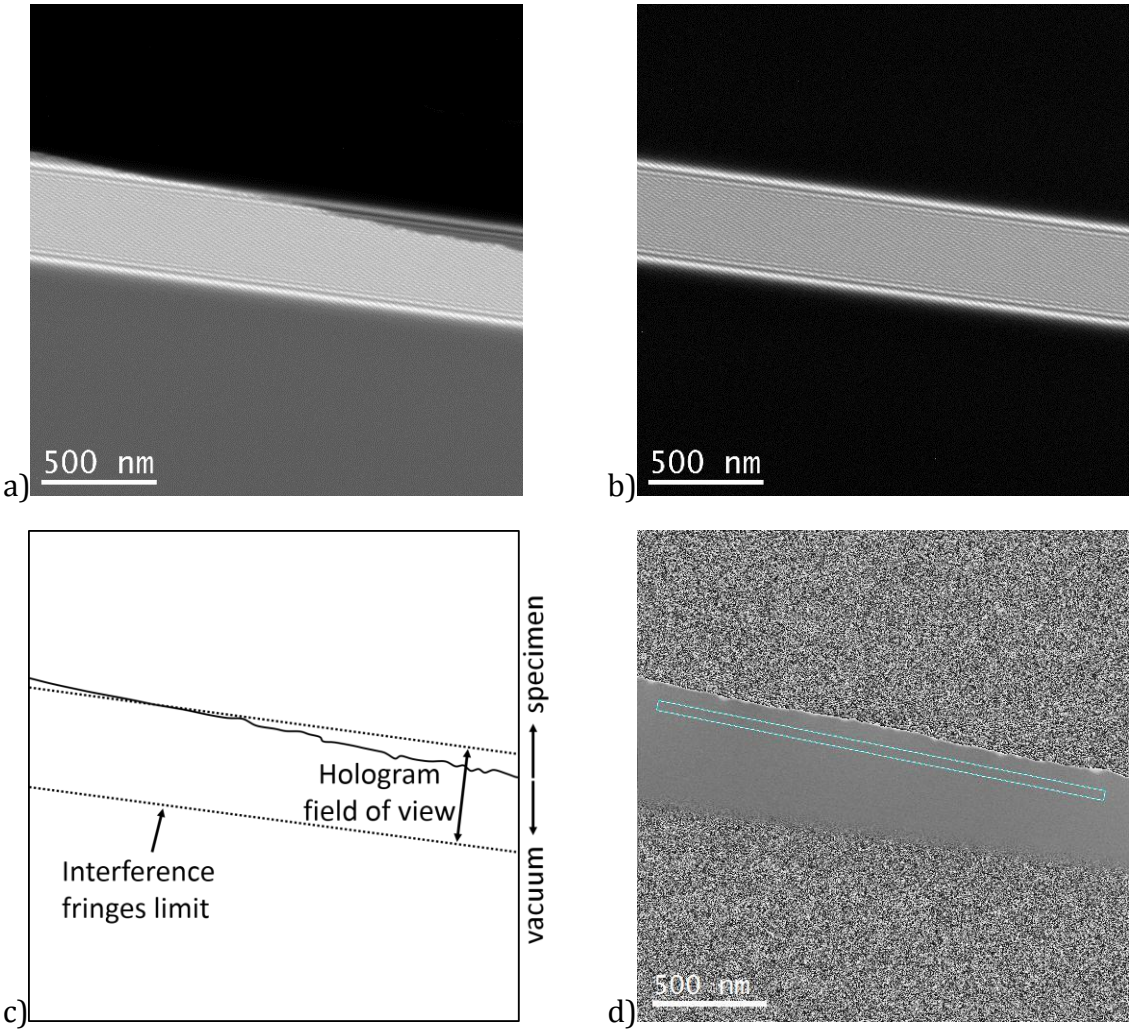

Figure 5-13: a) Object interference micrograph of YBCO thin film at 39 K under 809.2 mT applied magnetic field, b) reference interference micrograph, c) schematic of the object interference micrograph and d) phase image.

The phase image (Figure 5-13d) was 4× amplified to increase the contrast and the result is shown in Figure 5-14a. It is now visible that the phase at the edge of the sample exhibits variations. The line profile (Figure 5-14b), drawn parallel to the sample edge, shows that the phase variation in the vacuum reaches two minima spaced by 1 μm.

a) 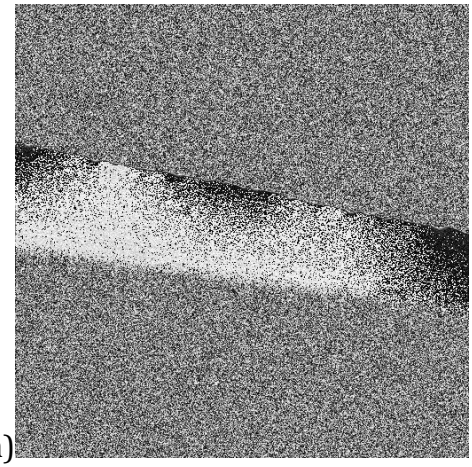

b) 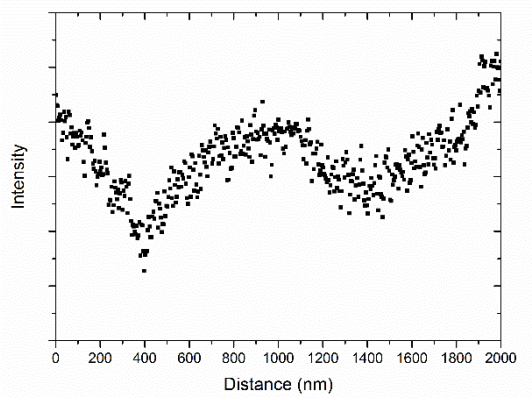

Figure 5-14: a) 4× phase-amplified micrograph of Figure 5-13d and b) line profile corresponding to the line in the phase image (Figure 5-13d).

5.4 Discussion and conclusions

This section will discuss the off-axis holography and Lorentz microscopy micrographs described in each of the results section for the YBCO crystal and the YBCO thin film.

5.4.1 YBCO crystal

5.4.1.1 Lorentz microscopy

The aim of the following section is to discuss the nature of the features visible in Figure 5-7 by examining the experimental conditions, the observed radius and the spacing of those features and to answer the question: are these features magnetic vortices?

The only test conditions under the round features were observed was at an applied field of -6.5 mT with a -620 µm defocus. The applied magnetic field was gradually increased and different defocus settings were tested for each applied magnetic field until a change in the contrast was observed that could potentially be magnetic vortices. The applied magnetic field, measured feature size and feature spacing seen in Figure 5-7 are compiled and compared with calculated values in Table 5-1.

The feature radius in Figure 5-7 can be determined in two ways:

i) By only considering the bright part of the feature. The diameter is measured 330 nm which gives a radius of 165 nm.

ii) By considering both the bright and the dark part of the feature as the way a vortex looks like as explained by Beleggia [95] and observed by Tonomura and

Loudon [79, 109-111, 114]. The diameter of the feature is then 440 nm giving a radius of 220 nm.

From theory, the penetration depth (and consequently observed vortex size) is a function of temperature, not applied magnetic field, and the vortex size increases with increasing temperature. The theoretical penetration depth at 20 K is 150 nm.

The feature radius may not be an accurate criterion to conclude whether we are observing vortices. First, Beleggia showed that the apparent vortex size varies with defocus and can double depending on the applied defocus (Figure 3 in reference [94]). Second, Loudon *et al.* [79, 116] measured the penetration depth from Lorentz micrographs by comparing experimental Lorentz micrographs with simulations. However, these experiments were done on a perfect MgB_2 single crystal containing no pinning defects, which may alter the vortex shape/contrast. Here, the twin contrast is dominant and alters the discussed features contrast, leading to the two previously mentioned interpretations of their shape and size. The observed size of the features is then reasonably in the range of vortices according to reference [94], even though the shape and contrast is overwhelmed by the presence of the twins and does not present a clear bright and dark contrast as seen by others ([94, 95, 109, 110]).

The feature spacing in Figure 5-7 is approximately 440 nm (along and across the twin bands) at an applied magnetic field of 6.5 mT. In comparison to the vortex size, the vortex spacing is a function of applied magnetic field and not temperature as shown by Equation (1.5) and vortex spacing decreases with increasing applied magnetic field (in case of no vortex pinning occurring).

According to Benkrouda and Clem [120], there is magnetic field amplification around type II superconductors in TEM conditions. As such, despite the applied field being 6.5 mT, it is anticipated that the actual local field around the specimen is ~650 mT (calculated using Equation (1.18) with a specimen length, L_x, and thickness, L_z, of 10 μm and 0.1 μm respectively).

It seems reasonable to take into account the locally amplified magnetic field around a very small sample because Loudon's experiments [15, 79, 114] have shown that it is possible to image vortices applying a magnetic field considerably below the lower critical field.

Table 5-1: Comparison of theoretical and the measured penetration depth and vortex spacing under an applied field of 6.5 mT at 20 K.

	Experimental observation (Figure 5-7)	**Theory Without considering a locally enhanced magnetic field**	**Theory Considering a locally enhanced field calculated using Equation (1.18)**
Temperature (K)	20	20	20
Applied magnetic field *B* (mT)	6.5	6.5	~650
Feature radius/ λ (nm)	i) 165 (bright round feature) ii) 220 (bright and dark feature)	150	150
Vortex spacing	440 nm	611 nm	61 nm

At a field of 650 mT the vortices should be spaced at approximately 61 nm when no pinning occurs. This value is lower than the measured feature spacing of 440 nm in Figure 5-7 and especially, lower than twice the theoretical penetration depth. Grissonnanche *et al.* [145] measured the upper critical field of YBCO crystal to be about 22 000 mT ± 9 % between 0-20 K. This means that even considering a locally amplified magnetic field around the specimen, the experiment was performed below the upper critical field. However at such high applied magnetic field, it is expected to have a large density of magnetic vortices. Any higher applied magnetic field does not increase the number of vortices and the spacing between them is the lowest.

Furthermore, calculations using Equation (1.18) show that the local field around the specimen in Figure 5-8 is 3600, 4300, 5900, and 9300 mT for the micrographs in Figure 5-8e, b, a and c respectively. Those fields are still lower than the upper critical field, but no features similar to the ones seen in Figure 5-8d are seen. This probably means that, if the features were vortices, the applied defocus is not appropriate for the applied magnetic field, or the density of vortices is too high and individual vortices are not visible.

To conclude, magnetic vortices may have been observed using Lorentz microscopy on the YBCO crystal in Figure 5-7. The size and spacing of the observed features are reasonably close to theoretical expectations under the experimental temperature, applied magnetic

field and defocus. However the expected bright and dark contrast is less clear due to the presence of the twins. A way to confirm that those features are vortices would be to repeat the experiment in similar defocus condition and slightly changing the applied magnetic field. If the number of observed features varies with the magnetic field, it would confirm that they are magnetic vortices.

5.4.1.2 Off-axis holography

The aim of the off-axis holography experiment performed on the YBCO crystal (presented in section 5.2.2) was to image the magnetic flux lines within the sample under an applied magnetic field of -173 mT at 19 K. The phase image does not present any phase variation in the specimen in this area (as shown by Figure 5-9d) under the experimental conditions. As discussed in the previous section, the applied magnetic field is high enough to be above the lower critical field of YBCO, whether or not the local field around the specimen is amplified. This lead to two possible conclusions:

- The combination of the TEM conditions (300 kV, applied magnetic field, biprism settings, temperature) is not suitable for magnetic field and vortex imaging in YBCO crystals.
- The observed magnetic field in the imaged region is constant and there are no vortices in this particular area at the time of the acquisition.

5.4.2 YBCO coated conductor

Three experiments were performed on the YBCO coated conductor: Lorentz microscopy, off-axis holography with the field of view in the specimen and off-axis holography with the field of view in the vacuum. More detailed conclusions for each experiment are explained in the following paragraphs.

In the Lorentz microscopy imaging, the temperature was set at 10.8 K and the applied magnetic field was -5 mT, leading to a theoretical penetration depth of about 150 nm and vortex spacing of about 691 nm. The chosen experimental conditions were therefore theoretically appropriate to observe vortices in the samples. However the contrast in the out-of-focus holograms created by the voids and curtaining are predominant and therefore no vortices are visible in those conditions. It was concluded that the Lorentz microscopy of the YBCO thin film sample shows no clear evidence of vortices under the investigated conditions, due to the complex sample microstructure.

The off-axis holography with the specimen located in the field of view did not highlight magnetic field changes. The phase amplification enhanced the noise created by the nanodefects and the non-YBCO phases contained in the matrix. Considering the size of the image it was concluded that the phase could have shown one vortex in the area if any were to be seen in those conditions.

Finally, for the field of view located in the vacuum, the hologram showed phase variation at the edge of the sample at 39 K. However the two minima of the phase variation spaced by 1 µm do not match the theoretical size (about 345 nm in diameter) of vortices at 39 K under 809 mT applied magnetic field. Further investigation would be required to conclude if it is only related to magnetic field variations due to the presence of vortices.

Chapter 6 General conclusions

6.1 Correlation of microstructural and electrical properties in YBCO coated conductors

Coated conductors have a complex microstructure and it is the combination of several distinct defect species that gives them their great performance. The effects of individual structural defects in superconducting materials on the critical current, I_c, are known to be non-additive. That is to say, for example, adding more nanoparticles does not simply improve the isotropic pinning under certain conditions, but also affects the anisotropic pinning.

This work studied the effect of oxygenation temperature in pure YBCO and 50 % Dy-doped YBCO coated conductors on the films' microstructure and I_c.

Changing only the oxygenation temperature leads to many microstructural differences for the pure YBCO films:

- The film texturing is sensitive to the oxygenation temperature. Although no monotonic trend is observed, the out-of-plane (*c*-axis) and in-plane (*ab* plane) misorientations show variation with oxygenation temperature.
- The stacking fault density increases with oxygenation temperature being approximately 8 %, 23 % and 36 % at low, intermediate and high oxygenation temperature respectively.
- The degree of orthorhombicity decreases with increasing oxygenation temperature, which is concomitant with the increasing stacking fault density.
- The presence of Cu-rich phases, such as Ba-Cu-O and Cu-O, is reduced with increasing oxygenation temperature which was associated with the increase of the stacking fault density.

The 50 % addition of Dy has a major effect on the YBCO coated conductor as the only obvious change in the Dy-doped samples with increasing oxygenation temperature is an increase in the stacking faults density. This contrasts with the pure YBCO microstructure which is much more sensitive to the oxygenation temperature. Therefore the addition of 50 % Dy:

- Prevents the formation of Ba-Cu-O phases [4]. The quantity of 50 % addition of Dy to the YBCO thin film allows more (Y,Dy)BCO to form and avoids the formation of the Y poor Ba-Cu-O phases present in the YBCO thin films.
- Reduces stacking fault formation. As Ba-Cu-O formation is prevented, the primary source of Cu-O for the stacking faults is removed. As such, stacking fault formation is reduced: approximately 6 %, 10 % and 12 % at low, intermediate and high oxygenation temperature respectively.
- Densifies the (Y,Dy)BCO films. The three Dy-doped thin films have a denser surface porosity (2 %) than the pure YBCO thin films (4.1 %). The surface porosity is uniformly distributed across the pure YBCO thin film surface, while the Dy-doped films present denser areas. The porosity is independent of the oxygenation temperature.
- Generates nano-sized $(Y,Dy)_2O_3$ by substitution of Y by Dy in the Y_2O_3. In the (Y,Dy)BCO thin films, the nanoparticles are smaller than in the YBCO thin films. The size of the $(Y,Dy)_2O_3$ is independent of oxygenation temperature, as opposed to the larger Y_2O_3 nanoparticles in the pure YBCO films.

The electrical properties of the pure YBCO and the Dy-doped YBCO samples were compared leading to the following conclusions.

- The reduction in non-superconducting phases (e.g. Ba-Cu-O) and the improved densification leads to an improved self-field I_c and isotopic I_c for the Dy-doped thin films in comparison to the YBCO thin films. In addition, a systematic trend of decreasing self-field I_c is observed with increasing oxygenation temperature for both pure YBCO and Dy-doped YBCO samples which is attributed to the increasing density of Y124-like stacking faults in both type of samples.
- Overall, there is a negative correlation between the stacking fault density and the isotropic critical current at 77 K and especially at 30 K at any applied magnetic field angle.
- The stacking faults do contribute to vortex pinning at 77 K for magnetic fields applied parallel to the *ab* plane. However, at 30 K, the stacking faults are not effective pinning centres for magnetic fields applied parallel to the *ab* plane. The anisotropic pinning at 30 K is attributed to intrinsic pinning.

These are important findings, that despite the stacking fault being a two dimensional vortex pinning defect, which typically only alters the anisotropic pinning, in this case they are found to be correlated in a negative way with the critical current. Limiting the stacking fault density alongside the presence of small nanoparticles is therefore an important factor in increasing I_c at both 30 K and 77 K, and this was achieved with the 50 % Dy addition in the YBCO coated conductors. This is important for applications and shows that it is preferable to reduce the density of stacking faults for devices operating at low temperatures (30 K). It also shows that measurements of I_c trends at 77 K cannot be extrapolated to estimate the performance at 30 K.

6.2 Vortex imaging using electron holography

Off-axis electron holography and Lorentz microscopy were performed on both a YBCO coated conductor and a YBCO crystal using an FEI Titan ATEM operated at 300 kV. Progress has been made in understanding the experimental requirements to image vortices in YBCO at 300 kV in terms of the sample configuration, the magnetic field to apply and the experimental conditions.

Specimen from both the YBCO film and the YBCO crystal were prepared using focused-ion beam scanning electron microscopy and milled to a uniformly thin lamella of approximately 100 nm. This thickness was sufficiently electron transparent to see the twins present in the YBCO crystal. The thickness uniformity and the surface quality are critical and are achievable on crystal samples. However, the high density of defects, voids, and secondary phases present in the YBCO film made the FIB sample preparation challenging for the electron holography requirements.

Due to magnetic field amplification around the TEM specimen, the magnetic field penetrates the superconductor well below the lower critical field. Therefore a magnetic field as low as 6.5 mT allowed the observation of vortex-like features in the YBCO crystal using Lorentz microscopy, while the lower critical field was measured to be approximately 38–56 mT for temperatures comprised between 20 K and 10 K.

Three experiments were performed to image vortices in the YBCO film: Lorentz microscopy, off-axis electron holography with the field of view in the specimen and off-axis electron holography with the field of view in the vacuum. Although the experimental conditions (temperature of 10.8 K and applied magnetic field of -5 mT) for the Lorentz microscopy were theoretically appropriate to observe vortices, the contrast in the out-

of-focus holograms from the defects (voids, thickness variation and phases) was predominant. Therefore no vortices were observed under those conditions due to the complexity of the sample microstructure. The off-axis holography with the specimen located in the field of view did not highlight changes in magnetic field. The chosen conditions should have allowed the observation of one vortex if any was to be seen in the area of observation. It is possible that the area of observation was too small. When the field of view was located in the vacuum, phase variation was observed at 39 K at the edge of the specimen, however further investigation is required to conclude whether the variation is due to the presence of vortices. To know if the phase variation observed in the vacuum region of the off-axis holography experiment on the thin film is related to magnetic field changes or if it is a charging effect, the experiment could be repeated at different applied magnetic field. If the phase variation is still observed at the same temperature but for different applied magnetic field, this would mean that the phase variation is created by charging effects.

In general, a larger field of view would allow a larger area of observation. This would be a particular improvement for off-axis holography experiments. To get a larger field of view, two options are possible. First, reducing the accelerating voltage of the microscope to 120 kV. For lower accelerating voltage and at the same biprism voltage, the biprism deflects more and allows a larger field of view. Second, undertaking measurements at 300 kV at low magnification. The second option is preferable as a lower accelerating voltage has the disadvantage of requiring an even thinner specimen, which would be detrimental due to the requirement of a relatively thick specimen for vortex observation using Lorentz microscopy.

Imaging vortices in the YBCO crystal using Lorentz microscopy at 300 kV was a significant challenge and tentative observation of vortices in the YBCO crystal was made for the first time using Lorentz microscopy at 300 kV. This is a great step towards directly imaging vortices in YBCO. The appropriate defocus using Lorentz microscopy on the YBCO crystal was found to be approximately –620 μm. For larger applied defocus the Fresnel fringes were dominant, whose contrast obscured the one of potentially visible vortices.

A way to confirm that the features seen in the YBCO crystal using Lorentz microscopy are magnetic vortices would be to repeat the experiment changing the applied magnetic field. It would be expected that the density of the features increases or decreases with the

applied magnetic field, therefore confirming that those features are magnetic vortices and that the defocus used is appropriate. Another way of confirming the suitability of the conditions used for observing magnetic vortices in the YBCO is to repeat the experiment with a sample presenting larger twins or an untwinned YBCO crystal, removing the Fresnel fringes induced with the applied defocus.

Bibliography

[1] Bednorz J G and Müller K A, *Possible high T_c superconductivity in the Ba-La-Cu-O system.* Zeitschrift für Physik B Condensed Matter, **64** (2). pp. 189-193, 1986.

[2] Wimbush S C, *Superconductors*, in *Materials for sustainable energy applications*, X Moya and D Muñoz-Rojas, Editors, Pan Stanford Publishing. ISBN 9789814411813, 2016.

[3] Foltyn S R, Civale L, Macmanus-Driscoll J L, Jia Q X, Maiorov B, Wang H, and Maley M, *Materials science challenges for high-temperature superconducting wire.* Nature Materials, **6** (9). pp. 631-642, 2007.

[4] Holesinger T G, Civale L, Maiorov B, Feldmann D M, Coulter J Y, Miller D J, Maroni V A, Chen Z, Larbalestier D C, Feenstra R, Li X, Huang Y, Kodenkandath T, Zhang W, Rupich M W, and Malozemoff A P, *Progress in nanoengineered microstructures for tunable high-current, high-temperature superconducting wires.* Advanced Materials, **20** (3). pp. 391-407, 2008.

[5] Cowley J M, *Twenty forms of electron holography.* Ultramicroscopy, **41** (4). pp. 335-348, 1992.

[6] Gabor D, *A new microscopic principle.* Nature, **161** (4098). pp. 777-778, 1948.

[7] Harada K, Osakabe N, and Ono Y A, *Electron Microscopy Study on Magnetic Flux Lines in Superconductors: Memorial to Akira Tonomura.* IEEE Transactions on Applied Superconductivity, **23** (1), art. 8000507, 2013, http://dx.doi.org/10.1109/TASC.2012.2232924.

[8] Tonomura A, *Applications of electron holography.* Reviews of Modern Physics, **59** (3). pp. 639-669, 1987.

[9] Tonomura A, *Holography in the transmission electron microscope*, in *Characterization of High T_c Materials and Devices by Electron Microscopy*, N D Browning and S J Pennycook, Editors, Cambridge University Press. ISBN 9780521031707, 2006.

[10] Holesinger T G, Maiorov B, Ugurlu O, Civale L, Chen Y, Xiong X, Xie Y, and Selvamanickam V, *Microstructural and superconducting properties of high current metal-organic chemical vapor deposition $YBa_2Cu_3O_{7-\delta}$ coated conductor wires.* Superconductor Science and Technology, **22** (4), 2009.

[11] Long N, Strickland N, Chapman B, Ross N, Xia J, Li X, Zhang W, Kodenkandath T, Huang Y, and Rupich M, *Enhanced in-field critical currents of YBCO second-generation (2G) wire by Dy additions.* Superconductor Science and Technology, **18** (12). pp. S405-S408, 2005.

[12] Strickland N, Talantsev E F, Xia J, Long N, D'Souza P, and Hoffmann C, *Low-temperature pinning behavior of MOD YBCO coated conductors.* IEEE Transactions on Applied Superconductivity, **21** (3). pp. 3214-3217, 2011.

[13] Rupich M W, Schoop U, Verebelyi D T, Thieme C L H, Buczek D, Li X, Zhang W, Kodenkandath T, Huang Y, Siegal E, Carter W, Nguyen N, Schreiber J, Prasova M, Lynch J, Tucker D, Harnois R, King C, and Aized D, *The development of second generation HTS wire at American superconductor.* IEEE Transactions on Applied Superconductivity, **17** (2). pp. 3379-3382, 2007.

[14] Tinkham M, *Introduction to superconductivity,* Second edition Edition, Courier Corporation, ISBN 07-064878-6, p. 454, 1996.

[15] Loudon J C and Midgley P A, *Imaging flux vortices in type II superconductors with a commercial transmission electron microscope.* Ultramicroscopy, **109** (6). pp. 700-729, 2009, http://dx.doi.org/10.1016/j.ultramic.2009.01.008.

[16] Poole Jr C P, Farach H A, Creswick R J, and Prozorov R, *12 - Type II Superconductivity*, in *Superconductivity (Second Edition)*, C P Poole, H A Farach, and R J C Prozorov, Editors, Academic Press: Amsterdam. ISBN 978-0-12-088761-3, pp. 337-383, 2007.

[17] Wu M K, Ashburn J R, Torng C J, Hor P H, Meng R L, Gao L, Huang Z J, Wang Y Q, and Chu C W, *Superconductivity at 93 K in a new mixed-phase Y-Ba-Cu-O compound system at ambient pressure.* Physical Review Letters, **58** (9). pp. 908-910, 1987.

[18] Dimos D, Chaudhari P, and Mannhart J, *Superconducting transport properties of grain boundaries in $YBa_2Cu_3O_7$ bicrystals.* Physical Review B, **41** (7). pp. 4038-4049, 1990.

[19] Dimos D, Chaudhari P, Mannhart J, and LeGoues F K, *Orientation dependence of grain-boundary critical currents in $YBa_2Cu_3O_{7-\delta}$ bicrystals.* Physical Review Letters, **61** (2). pp. 219-222, 1988.

[20] Yamane H, Masumoto H, Hirai T, Iwasaki H, Watanabe K, Kobayashi N, Muto Y, and Kurosawa H, *Y-Ba-Cu-O superconducting films prepared on $SrTiO_3$ substrates by chemical vapor deposition.* Applied Physics Letters, **53** (16). pp. 1548-1550, 1988.

[21] Obradors X, Puig T, Pomar A, Sandiumenge F, Piñol S, Mestres N, Castaño O, Coll M, Cavallaro A, Palau A, Gázquez J, González J C, Gutiérrez J, Romà N, Ricart S, Moretó J M, Rossell M D, and Tendeloo G v, *Chemical solution deposition: a path towards low cost coated conductors.* Superconductor Science and Technology, **17** (8). pp. 1055-1064, 2004.

[22] Araki T and Hirabayashi I, *Review of a chemical approach to $YBa_2Cu_3O_{7-x}$ coated superconductors-metalorganic deposition using trifluoroacetates.* Superconductor Science and Technology, **16** (11). pp. R71-R94, 2003.

[23] Goyal A, Norton D P, Budai J D, Paranthaman M, Specht E D, Kroeger D M, Christen D K, He Q, Saffian B, List F A, Lee D F, Martin P M, Klabunde C E, Hartfield E, and Sikka V K, *High critical current density superconducting tapes by epitaxial deposition*

of $YBa_2Cu_3O_x$ thick films on biaxially textured metals. Applied Physics Letters, **69** (12). pp. 1795-1797, 1996.

[24] Goyal A, Paranthaman M P, and Schoop U, *The RABiTS approach: Using rolling-assisted biaxially textured substrates for high-performance YBCO superconductors.* MRS Bulletin, **29** (8). pp. 552-561, 2004.

[25] Gupta A, Jagannathan R, Cooper E I, Giess E A, Landman J I, and Hussey B W, *Superconducting oxide films with high transition temperature prepared from metal trifluoroacetate precursors.* Applied Physics Letters, **52** (24). pp. 2077-2079, 1988.

[26] McIntyre P C, Cima M J, and Ng M F, *Metalorganic deposition of high-J_c $Ba_2YCu_3O_{7-x}$ thin films from trifluoroacetate precursors onto (100) $SrTiO_3$.* Journal of Applied Physics, **68** (8). pp. 4183-4187, 1990.

[27] Obradors X, Puig T, Ricart S, Coll M, Gazquez J, Palau A, and Granados X, *Growth, nanostructure and vortex pinning in superconducting $YBa_2Cu_3O_7$ thin films based on trifluoroacetate solutions.* Superconductor Science and Technology, **25** (12), art. 123001, 2012.

[28] Farjas J, Camps J, Roura P, Ricart S, Puig T, and Obradors X, *The thermal decomposition of barium trifluoroacetate.* Thermochimica Acta, **544**. pp. 77-83, 2012.

[29] Obradors X, Puig T, Pomar A, Sandiumenge F, Mestres N, Coll M, Cavallaro A, Rom N, Gázquez J, González J C, Castão O, Gutierrez J, Palau A, Zalamova K, Morlens S, Hassini A, Gibert M, Ricart S, Moretó J M, Pĩol S, Isfort D, and Bock J, *Progress towards all-chemical superconducting $YBa_2Cu_3O_{7-\delta}$ coated conductors.* Superconductor Science and Technology, **19** (3). pp. S13-S26, 2006.

[30] Araki T, *Purified coating solution and growth scheme of the $YBa_2Cu_3O_{7-x}$ superconductors in metal organic deposition using trifluoroacetates.* Bulletin of the Chemical Society of Japan, **77** (6). pp. 1051-1061, 2004.

[31] Feenstra R, Lindemer T B, Budai J D, and Galloway M D, *Effect of oxygen pressure on the synthesis of $YBa_2Cu_3O_{7-x}$ thin films by post-deposition annealing.* Journal of Applied Physics, **69** (9). pp. 6569-6585, 1991.

[32] Gàzquez J, Sandiumenge F, Coll M, Pomar A, Mestres N, Puig T, Obradors X, Kihn Y, Casanove M J, and Ballesteros C, *Precursor evolution and nucleation mechanism of $YBa_2Cu_3O_x$ films by TFA metal–organic decomposition.* Chemistry of Materials, **18** (26). pp. 6211-6219, 2006.

[33] Llordés A, Zalamova K, Ricart S, Palau A, Pomar A, Puig T, Hardy A, Van Bael M K, and Obradors X, *Evolution of metal-trifluoroacetate precursors in the thermal decomposition toward high-performance $YBa_2Cu_3O_7$ superconducting films.* Chemistry of Materials, **22** (5). pp. 1686-1694, 2010.

[34] Niwa T, Araki T, Muroga T, Iijima Y, Yamada Y, Saitoh T, Hirabayashi I, and Shiohara Y, *Calcining conditions for $YBa_2Cu_3O_{7-x}$ films by metalorganic deposition using*

trifluoroacetates. IEEE Transactions on Applied Superconductivity, **13** (2). pp. 2747-2750, 2003.

[35] Zalamova K, Pomar A, Palau A, Puig T, and Obradors X, *Intermediate phase evolution in YBCO thin films grown by the TFA process.* Superconductor Science and Technology, **23** (1), art. 014012, 2010.

[36] Chen H, Zalamova K, Pomar A, Granados X, Puig T, and Obradors X, *Growth rate control and solid–gas modeling of TFA-$YBa_2Cu_3O_7$ thin film processing.* Superconductor Science and Technology, **23** (3), art. 034005, 2010.

[37] Fuji H, Teranishi R, Kito Y, Matsuda J, Nakaoka K, Izumi T, Shiohara Y, Yamada Y, Yajima A, and Saitoh T, *Progress on TFA-MOD coated conductor development.* Physica C: Superconductivity and its Applications, **426–431, Part 2**. pp. 938-944, 2005.

[38] Wesolowski D E, Yoshizumi M, and Cima M J, *Trajectory-property relationships in MOD-derived YBCO films.* Physica C: Superconductivity and its Applications, **450** (1–2). pp. 76-82, 2006.

[39] Dew-Hughes D, *The critical current of superconductors: An historical review.* Low Temperature Physics, **27** (9-10). pp. 713-722, 2001.

[40] Bellis R H and Iwasa Y, *Quench propagation in high T_c superconductors.* Cryogenics, **34** (2). pp. 129-144, 1994.

[41] Jorgensen J D, Veal B W, Paulikas A P, Nowicki L J, Crabtree G W, Claus H, and Kwok W K, *Structural properties of oxygen-deficient $YBa_2Cu_3O_7$.* Physical Review B, **41** (4). pp. 1863-1877, 1990.

[42] Tallon J L, *Oxygen in high-T_c cuprate superconductors*, in *Frontiers in Superconducting Materials* A V Narlikar, Editor, Springer. ISBN 3-540-24513, 2005.

[43] Stadelmann P A, *EMS - a software package for electron diffraction analysis and HREM image simulation in materials science.* Ultramicroscopy, **21** (2). pp. 131-145, 1987.

[44] Zandbergen H W, Gronsky R, Wang K, and Thomas G, *Structure of $(CuO)_2$ double layers in superconducting $YBa_2Cu_3O_7$.* Nature, **331** (6157). pp. 596-599, 1988.

[45] MacManus-Driscoll J L, Alonso J A, Wang P C, Geballe T H, and Bravman J C, *Studies of structural disorder in $ReBa_2Cu_3O_{7-x}$ thin films (Re=rare earth) as a function of rare-earth ionic radius and film deposition conditions.* Physica C: Superconductivity and its Applications, **232** (3-4). pp. 288-308, 1994.

[46] Schoop U, Rupich M W, Thieme C, Verebelyi D T, Zhang W, Li X, Kodenkandath T, Nguyen N, Siegal E, Civale L, Holesinger T, Maiorov B, Goyal A, and Paranthaman M, *Second generation HTS wire based on RABiTS substrates and MOD YBCO.* IEEE Transactions on Applied Superconductivity, **15** (2 PART III). pp. 2611-2616, 2005.

[47] Shannon R D, *Revised effective ionic radii and systematic studies of interatomic distances in halides and chalcogenides.* Acta Crystallographica Section A, **32** (5). pp. 751-767, 1976.

[48] Guillaume M, Allenspach P, Mesot J, Roessli B, Staub U, Fischer P, and Furrer A, *A systematic neutron diffraction study of $RBa_2Cu_3O_7$ (R=yttrium and rare earths) high-T_c superconductors.* Zeitschrift für Physik B Condensed Matter, **90** (1). pp. 13-17, 1993.

[49] Morris D E, Nickel J H, Wei J Y T, Asmar N G, Scott J S, Scheven U M, Hultgren C T, Markelz A G, Post J E, Heaney P J, Veblen D R, and Hazen R M, *Eight new high-temperature superconductors with the 1:2:4 structure.* Physical Review B, **39** (10). pp. 7347-7350, 1989.

[50] Camerlingo C and Jung G, *Evaluation of the out-of-plane coherence length in (103)/(013) $YBa_2Cu_3O_{7-\delta}$ films from electrical transport measurements.* Superconductor Science and Technology, **18** (8). pp. 1106-1111, 2005.

[51] Gutiérrez J, Llordés A, Gázquez J, Gibert M, Romà N, Ricart S, Pomar A, Sandiumenge F, Mestres N, Puig T, and Obradors X, *Strong isotropic flux pinning in solution-derived $YBa_2Cu_3O_{7-x}$ nanocomposite superconductor films.* Nature Materials, **6** (5). pp. 367-373, 2007.

[52] Guzman R, Gazquez J, Rouco V, Palau A, Magen C, Varela M, Arbiol J, Obradors X, and Puig T, *Strain-driven broken twin boundary coherence in $YBa_2Cu_3O_{7-\delta}$ nanocomposite thin films.* Applied Physics Letters, **102** (8), art. 081906, 2013.

[53] Maiorov B, Baily S A, Zhou H, Ugurlu O, Kennison J A, Dowden P C, Holesinger T G, Foltyn S R, and Civale L, *Synergetic combination of different types of defect to optimize pinning landscape using $BaZrO_3$-doped $YBa_2Cu_3O_7$.* Nature Materials, **8** (5). pp. 398-404, 2009.

[54] Puig T, Gutiérrez J, Pomar A, Llordés A, Gázquez J, Ricart S, Sandiumenge F, and Obradors X, *Vortex pinning in chemical solution nanostructured YBCO films.* Superconductor Science and Technology, **21** (3), art. 034008, 2008.

[55] Mele P, Matsumoto K, Horide T, Ichinose A, Mukaida M, Yoshida Y, Horii S, and Kita R, *Ultra-high flux pinning properties of $BaMO_3$-doped $YBa_2Cu_3O_{7-x}$ thin films (M = Zr, Sn).* Superconductor Science and Technology, **21** (3), art. 032002, 2008.

[56] Engel S, Thersleff T, Hühne R, Schultz L, and Holzapfel B, *Enhanced flux pinning in $YBa_2Cu_3O_7$ layers by the formation of nanosized $BaHfO_3$ precipitates using the chemical deposition method.* Applied Physics Letters, **90** (10), art. 102505, 2007.

[57] Gapud A A, Kumar D, Viswanathan S K, Cantoni C, Varela M, Abiade J, Pennycook S J, and Christen D K, *Enhancement of flux pinning in $YBa_2Cu_3O_{7-\delta}$ thin films embedded with epitaxially grown Y_2O_3 nanostructures using a multi-layering process.* Superconductor Science and Technology, **18** (11). pp. 1502-1505, 2005.

[58] Viswanathan S K, Gapud A A, Varela M, Abiade J T, Christen D K, Pennycook S J, and Kumar D, *Enhancement of critical current density of $YBa_2Cu_3O_{7-\delta}$ thin films by self-*

assembly of Y_2O_3 nanoparticulates. Thin Solid Films, **515** (16 SPEC. ISS.). pp. 6452-6455, 2007.

[59] Goyal A, Li J, Martin P M, Gapud A, Specht E D, Paranthaman M, Li X, Zhang W, Kodenkandath T, and Rupich M W, *Enhanced Flux-Pinning in Dy-Doped, MOD YBCO Films on RABiTS.* IEEE Transactions on Applied Superconductivity, **17** (2). pp. 3340-3342, 2007.

[60] Specht E D, Goyal A, Li J, Martin P M, Li X, and Rupich M W, *Stacking faults in $YBa_2Cu_3O_{7-x}$: Measurement using X-ray diffraction and effects on critical current.* Applied Physics Letters, **89** (16), 2006.

[61] Xia J, Long N, Strickland N M, Hoefakker P, Talantsev E F, Li C, Zhang W, Kodenkandath T, Huang Y, and Rupich M W, *TEM observation of the microstructure of metal-organic deposited $YBa_2Cu_3O_{7-\delta}$ with Dy additions.* Superconductor Science and Technology, **20** (8). pp. 880-885, 2007.

[62] Zhang W, Huang Y, Li X, Kodenkandath T, Rupich M W, Schoop U, Verebelyi D T, Thieme C L H, Siegal E, Holesinger T G, Maiorov B, Civale L, Miller D J, Maroni V A, Li J, Martin P M, Specht E D, Goyal A, and Paranthaman M P, *Control of flux pinning in MOD YBCO coated conductor.* IEEE Transactions on Applied Superconductivity, **17** (2). pp. 3347-3350, 2007.

[63] Ortalan V, Herrera M, Rupich M W, and Browning N D, *Three dimensional analyses of flux pinning centers in Dy-doped $YBa_2Cu_3O_{7-x}$ coated superconductors by STEM tomography.* Physica C: Superconductivity and its Applications, **469** (23-24). pp. 2052-2059, 2009.

[64] Llordés A, Palau A, Gázquez J, Coll M, Vlad R, Pomar A, Arbiol J, Guzmán R, Ye S, Rouco V, Sandiumenge F, Ricart S, Puig T, Varela M, Chateigner D, Vanacken J, Gutiérrez J, Moshchalkov V, Deutscher G, Magen C, and Obradors X, *Nanoscale strain-induced pair suppression as a vortex-pinning mechanism in high-temperature superconductors.* Nature Materials, **11** (4). pp. 329-336, 2012.

[65] Macmanus-Driscoll J L, Foltyn S R, Jia Q X, Wang H, Serquis A, Civale L, Maiorov B, Hawley M E, Maley M P, and Peterson D E, *Strongly enhanced current densities in superconducting coated conductors of $YBa_2Cu_3O_{7-x}$ + $BaZrO_3$.* Nature Materials, **3** (7). pp. 439-443, 2004.

[66] Wang H, Serquis A, Maiorov B, Civale L, Jia Q X, Arendt P N, Foltyn S R, MacManus-Driscoll J L, and Zhang X, *Microstructure and transport properties of Y-rich $YBa_2Cu_3O_{7-\delta}$ thin films.* Journal of Applied Physics, **100** (5), art. 053904, 2006.

[67] McIntyre P C and Cima M J, *Microstructural inhomogeneities in chemically derived $Ba_2YCu_3O_{7-x}$ thin films: Implications for flux pinning.* Journal of Materials Research, **9** (11). pp. 2778-2788, 1994.

[68] Mele P, Guzman R, Gazquez J, Puig T, Obradors X, Saini S, Yoshida Y, Mukaida M, Ichinose A, Matsumoto K, and Idries Adam M, *High pinning performance of $YBa_2Cu_3O_{7-x}$ films added with Y_2O_3 nanoparticulate defects.* Superconductor Science and Technology, **28** (2), art. 024002, 2015.

[69] Rouco V, Palau A, Guzman R, Gazquez J, Coll M, Obradors X, and Puig T, *Role of twin boundaries on vortex pinning of CSD YBCO nanocomposites.* Superconductor Science and Technology, **27** (12), art. 125009, 2014.

[70] Van Tendeloo G, Zandbergen H W, Van Landuyt J, and Amelinckx S, *Electron microscopy of high T_c superconductors.* Materials Characterization, **27** (2). pp. 59-89, 1991.

[71] Zhu Y, Tsai C F, and Wang H, *Atomic interface sequence, misfit strain relaxation and intrinsic flux-pinning defects in different $YBa_2Cu_3O_{7-\delta}$ heterogeneous systems.* Superconductor Science and Technology, **26** (2), art. 025009, 2013.

[72] Gazquez J, Coll M, Roma N, Sandiumenge F, Puig T, and Obradors X, *Structural defects in trifluoroacetate derived $YBa_2Cu_3O_7$ thin films.* Superconductor Science and Technology, **25** (6), art. 065009, 2012.

[73] Vinnikov L Y, Gurevich L A, Grigoryeva I V, Koshelev A E, and Osip'yan Y A, *Observation of the flux line lattice in high T_c superconductors.* Journal of the Less Common Metals, **164**. pp. 1271-1284, 1990.

[74] Wang H, Foltyn S R, Arendt P N, Jia Q X, and Zhang X, *Identification of the misfit dislocations at $YBa_2Cu_3O_{7-\delta}/SrTiO_3$ interface using moiré fringe contrast.* Physica C: Superconductivity and its Applications, **444** (1-2). pp. 1-4, 2006.

[75] Araki T, Yuasa T, Kurosaki H, Yamada Y, Hirabayashi I, Kato T, Hirayama T, Iijima Y, and Saito T, *High-J_c $YBa_2Cu_3O_{7-x}$ films on metal tapes by the metalorganic deposition method using trifluoroacetates.* Superconductor Science and Technology, **15** (1). pp. L1-L3, 2002.

[76] Williams D B and Carter C B, *Transmission electron microscopy: A textbook for materials science (Second edition),* Edition, Springer, ISBN 978-0-387-76500-6, p. 760, 2009.

[77] Nishiyama T, Kaneko K, Yamada K, Teranishi R, Kato T, Hirayama T, Izumi T, and Shiohara Y, *Microstructural characterization of TFA-MOD processed $Y_{1-x}Gd_xBa_2Cu_3O_{7-y}$ with $BaZrO_3$.* Micron, **52-53**. pp. 1-7, 2013.

[78] Yamada K, Mitsuhara M, Hata S, Miyanaga Y, Teranishi R, Mori N, Mukaida M, and Kaneko K, *Three-dimensional observation of microstructures in Y123 films fabricated by TFA-MOD method.* Physica C: Superconductivity and its Applications, **469** (15-20). pp. 1446-1449, 2009.

[79] Loudon J C, Yazdi S, Kasama T, Zhigadlo N D, and Karpinski J, *Measurement of the penetration depth and coherence length of MgB_2 in all directions using transmission electron microscopy.* Physical Review B - Condensed Matter and Materials Physics, **91** (5), art. 054505, 2015.

[80] Liang W Y and Loram J W, *Magneto-calorimetric studies of reversible magnetisation.* Proceedings of the third European Conference on Vortex Matter, **404** (1-4). pp. 230-240, 2004.

[81] Sonier J E, Sabok-Sayr S A, Callaghan F D, Kaiser C V, Pacradouni V, Brewer J H, Stubbs S L, Hardy W N, Bonn D A, Liang R, and Atkinson W A, *Hole-doping dependence of the magnetic penetration depth and vortex core size in $YBa_2Cu_3O_y$: Evidence for stripe correlations near 1/8 hole doping.* Physical Review B - Condensed Matter and Materials Physics, **76** (13), 2007.

[82] Prozorov R and Giannetta R W, *Magnetic penetration depth in unconventional superconductors.* Superconductor Science and Technology, **19** (8). pp. R41-R67, 2006.

[83] Bonn D A, Liang R, Riseman T M, Baar D J, Morgan D C, Zhang K, Dosanjh P, Duty T L, MacFarlane A, Morris G D, Brewer J H, Hardy W N, Kallin C, and Berlinsky A J, *Microwave determination of the quasiparticle scattering time in $YBa_2Cu_3O_{6.95}$.* Physical Review B, **47** (17). pp. 11314-11328, 1993.

[84] Basov D N, Puchkov A V, Hughes R A, Strach T, Preston J, Timusk T, Bonn D A, Liang R, and Hardy W N, *Disorder and superconducting-state conductivity of single crystals of $YBa_2Cu_3O_{6.9}$.* Physical Review B, **49** (17). pp. 12165-12169, 1994.

[85] Tallon J L, Bernhard C, Binninger U, Hofer A, Williams G V M, Ansaldo E J, Budnick J I, and Niedermayer C, *In-plane anisotropy of the penetration depth due to superconductivity on the Cu-O chains in $YBa_2Cu_3O_{7-\delta}$, $Y_2Ba_4Cu_7O_{15-\delta}$, and $YBa_2Cu_4O_8$.* Physical Review Letters, **74** (6). pp. 1008-1011, 1995.

[86] Lauter-Pasyuk V, Lauter H J, Aksenov V L, Kornilov E I, Petrenko A V, and Leiderer P, *Determination of the magnetic field penetration depth in $YBa_2Cu_3O_7$ superconducting films by polarized neutron reflectometry.* Physica B: Condensed Matter, **248** (1–4). pp. 166-170, 1998.

[87] Prozorov R, Giannetta R W, Carrington A, Fournier P, Greene R L, Guptasarma P, Hinks D G, and Banks A R, *Measurements of the absolute value of the penetration depth in high-T_c superconductors using a low-T_c superconductive coating.* Applied Physics Letters, **77** (25). pp. 4202-4204, 2000.

[88] Djordjevic S, Farber E, Deutscher G, Bontemps N, Durand O, and Contour J P, *Low temperature dependence of the penetration depth in YBCO thin films revisited by mm wave transmission and surface impedance measurements.* The European Physical Journal B, **25** (4). pp. 407-416, 2002.

[89] Carrington A, Giannetta R W, Kim J T, and Giapintzakis J, *Absence of nonlinear Meissner effect in $YBa_2Cu_3O_{6.95}$.* Physical Review B, **59** (22). pp. R14173-R14176, 1999.

[90] Zheng D N, Campbell A M, Johnson J D, Cooper J R, Blunt F J, Porch A, and Freeman P A, *Magnetic susceptibilities, critical fields, and critical currents of Co- and Zn-doped $YBa_2Cu_3O_7$.* Physical Review B, **49** (2). pp. 1417-1426, 1994.

[91] Kokubo N, Tamochi H, Shinozaki B, Nishizaki T, and Kobayashi N, *Orientation of a moving vortex lattice in an amorphous $Mo_{1-x}Ge_x$ superconducting film.* Journal of Physics: Conference Series, **400** (2), 2012.

[92] Kasama T, Dunin-Borkowski R E, and Beleggia M, *Electron holography of magnetic materials*, in *Holography - Different fields of application*, F Monroy, Editor, InTech. ISBN 978-953-307-635-5, pp. 53-80, 2011.

[93] Tonomura A, *Fundamentals and applications of electron holography*, in *Holography, research and technologies*, J Rosen, Editor, InTech. ISBN 978-953-307-227-2, 2011.

[94] Beleggia M, Fanesi S, Patti R, and Pozzi G, *Recent results in the interpretation of interference and Lorentz images of vortices in superconductors.* Materials Characterization, **42** (4). pp. 209-220, 1999.

[95] Beleggia M, Pozzi G, Masuko J, Osakabe N, Harada K, Yoshida T, Kamimura O, Kasai H, Matsuda T, and Tonomura A, *Interpretation of Lorentz microscopy observations of vortices in high-temperature superconductors with columnar defects.* Physical Review B, **66** (17), art. 174518, 2002.

[96] Harada K, Matsuda T, Bonevich J, Igarashi M, Kondo S, Pozzi G, Kawabe U, and Tonomura A, *Real-time observation of vortex lattices in a superconductor by electron microscopy.* Nature, **360** (6399). pp. 51-53, 1992.

[97] Petford-Long A K and Chapman J N, *Lorentz Microscopy*, in *Magnetic Microscopy of Nanostructures*, H Hopster and H P Oepen, Editors, Springer Berlin Heidelberg: Berlin, Heidelberg. ISBN 978-3-540-26641-9, pp. 67-86, 2005.

[98] Lichte H, *Performance limits of electron holography.* Ultramicroscopy, **108** (3). pp. 256-262, 2008.

[99] Yazdi S, *Towards electron holography of working transistors*, Imperial College London, *PhD Thesis,* 2012.

[100] McCartney M R, Dunin-Borkowski R E, and Smith D J, *Electron holography of magnetic nanostructures*, in *Magnetic microscopy of nanostructures*, H Hopster and H Oepen, Editors, Springer Berlin Heidelberg. ISBN 978-3-540-40186-5, pp. 87-109, 2005.

[101] Dolan G J, Holtzberg F, Feild C, and Dinger T R, *Anisotropic vortex structure in $Y_1Ba_2Cu_3O_7$.* Physical Review Letters, **62** (18). pp. 2184-2187, 1989.

[102] Essmann U and Träuble H, *The direct observation of individual flux lines in type II superconductors.* Physics Letters A, **24** (10). pp. 526-527, 1967.

[103] Hess H F, Robinson R B, Dynes R C, Valles J M, and Waszczak J V, *Scanning-tunneling-microscope observation of the Abrikosov flux lattice and the density of states near and inside a fluxoid.* Physical Review Letters, **62** (2). pp. 214-216, 1989.

[104] Mannhart J, Bosch J, Gross R, and Huebener R P, *Two-dimensional imaging of trapped magnetic flux quanta in Josephson tunnel junctions.* Physical Review B, **35** (10). pp. 5267-5269, 1987.

[105] Matsuda T, Hasegawa S, Igarashi M, Kobayashi T, Naito M, Kajiyama H, Endo J, Osakabe N, Tonomura A, and Aoki R, *Magnetic field observation of a single flux*

quantum by electron-holographic interferometry. Physical Review Letters, **62** (21). pp. 2519-2522, 1989, http://dx.doi.org/10.1103/PhysRevLett.62.2519.

[106] Bonevich J E, Harada K, Matsuda T, Kasai H, Yoshida T, Pozzi G, and Tonomura A, *Electron holography observation of vortex lattices in a superconductor.* Physical Review Letters, **70** (19). pp. 2952-2955, 1993, http://dx.doi.org/10.1103/PhysRevLett.70.2952.

[107] Kawasaki T, Matsui I, Yoshida T, Katsuta T, Hayashi S, Onai T, Furutsu T, Myochin K, Numata M, Mogaki H, Gorai M, Akashi T, Kamimura O, Matsuda T, Osakabe N, Tonomura A, and Kitazawa K, *Development of a 1 MV field-emission transmission electron microscope.* Journal of Electron Microscopy, **49** (6). pp. 711-718, 2000.

[108] Kawasaki T, Yoshida T, Matsuda T, Osakabe N, Tonomura A, Matsui I, and Kitazawa K, *Fine crystal lattice fringes observed using a transmission electron microscope with 1 MeV coherent electron waves.* Applied Physics Letters, **76** (10). pp. 1342-1344, 2000.

[109] Tonomura A, Kasai H, Kamimura O, Matsuda T, Harada K, Nakayama Y, Shimoyama J, Kishio K, Hanaguri T, Kitazawa K, Sasase M, and Okayasu S, *Observation of individual vortices trapped along columnar defects in high-temperature superconductors.* Nature, **412** (6847). pp. 620-622, 2001.

[110] Tonomura A, *Direct observation of vortices in high-T_c superconductors.* Physica C: Superconductivity and its Applications, **388-389**. pp. 624-626, 2003.

[111] Tonomura A, Kasai H, Kamimura O, Matsuda T, Harada K, Yoshida T, Akashi T, Shimoyama J, Kishio K, Hanaguri T, Kitazawa K, Masui T, Tajima S, Koshizuka N, Gammel P L, Bishop D, Sasase M, and Okayasu S, *Observation of structures of chain vortices inside anisotropic high-T_c superconductors.* Physical Review Letters, **88** (23), art. 237001, 2002, http://dx.doi.org/10.1103/PhysRevLett.88.237001.

[112] Cottet M J G, Cantoni M, Mansart B, Alexander D T L, Hébert C, Zhigadlo N D, Karpinski J, and Carbone F, *Quantitative imaging of flux vortices in the type-II superconductor MgB_2 using cryo-Lorentz transmission electron microscopy.* Physical Review B - Condensed Matter and Materials Physics, **88** (1), art. 014505, 2013.

[113] Loudon J C, Bowell C J, and Midgley P A, *Quantitative imaging of flux vortices in superconductors.* Journal of Physics: Conference Series, **391** (1), art. 012117, 2012.

[114] Loudon J C, Bowell C J, Zhigadlo N D, Karpinski J, and Midgley P A, *Imaging flux vortices in MgB_2 using transmission electron microscopy.* Physica C: Superconductivity and its Applications, **474**. pp. 18-20, 2012.

[115] Nagamatsu J, Nakagawa N, Muranaka T, Zenitani Y, and Akimitsu J, *Superconductivity at 39 K in magnesium diboride.* Nature, **410** (6824). pp. 63-64, 2001.

[116] Loudon J C, Bowell C J, Zhigadlo N D, Karpinski J, and Midgley P A, *Magnetic structure of individual flux vortices in superconducting MgB_2 derived using transmission electron microscopy.* Physical Review B, **87** (14), art. 144515, 2013.

[117] Joshi A G, Pillai C G S, Raj P, and Malik S K, *Magnetization studies on superconducting MgB_2 - Lower and upper critical fields and critical current density.* Solid State Communications, **118** (9). pp. 445-448, 2001.

[118] Li S L, Wen H H, Zhao Z W, Ni Y M, Ren Z A, Che G C, Yang H P, Liu Z Y, and Zhao Z X, *Linear temperature dependence of lower critical field in MgB_2.* Physical Review B, **64** (9), art. 094522, 2001.

[119] Takano Y, Takeya H, Fujii H, Kumakura H, Hatano T, Togano K, Kito H, and Ihara H, *Superconducting properties of MgB_2 bulk materials prepared by high-pressure sintering.* Applied Physics Letters, **78** (19). pp. 2914-2916, 2001.

[120] Benkraouda M and Clem J R, *Magnetic hysteresis from the geometrical barrier in type-II superconducting strips.* Physical Review B - Condensed Matter and Materials Physics, **53** (9). pp. 5716-5726, 1996.

[121] Paranthaman M P, *Chemical solution deposition based oxide buffers and YBCO coated conductors,* Edition, Applications of High-T_c Superconductivity, ISBN 978-953-307-308-8, 2011.

[122] Guinebretière R, *Diffraction des rayons X sur échantillons polycristallins. Instrumentation et étude de la microstructure. (2^e édition revue et augmentée),* Lavoisier Edition, Hermes Science Publishing, ISBN 2-7462-1238-2, p. 361, 2006.

[123] Hendricks S and Teller E, *X-Ray interference in partially ordered layer lattices.* The Journal of Chemical Physics, **10** (3). pp. 147-167, 1942.

[124] Talantsev E F, Strickland N M, Wimbush S C, Storey J G, Tallon J L, and Long N J, *Hole doping dependence of critical current density in $YBa_2Cu_3O_{7-\delta}$ conductors.* Applied Physics Letters, **104** (24), art. 242601, 2014.

[125] Talantsev E F, Wimbush S C, Strickland N M, Xia J A, D'Souza P, Storey J G, Tallon J L, Ingham B, Knibbe R, and Long N J, *Oxygen deficiency, stacking faults and calcium substitution in MOD YBCO coated conductors.* IEEE Transactions on Applied Superconductivity, **23** (3), 2013.

[126] Schneider C A, Rasband W S, and Eliceiri K W, *NIH Image to ImageJ: 25 years of image analysis.* Nature Methods, **9** (7). pp. 671-675, 2012.

[127] Raffa V, Vittorio O, Pensabene V, Menciassi A, and Dario P, *FIB-nanostructured surfaces and investigation of bio/nonbio interactions at the nanoscale.* IEEE Transactions on Nanobioscience, **7** (1). pp. 1-10, 2008.

[128] He Q, Christen D K, Budai J D, Specht E D, Lee D F, Goyal A, Norton D P, Paranthaman M, List F A, and Kroeger D M, *Deposition of biaxially-oriented metal and oxide buffer-layer films on textured Ni tapes: New substrates for high-current, high-temperature superconductors.* Physica C: Superconductivity and its Applications, **275** (1-2). pp. 155-161, 1997.

[129] Paranthaman M, Goyal A, List F A, Specht E D, Lee D F, Martin P M, He Q, Christen D K, Norton D P, Budai J D, and Kroeger D M, *Growth of biaxially textured buffer*

layers on rolled-Ni substrates by electron beam evaporation. Physica C: Superconductivity and its Applications, **275** (3-4). pp. 266-272, 1997.

[130] Onoda M, Shamoto S-i, Sato M, and Hosoya S, *Crystal Structures of $YBa_2Cu_3O_x$ and $LnBa_2Cu_3O_x$ (Ln = Ho and Dy).* Japanese Journal of Applied Physics, **26** (5A). pp. L876-L878, 1987.

[131] Strickland N M, Hoffmann C, and Wimbush S C, *A 1 kA-class cryogen-free critical current characterization system for superconducting coated conductors.* Review of Scientific Instruments, **85** (11), art. 113907, 2014.

[132] Strickland N M, Talantsev E F, Xia J A, Long N J, Rupich M W, Li X, and Zhang W, *Flux pinning by barium stannate nanoparticles in MOD YBCO coated conductors.* IEEE Transactions on Applied Superconductivity, **19** (3). pp. 3140-3143, 2009.

[133] Benzi P, Bottizzo E, and Rizzi N, *Oxygen determination from cell dimensions in YBCO superconductors.* Journal of Crystal Growth, **269** (2-4). pp. 625-629, 2004.

[134] Feldmann D M, Holesinger T G, Cantoni C, Feenstra R, Nelson N A, Larbalestier D C, Verebelyi D T, Li X, and Rupich M, *Grain orientations and grain boundary networks of $YBa_2Cu_3O_{7-\delta}$ films deposited by metalorganic and pulsed laser deposition on biaxially textured Ni-W substrates.* Journal of Materials Research, **21** (4). pp. 923-934, 2006.

[135] Poole Jr C P, Farach H A, Creswick R J, and Prozorov R, *2 - Phenomenon of Superconductivity*, in *Superconductivity (Second Edition)*, C P Poole, H A Farach, and R J C Prozorov, Editors, Academic Press: Amsterdam. ISBN 978-0-12-088761-3, pp. 23-59, 2007.

[136] Breit V, Schweiss P, Hauff R, Wühl H, Claus H, Rietschel H, Erb A, and Müller-Vogt G, *Evidence for chain superconductivity in near-stoichiometric $YBa_2Cu_3O_x$ single crystals.* Physical Review B, **52** (22). pp. R15727-R15730, 1995.

[137] Liang R, Bonn D A, and Hardy W N, *Evaluation of CuO_2 plane hole doping in $YBa_2Cu_3O_{6+x}$ single crystals.* Physical Review B, **73** (18), art. 180505, 2006.

[138] Feldmann D M, Larbalestier D C, Verebelyi D T, Zhang W, Li Q, Riley G N, Feenstra R, Goyal A, Lee D F, Paranthaman M, Kroeger D M, and Christen D K, *Inter- and intragrain transport measurements in $YBa_2Cu_3O_{7-x}$ deformation textured coated conductors.* Applied Physics Letters, **79** (24). pp. 3998-4000, 2001.

[139] Yelland E A, Singleton J, Mielke C H, Harrison N, Balakirev F F, Dabrowski B, and Cooper J R, *Quantum oscillations in the underdoped cuprate $YBa_2Cu_4O_8$.* Physical Review Letters, **100** (4), art. 047003, 2008.

[140] Naamneh M, Campuzano J C, and Kanigel A, *Doping dependence of the critical current in$Bi_2Sr_2CaCu_2O_{8+\delta}$.* Physical Review B, **90** (22), art. 224501, 2014.

[141] Rupich M W, Verebelyi D T, Zhang W, Kodenkandath T, and Li X, *Metalorganic deposition of YBCO films for second-generation high-temperature superconductor wires.* MRS Bulletin, **29** (8). pp. 572-578+539-541, 2004.

[142] Foltyn S R, Jia Q X, Arendt P N, Kinder L, Fan Y, and Smith J F, *Relationship between film thickness and the critical current of $YBa_2Cu_3O_{7-\delta}$ coated conductors.* Applied Physics Letters, **75** (23). pp. 3692-3694, 1999.

[143] Castano O, Cavallaro A, Palau A, Gonzalez J C, Rosell M, Puig T, Pinol S, Mestres N, Sandiumenge F, Pomar A, and Obradors X, *Influence of porosity on the critical currents of trifluoroacetate-MOD $YBa_2Cu_3O_7$ films.* IEEE Transactions on Applied Superconductivity, **13** (2). pp. 2504-2507, 2003.

[144] Midgley P A, *An introduction to off-axis electron holography.* Micron, **32** (2). pp. 167-184, 2001.

[145] Grissonnanche G, Cyr-Choinière O, Laliberté F, René de Cotret S, Juneau-Fecteau A, Dufour-Beauséjour S, Delage M È, LeBoeuf D, Chang J, Ramshaw B J, Bonn D A, Hardy W N, Liang R, Adachi S, Hussey N E, Vignolle B, Proust C, Sutherland M, Krämer S, Park J H, Graf D, Doiron-Leyraud N, and Taillefer L, *Direct measurement of the upper critical field in cuprate superconductors.* Nature Communications, **5**, 2014.